Acoustic foams with pore size distributions and controlled interconnections: Structures-properties-fabrication relationships

Cong Truc Nguyen

UNIVERSITÉ PARIS-EST SUP

École doctorale Sciences, Ingénierie et Environnement

THÈSE

pour obtenir le grade de

DOCTEUR DE L'UNIVERSITÉ GUSTAVE EIFFEL

Spécialité: Mécanique

Présentée par

Cong Truc NGUYEN

Mousses acoustiques à distributions de tailles de pores et interconnexions contrôlées: Relations structures, propriétés, fabrication

---

Soutenue le 26 mai 2021 devant le jury composé de

F. SGARD	IRSST (CA)	Président
O. DOUTRES	Ecole de Technologie Supérieure (CA)	Rapporteur
M.-A. GALLAND	Ecole Centrale de Lyon (FR)	Rapportrice
C. PERROT	Université Gustave Eiffel (FR)	Directeur
J. GUILLEMINOT	Duke University (USA)	Co-directeur
F. DETREZ	Université Gustave Eiffel (FR)	Co-encadrant
V. LANGLOIS	Université Gustave Eiffel (FR)	Co-encadrant
E. SADOULET-REBOUL	Université de Franche-Comté (FR)	Examinatrice
A. DUVAL	CERA - Trèves group (FR)	Invité
B. VANDAMME	EMPA (CH)	Invité

Laboratoire Modélisation et Simulation Multi Echelle MSME UMR 8208 CNRS

Remerciements

A l'issue de ce travail de recherche, je suis convaincu que la thèse doctorale n'est pas un travail solitaire. En effet, je n'aurais jamais pu la réaliser sans le soutien d'un grand nombre de personnes dans cette phase délicate de "l'apprenti chercheur".

Cette thèse a été réalisée au sein du laboratoire Modélisation et Simulation Multi Echelle (UMR 8208 CNRS) de l'université Gustave Eiffel en partenariat industriel avec le Centre d'Etude et de Recherche pour l'Automobile (CERA) du groupe Trèves, sous convention CIFRE No. 2017/ 1098 à partir de Décembre 2017. A ce titre, je tiens à remercier l'ANRT et CERA pour leur soutien financier. Je remercie aussi l'équipe Acoustique du CERA son accueil chaleureux, l'expertise et les conseils de ses membres. Mes remerciements vont également à tous membres du laboratoire MSME pour y avoir fait régner une ambiance amicale au travail.

Je souhaiterais adresser mes sincères remerciements à mes directeurs et à mes encadrants, messieurs **Camille PERROT**, **Johann GUILLEMINOT**, **Vincent LANGLOIS** et **Fabrice DETREZ**, pour la confiance et le soutien qu'ils m'ont accordés. Je les remercie pour leur supervision, leur aide et leur culture scientifique qu'ils m'ont fait partager à travers de ces trois années de thèse.

J'exprime toute ma reconnaissance aux membres du jury: **Olivier DOUTRES**, **Marie-Annick GALLAND**, **Emeline SADOULET-REBOUL**, **Franck SGARD**, **Arnaud DUVAL**, **Bart VAN DAMME**, pour le temps qu'ils ont passé à évaluer mon travail. Leurs remarques constructives, leurs questions intéressantes ont suscité une réflexion ouvrant d'autres perspectives à mon travail.

Un grand merci à **Lei LEI**, **Anders LINDBERG** (CERA), **Fabien CHEVILLOTTE**, **Fabien MARCHETTI** (Matelys) pour leur implication en caractérisation, **Rémy PIRES BRAZUNA** (ICMPE) côté imagerie MEB, **Michel BORNERT** et **Patrick AIMEDIEU** (ENPC) sur le plan de l'imagerie par tomographie, **Marie-Hélène ALEXANDRE** en ce qui concerne l'édition scientifique en langue anglaise.

Je tiens à exprimer mon amitié à tous mes amis qui ont contribué de près ou de loin au bon déroulement de mon travail et avec qui j'ai passé de bons moments.

Enfin, du fond de mon cœur, je remercie ma famille, mon père, ma mère, ma petite sœur et ma petite amie pour leur soutien indéfectible, leur patience et leur encouragement au cours de l'élaboration de cette thèse.

Il est difficile à lister les noms de toutes les personnes auxquelles j'aimerais exprimer ma reconnaissance. Merci à toutes les personnes côtoyées que je n'ai, hélas, pas pu les mentionner.

Résumé

Les mousses sont utilisées fréquemment notamment en raison de leurs propriétés d'absorption et d'isolation sonore. Les exigences accrues en matière de réductions d'émissions de CO_2 combinées à des exigences de performances acoustiques, thermiques, et de tenue au feu impliquent un effort significatif tourné vers l'allègement des traitements acoustiques—à performances égales ou supérieures. L'introduction de particules fines lors du processus de moussage, réalisée afin d'améliorer la tenue au feu, perturbe les sites de nucléation, ce qui conduit à la production de microstructures désordonnées où coexistent localement des cellules de tailles très contrastées. Ce travail de thèse traite de la construction d'outils numériques pour la modélisation du comportement acoustique de mousses polydisperses à partir d'une démarche multi-échelle et multi-physique. L'objectif principal est de pouvoir développer des relations entre la géométrie locale et le macro-comportement acoustique, afin de pouvoir guider la fabrication de mousses dans le but d'optimiser leurs performances acoustiques. Nous nous intéressons plus particulièrement au cas de mousses qui, présentant une forte hétérogénéité locale de tailles de pores, ne peuvent être décrites par une cellule périodique idéalisée (modèle déterministe). Des techniques d'imagerie avancées (microtomographie axiale à rayons-X et microscopie électronique à balayage) sont utilisées, dans un premier temps, pour identifier les caractéristiques morphologiques des microstructures étudiées. Les caractéristiques géométriques obtenues sont ensuite modélisées afin de reconstruire des partitions spatiales proches de celles mesurées. La perméabilité visqueuse, paramètre clé au regard de la détermination des propriétés acoustiques, est estimée par une simulation de type "pore-network". Nous quantifions, au travers de telles simulations, que la perméabilité d'une mousse est fortement influencée, non seulement par la présence des membranes, mais aussi par la variation de la taille des pores. L'effet de l'épaisseur de membrane sur les paramètres visqueux (longueur caractéristique visqueuse et tortuosité) décrivant le comportement asymptotique haute fréquence est, de plus, finement étudié. Les résultats obtenus montrent, en particulier, qu'il est possible de modéliser l'effet de l'épaisseur de membranes minces par des membranes virtuelles sans épaisseur pour le calcul de la longueur caractéristique visqueuse. Enfin, les propriétés acoustiques d'un échantillon réel de mousse ayant une distribution étendue de tailles de pores sont modélisées. Une bonne concordance avec les données expérimentales obtenues à partir d'un tube d'impédance confirme la validité de la méthode proposée.

Mots-clés: Mousses acoustiques, microstructures, distribution étendue de tailles de pores, mousse polydisperse, méthode multi-échelle.

Abstract

Foam materials are frequently used in engineering applications, due to their absorption and sound insulation properties. At the same time, the evolution of CO_2 emission goals, together with new standards for acoustic, thermal, and fire resistance performance, calls for further developments that seek to reduce the impact of acoustic treatments—while maintaining, or even improving, global performance. Fine particles are usually introduced during the foaming process to improve fire resistance. By disrupting the nucleation sites, this procedure leads to disordered microstructures where cells of very different sizes coexist locally. This thesis work deals with the construction and experimental validation of a computational multi-scale-informed framework for modeling the acoustic behavior of polydisperse foams. The main objective is to model the relationships between the local foam geometry and the acoustic behavior exhibited at macroscale, with a view towards devising foam manufacturing conditions under acoustic performance targets. Here, we restrict our attention to the case of foams which present strong local heterogeneities in terms of pore sizes and therefore cannot be described by a deterministic unit cell. Advanced imaging techniques (namely, axial X-ray microtomography and scanning electron microscopy) are first deployed to identify relevant morphological characteristics on the studied microstructures. The geometrical properties thus obtained are then used in order to reconstruct spatial partitions consistent with the observations. The viscous permeability, which is a key parameter for the determination of acoustic properties, is estimated through "Pore-Network" simulations. The numerical predictions show that the permeability of a foam is strongly influenced, not only by the presence of membranes, but also by the variation of pore sizes. The effect of membrane thickness on viscous parameters (i.e., the viscous characteristic length and the tortuosity) describing the asymptotic behavior at high frequencies is also thoroughly studied. For the calculation of the viscous characteristic length, the results show that the effect of thin-membrane thickness can equivalently be modeled by virtual membranes without thickness. Finally, the acoustic properties of a real foam sample presenting a wide pore size distribution are modeled. Good agreement with experimental data obtained from an impedance tube is observed, which supports the relevance of the proposed approach.

Keywords: Acoustic foams, microstructures, wide pore size distribution, polydisperse foam, multiscale method.

Contents

List of Figures

List of Tables

List of Symbols

Most acronyms and variables used in this manuscript are defined upon first use. The most frequently used symbols are presented below for the sake of convenience.

α_∞	High frequency tortuosity
Δ	Laplace operator
η	Dynamic viscosity of air
η_e	Loss factor
Λ	Viscous characteristic length
Λ'	Thermal characteristic length
$\langle\cdot\rangle$	Average operator
$\mathcal{B}_{ef}$	Effective bulk modulus
∇	Gradient operator
ν_e	Poisson's coefficient
ω	Angular frequency
Ω_f, Ω	Fluid phase, total porous volume
$\partial\Omega$	Solid-fluid interface
ϕ	Porosity
ρ_0	Density of air
ρ_1	Mass density of porous material
ρ_{ef}	Effective dynamic density
σ	Static air flow resistivity
τ_o	Membranes aperture rate
$\mathbf{E}$	Electric field
c_d	Variation coefficient of pore size
d	Pore size
E	Young's modulus

e_m	Membrane thickness
h_e	Finite element size
i	Imaginary unit
K	Global permeability
k'_0	Static thermal permeability
k_0	Static viscous permeability
N_p	Total number of pores
N_v	Number of neighbor pores
P	Pressure
Q	Volume fluid flow rate
r_o	Aperture size
s	Sphericity of pore size
t_o	Aperture ratio of open membrane
x_o, x_c	Proportion of open and closed membranes
CERA	Centre d'Étude et de Recherche pour l'Automobile du groupe Trèves
FEM	Finite element method
JCAL	Johnson-Champoux-Allard-Lafarge (model)
PU	Polyurethane (foam)
PUC	Periodic unit cell
RVE	Representative volume element

Chapter I

General introduction

Contents

I.1 Industrial context

Porous materials such as cellular foams (which consist of a frame structure with an interstitial fluid, e.g., air, filling the voids) are well known for their good sound absorption and thermal insulation qualities. As a consequence, they are widely used in industrial applications such as construction and transport (automobile, rail, aeronautics, etc.). In the automotive industry for example, porous materials appear frequently in the cabin, the trunk, the engine bay and the body in order to reduce noise pollution and improve users' comfort (see Fig. I.1).

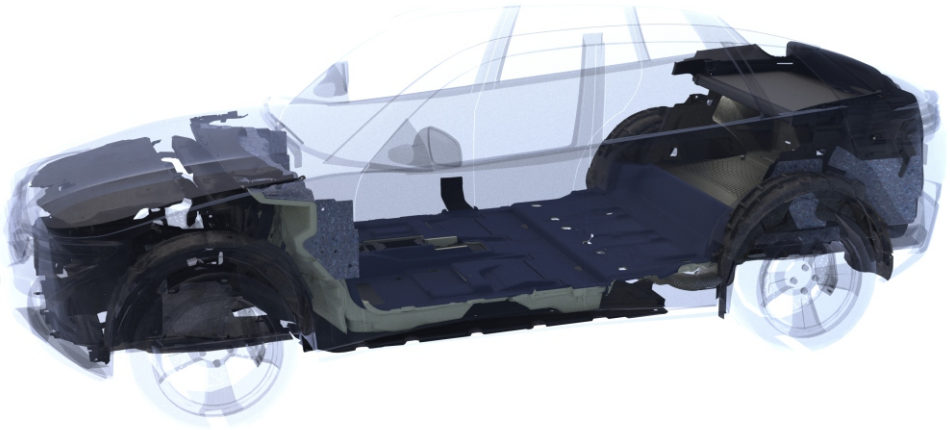

Figure I.1: Use of porous materials in automotive industry. Photo source: TREVES website.

New environmental (e.g., CO_2 emission) standards for sustainable development, combined with constraints on acoustic, thermal, and flame retardant performance, have led manufacturers to increasingly lighten materials. This evolution comes in parallel with the ongoing replacement of fibrous media by foams due to public health concerns, since fibers with diameters of less than $6\mu m$ are likely to be carcinogenic (if not bio-soluble). These public health objectives and environmental standards thus play a crucial role in the deployment of innovative solutions, while lightening and improving the insulation character are antagonistic elements in acoustics.

In this context where solutions by trial-and-error prove to be costly and ineffective, multi-scale and multi-physics approaches leading to a detailed understanding of the involved physics become inevitable. Thus, significant efforts have been made over the last decades to define multi-physics models of acoustic foams, through i) the identification of idealized microstructures, ii-1) the resolution of boundary value problems governing physical phenomena of interest at the local scale, ii-2) solution field averages leading to the calculation of macroscopic parameters, iii) experimental validation comparing the calculated macroscopic parameters with properties measured on physical samples. Such a multi-scale approach has led to substantial progress allowing both a better understanding of the physical origin of the visco-thermal and visco-elastic structural dissipation effects, and also helped engineers design the new generation of insulation systems. Indeed, multi-scale approaches enable the chemist and the acoustic engineer to work in a synergistic manner, using microstructural information, and to converge towards an optimal acoustical material design.

In order to improve the flame retardant of acoustic foams, fine particles are often introduced during the foaming process. An unanticipated effect of the introduction of these fine particles is to disrupt the nucleation sites, leading to disordered microstructures where locally bubbles of

very contrasting sizes coexist. These new candidates have proved to be interesting from an acoustic point of view, paving the way for the development of new generation insulating systems. However, the coexistence of very contrasting bubble sizes leads to local heterogeneity, and the representative volume element (RVE) can no longer be obtained by means of a single cell capable to reproduce most of physics.

Additionally, in the highly competitive context of the automotive industry, partnership research is an asset that makes it possible to identify scientific and technological issues or obstacles to be overcome while constituting interdisciplinary and complementary work teams (chemistry and processes on the one hand, computational mechanics on the other). Therefore, this thesis work is dedicated to the modeling of acoustic foams with random distribution of pore size and membranes in the industrial-academic partnership between TREVES Products Services & Innovation (CERA - Centre d'Étude et de Recherche pour l'Automobile du groupe Trèves) and the Laboratory of Multi-scale Modeling and Simulation (UMR 8208 CNRS), Paris-Est Marne-La-Vallée University, France, under CIFRE agreement No. 2017/1098.

I.2 Scientific context

Acoustic properties of porous materials such as foams are driven by the structural and visco-thermal dissipation of the sound propagation in these materials. In order to describe these behaviors, several approaches are proposed.

The empirical approach is not only the simplest but also the most used. It is based on observations and experimental characterizations to identify the empirical laws that can be used for the analysis of acoustic properties. The most famous empirical model was proposed by Delany and Bazley in 1970 [27] in which the characteristic impedance and the complex wave number depend on ratio between frequency and air flow resistivity by power laws. Miki [69] proposed an improvement of the behavior at low frequencies, thus making it possible to ensure a positive and physical value of the characteristic impedance. An additional correction was proposed by Beranek and Ver [100]. Allard and Champoux [3] derived another empirical model in which the dynamic density and the dynamic compressibility are defined with an additional validation at low frequencies. In general, empirical models are easy to use. However, they are generally limited to a specific class of materials and are not adapted to the optimization of microstructures.

Semi-phenomenological approaches make it possible to determine the acoustic behavior of materials from analytical solutions associated with simple geometries by introducing one or more form factors to describe the dependence on more complex local geometries. An analytical solution for a network of parallel circular cylindrical pores was developed by Zwikker and Kosten [111] by treating viscous and thermal effects separately. Biot (1956a,1956b) [8, 7] developed a theory on the propagation of elastic waves in a saturated porous medium having a deformable and elastic skeleton. A semi-phenomenological model describing viscous-inertial mechanisms with a rigid frame assumption was derived in the work of Johnson, Koplik and Dashen [49], it was then refined by Pride [79]. Effect of thermal dissipation was carried out by Champoux and Allard [20] as well as Lafarge et al. [56]. Biot's theory can be used to take account of structural dissipation [47]. The inputs of these approaches are macroscopic parameters having a physical significance linked to the low or high frequency asymptotic behaviors of the porous medium involved and giving a physical understanding of the porous material behavior. Originally, input macroscopic parameters are measured by experiments.

Based on the homogenization theory of periodic structures, the equations governing properties of fluid in porous media, i.e., a coupled visco-thermal problem, can be solved by two uncoupled viscous-thermal problems performed on a RVE [110]. This approach links material microstructure features to their acoustical behavior. However, since the calculations must be carried out for the full

interested range of frequencies, main limits of this approach lie on computational cost, particularly in the case of three-dimensional geometry, the most useful for the study of optimal microstructures. Nevertheless, the low and high frequency asymptotic solution of this approach could give the input parameters of semi-phenomenological models (instead of direct measurements). Such an approach is called a hybrid multi-scale method and it is most promising for our work.

Using one of the above approaches, several studies were carried out on the effect of microstructural features on the acoustic performance of foams. It was shown in a series of works by Hoang et al. [76, 94, 95, 45, 46] that the average pore size governs acoustic properties of open-cell foams with narrow pore size distributions. For a wider distribution of pore size, the acoustical behavior is controlled by critical pore sizes that are deduced from porosity and viscous permeability. When the foams have fully or partially closed membranes, additional identification of membrane content is necessary. In these works as well as in Park et al. [75], the effect of membranes was studied via aperture ratio (or closure rates) through a hybrid multi-scale method. By using semi-phenomenological approaches with an empirical link of foam microstructure and non-acoustic properties as in the works of Doutres et al. [29, 30] or by numerical homogenization as in Park's work, effect of closed membranes was also investigated. Recently, by using different approaches both without and with elasto-acoustic coupling, Trinh et al. [97] and Gao et al. [37] showed the importance of taking into account both the fraction of closed membranes and aperture ratio of open ones for the acoustic modeling of the foams having both fully closed and partially open membranes. All of the above works study the effect of membranes content on foam absorption. However, it could be seen that these works were carried out mainly on the basis of one or a network of single pore size, i.e., Kelvin or Weaire-Phelan cell structure. One may observe that the effects of polydispersity on the mechanical behavior of cellular foams can be found in the literature [81, 64, 66, 39, 67] but their effects on acoustic properties of foam with complex membrane contents, i.e., both fully closed and partially closed membranes, are still to be elucidated.

I.3 Study objectives

The next key step is to control a random distribution of pore size and their interconnections (membrane sizes). The main objective of this thesis is to model the acoustic behavior of heterogeneous or chaotic foams (random wide distribution of pore size and interconnections in a restricted RVE) through the multi-scale approaches in order to assess the dependence of transport and acoustic properties of material as a function of microstructure parameters. The obstacles to be removed remain in particular on the morphological modeling of complex RVE, the computational cost of which increases rapidly with the number of cellular pores treated. To find a compromise aimed at capturing physics without resorting to prohibitive computing times, the following steps are necessary:

1. Acquisition: The first step consists in acquiring the characteristics of the local geometry of the acoustic foams studied. An approach combining axial X-ray microtomography (μCT) and analysis of images obtained by scanning electron microscopy (SEM) will be used. These two techniques are complementary [37]. The μCT is well suited to the determination of pore size distributions. However, its resolution is insufficient to estimate the sizes of interconnections and their distribution. By performing sections on two orthogonal planes of the foam samples studied, SEM images allow us to study the sizes of interconnections between pores by local estimation of the membrane apertures ratio and their distributions. Even if this last technique is destructive and can damage the membranes on the section plane, the SEM images have the particularity of being acute over a large depth of field, which allows to finely characterize the first undamaged layer.

2. Reconstruction: Using data from the microstructure of foam samples, simplified three-dimensional cell models will be reconstructed based on the Laguerre tessellation. To reduce the computational cost, ligaments system and thickness of membranes will not be modeled.

3. Calculation of acoustic properties through a hybrid multi-scale method with the search of low computational cost techniques of the calculations in order to allow computational estimates on reconstructed microstructures containing a large number of heterogeneous cells.

4. Validation using laboratory experiments: acoustic properties of virtual samples characterized from the above mentioned steps will be compared with experimental data independently measured from a three-microphones impedance tube in order to validate the proposed multi-scale approach.

This thesis is organized as follows. Chapter II is devoted to a literature review on numerical approaches for the acoustic properties calculation of porous media. The microstructure of a real polydisperse foam is characterized and reconstructed in chapter III. As a key parameter of transport and acoustic properties, the permeability of polydisperse foams is studied in chapter IV. In chapter V, effect of membrane thickness on the viscous characteristic length is investigated. In order to deal with computational cost, a calculation technique of this characteristic length from an equivalent geometry of zero-thickness membranes is proposed. Chapter VI presents the simulation of the acoustic behavior of a real polydisperse foam sample. Finally, a general conclusion of the thesis and some perspectives for future work are presented in chapter VII.

Chapter II

Numerical approach for sound absorption of porous media

Contents

II.1 Introduction

In this thesis, we are particularity interested in the sound absorption coefficient which represents the proportion of the sound energy that an acoustical layer is able to absorb. In the case of a porous layer of finite thickness in contact with air on its front face and fixed to a rigid impervious wall on its rear face, the sound absorption coefficient is related to the surface reflection coefficient $R(\omega)$ which is the ratio of the pressures created by the outgoing ($p'(M)$) and the ingoing waves ($p(M)$) at the surface of the porous layer (Fig. II.1). The sound absorption coefficient at normal-incident (SAC_{NI}) corresponds to the ingoing waves perpendicular to the surface of the porous layer. The SAC_{NI} varies from 0 for total reflection to 1 for total absorption.

$$SAC_{NI}(\omega) = 1 - \left|R(\omega)\right|^2 = 1 - \left|\frac{p'(M)}{p(M)}\right|^2. \tag{II.1}$$

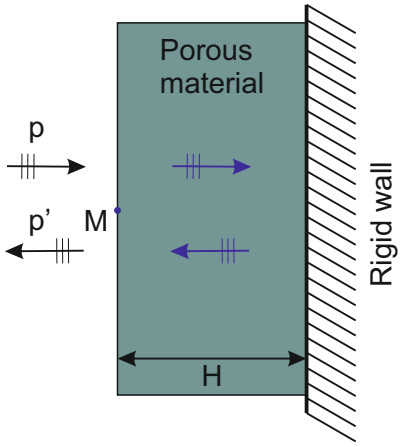

Figure II.1: The normal-incident waves in a porous layer of thickness H backed by a rigid impervious wall.

In this chapter, a bibliographical revision about numerical approaches to the acoustic properties of porous materials is provided. Firstly, the sound propagation in rigid-frame porous media will briefly be described by the governing equations. By applying the two-scale asymptotic homogenization method which is based on periodicity, the sound propagation will be written as a Helmholtz equation and the air saturating in porous media will be considered as an equivalent fluid having complex properties, i.e., mass density and bulk modulus. Then the semi-phenomenological models will be presented, their input parameters will be calculated from an approximation of three asymptotic behaviors of equivalent fluids: static viscous, inertial and static thermal. Therefore, the SAC_{NI} of rigid-frame porous layer can be computed. Finally, the Biot's theory will be introduced with assuming complex properties of equivalent fluid to predict the sound absorption coefficient at normal-incident of a porous material having an elastic frame.

II.2 Direct simulation

In a harmonic regime, the flow of a compressible fluid (air) saturating pore domain Ω_f of a porous medium Ω with rigid skeleton is described by the linearized Navier-Stokes-Fourier equations [47, 110] including the mass conservation II.2a, momentum conservation II.2b, energy conservation

II.2c and the equation of state II.2d:

$$\rho_0 \nabla \cdot \mathbf{u} + i\omega\rho = 0 \quad \text{in} \quad \Omega_f, \tag{II.2a}$$

$$\eta\left(\nabla^2\mathbf{u} + \frac{1}{3}\nabla\left(\nabla\cdot\mathbf{u}\right)\right) - \nabla p = i\omega\rho_0\mathbf{u} \quad \text{in} \quad \Omega_f, \tag{II.2b}$$

$$\kappa\nabla^2 T = i\omega\rho_0 C_p T - i\omega p \quad \text{in} \quad \Omega_f, \tag{II.2c}$$

$$\frac{p}{P_0} = \frac{\rho}{\rho_0} + \frac{T}{T_0} \quad \text{in} \quad \Omega_f, \tag{II.2d}$$

in which **u**, p, ρ and T are the fluid velocity, pressure, density and temperature, respectively. The dynamic viscosity, thermal conductivity, and heat capacity at constant pressure of the air are denoted by η, κ and C_p, respectively. ρ_0 is the air density at the ambient pressure P_0 and temperature T_0. The angular frequency $\omega = 2\pi f$ with f is the frequency, i is the imaginary unit. The above equations describe a coupled visco-thermal problem in the porous medium. The direct simulation solves this problem on the fluid domain Ω_f of whole porous layer (thickness H) attached to a rigid wall and an adjacent thin layer of air (thickness H_a) is added to put a plane wave source with adiabatic pressure condition (see Fig. II.2). The no-slip and isothermal conditions are imposed on both the fluid-solid interface $\partial\Omega$ and the rigid wall:

$$\mathbf{u} = 0, \tag{II.3a}$$

$$T = 0. \tag{II.3b}$$

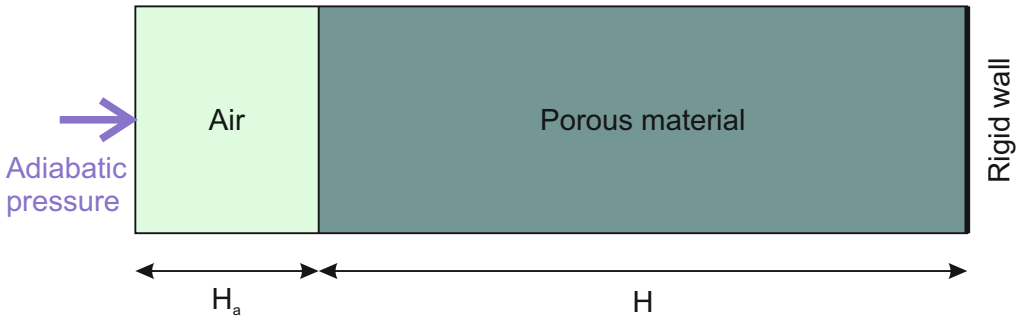

Figure II.2: Direct simulation schema.

The simulation gives the complex-valued solutions of **u**, p, ρ and T for each frequency ω. There, the SAC_{NI} of the porous material $\text{SAC}_{\text{NI}}\left(\omega\right)$ is computed by:

$$\text{SAC}_{\text{NI}}\left(\omega\right) = 1 - \left|\frac{Z_s\left(\omega\right) - Z_0}{Z_s\left(\omega\right) + Z_0}\right|^2, \tag{II.4}$$

where the surface acoustic impedance $Z_s\left(\omega\right) = p\left(\omega\right)/\mathbf{u}\left(\omega\right)$ can be computed at any single point on the external boundary of the adjacent air layer and Z_0 is the impedance of air [110].

This method is computationally very demanding since it requires solutions for each frequency and the simulation has to be performed on a large fluid domain even when the symmetrical properties of porous material are taken into account by applying the periodic or symmetric conditions on the lateral fluid boundaries. Therefore, it is suitable for the models of 2D or 3D simple geometries.

II.3 Homogenization of rigid-frame porous media

In this section, we will recall how the sound propagation in a porous media is described by using the two-scale asymptotic homogenization method [48] based on periodicity. Let us consider a periodic porous material in which the size of local heterogeneities determines a microscopic characteristic length l and the sound wavelength λ determines a macroscopic characteristic length $L = \lambda/2\pi$. The condition of scale separation is assumed, i.e., $\epsilon = l/L \ll 1$.

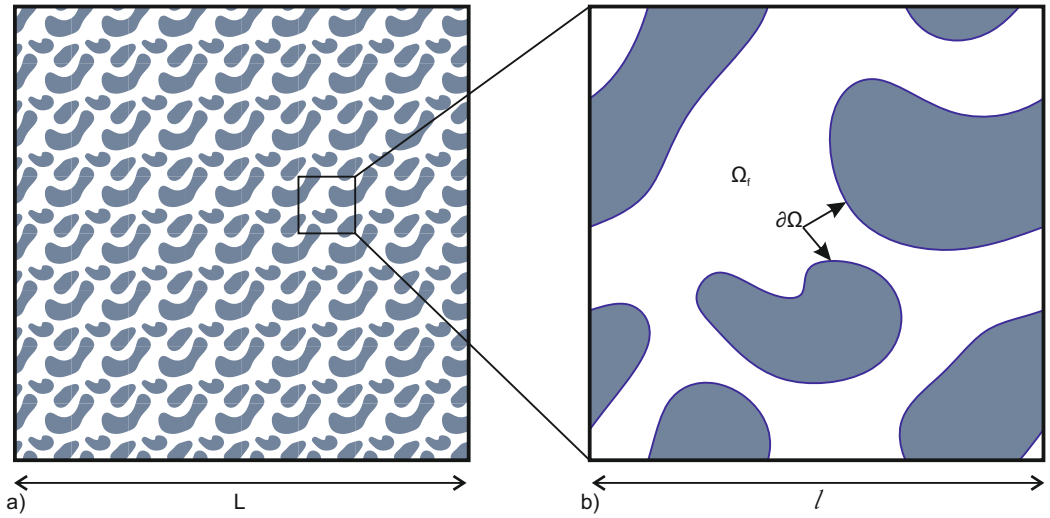

Figure II.3: Macroscopic scale description a) and microscopic scale description b) of a periodic porous media.

The two-scale asymptotic procedure is as follows:

1. Introduce two independent space variables: x for macroscopic scale description and $y = \epsilon^{-1}x$ for microscopic scale description. The physical variables are function of x and y, given as:

$$\mathbf{u} = \mathbf{u}^{(0)}(x,y) + \epsilon\mathbf{u}^{(1)}(x,y) + \mathcal{O}\left(\epsilon^2\right), \tag{II.5a}$$

$$p = p^{(0)}(x,y) + \epsilon p^{(1)}(x,y) + \mathcal{O}\left(\epsilon^2\right), \tag{II.5b}$$

$$T = T^{(0)}(x,y) + \epsilon T^{(1)}(x,y) + \mathcal{O}\left(\epsilon^2\right), \tag{II.5c}$$

2. The gradient operator can be modified as: $\nabla = \nabla_x + \epsilon^{-1}\nabla_y$, the viscosity and conductivity coefficients are rescaled by ϵ^2 [10]:

$$\eta = \epsilon^2\eta^{(2)}, \tag{II.6a}$$

$$\kappa = \epsilon^2\kappa^{(2)}. \tag{II.6b}$$

3. Substitution of asymptotic series of physical variables in Eqs. II.5a-II.5c, gradient operator, and scaled parameters in Eqs. II.6a-II.6b into governing equations II.2a-II.2d and into boundary condition equations II.5a - II.5c. Then, the terms of same order of ϵ are identified.

At ϵ^{-1}:

$$\nabla_y p^{(0)} = \mathbf{0} \quad \text{in} \quad \Omega_f, \tag{II.7}$$
$$\nabla_y \cdot \mathbf{u}^{(0)} = 0 \quad \text{in} \quad \Omega_f, \tag{II.8}$$
$$\mathbf{u}^{(0)} = 0 \quad \text{on} \quad \partial\Omega, \tag{II.9}$$
$$T^{(0)} = 0 \quad \text{on} \quad \partial\Omega. \tag{II.10}$$

At ϵ^0:

$$\eta^{(2)} \nabla_y^2 \mathbf{u}^{(0)} - \nabla_y p^{(1)} = i\omega \mathbf{u}^{(0)} + \nabla_x p^{(0)} \quad \text{in} \quad \Omega_f, \tag{II.11}$$
$$\kappa^{(2)} \nabla_y^2 T^{(0)} = i\omega \rho_0 C_p T^{(0)} - i\omega p^{(0)} \quad \text{in} \quad \Omega_f, \tag{II.12}$$
$$\nabla_x \cdot \mathbf{u}^{(0)} + \nabla_y \cdot \mathrm{u}^{(1)} + i\omega \left(\frac{p^{(0)}}{P_0} - \frac{T^{(0)}}{T_0} \right) = 0 \quad \text{in} \quad \Omega_f. \tag{II.13}$$

Equation II.7 means that at leading order, the pressure is purely macroscopic, i.e., pressure $p^{(0)}$ depends only on x: $p^{(0)} = p^{(0)}(x)$.

The dynamic Stokes flow cell problem is identified from Eqs. II.8, II.9 and II.11. At a given frequency, linear relationships between the macroscopic pressure gradient and velocity $\mathbf{u}^{(0)}$ and between the macroscopic pressure gradient and local pressure $p^{(1)}$ are assumed [62, 5, 56]:

$$\mathbf{u}^{(0)}(x, y) = -\frac{\tilde{\underline{\underline{\mathbf{k}}}}(y, \omega)}{\eta^{(2)}} \cdot \nabla_x p^{(0)}(x), \tag{II.14}$$
$$p^{(1)}(x, y) = -\tilde{\boldsymbol{\chi}}(y, \omega) \cdot \nabla_x p^{(0)}(x) + \bar{p}^{(1)}(x), \tag{II.15}$$

where $\tilde{\underline{\underline{\mathbf{k}}}}(y, \omega)$, $\tilde{\boldsymbol{\chi}}(y, \omega)$ are a local tensor and a local vector, respectively, $\bar{p}^{(1)}(x)$ is a constant. $\tilde{\underline{\underline{\mathbf{k}}}}(y, \omega)$, $\tilde{\boldsymbol{\chi}}(y, \omega)$ are Ω-periodic fields, i.e. satisfy the condition of periodic continuity on the corresponding fluid boundaries lying on the opposite faces of the periodic cell Ω.

Now, we define an averaging operator:

$$\langle \cdot \rangle = \frac{1}{\Omega} \int_{\Omega_f} (\cdot)\, dV = \frac{\phi}{\Omega_f} \int_{\Omega_f} (\cdot)\, dV = \phi \langle \cdot \rangle_f. \tag{II.16}$$

Here, $\langle \cdot \rangle_f = \frac{1}{\Omega_f} (\cdot)\, dV$ is the fluid-phase average, $\phi = \Omega_f / \Omega$ denotes the porosity. By applying the operator II.16 to Eq. II.15, we have: $\langle \tilde{\boldsymbol{\chi}}(y, \omega) \rangle = 0$ due to $\bar{p}^{(1)}(x)$ is a constant field. Similarly, with Eq. II.14:

$$\langle \mathbf{u}^{(0)}(x, y) \rangle = -\frac{\langle \tilde{\underline{\underline{\mathbf{k}}}}(y, \omega) \rangle}{\eta^{(2)}} \cdot \nabla_x p^{(0)}(x). \tag{II.17}$$

This is dynamic Darcy's law [5] where the dynamic viscous permeability tensor $\underline{\underline{\mathbf{K}}}(\omega)$ is calculated by:

$$\underline{\underline{\mathbf{K}}}(\omega) = \langle \tilde{\underline{\underline{\mathbf{k}}}}(y, \omega) \rangle = \phi \langle \tilde{\underline{\underline{\mathbf{k}}}}(y, \omega) \rangle_f, \tag{II.18}$$

and the Darcy's velocity:

$$\mathbf{U}(x) = \langle \mathbf{u}^{(0)}(x, y) \rangle = \phi \langle \mathbf{u}^{(0)}(x, y) \rangle_f. \tag{II.19}$$

In the case where an isotropic wave propagation in isotropic media or a plane-wave propagation in the preferential direction defined by a unitary vector $\mathbf{e}$ is considered, the dynamic viscous permeability function is computed as:

$$\mathcal{K}(\omega) = \left(\underline{\underline{\mathbf{K}}}(\omega)\cdot\mathbf{e}\right)\cdot\mathbf{e} = \left(\langle\underline{\underline{\tilde{\mathbf{k}}}}(y,\omega)\cdot\mathbf{e}\rangle\right)\cdot\mathbf{e} = \langle\hat{\mathbf{k}}(y,\omega)\rangle\cdot\mathbf{e} = \phi\langle\hat{\mathbf{k}}(y,\omega)\rangle_f\cdot\mathbf{e}. \tag{II.20}$$

Here, $\hat{\mathbf{k}}(y,\omega) = \underline{\underline{\tilde{\mathbf{k}}}}(y,\omega)\cdot\mathbf{e}$ is the component vector of tensor $\underline{\underline{\tilde{\mathbf{k}}}}(y,\omega)$ projected onto direction $\mathbf{e}$. Similarly, we have the projection of the vector $\tilde{\boldsymbol{\chi}}(y,\omega)$ onto $\mathbf{e}$: $\hat{\chi}(y,\omega) = \tilde{\boldsymbol{\chi}}(y,\omega)\cdot\mathbf{e}$. Let us formally choose the locally-constant pressure gradient: $\nabla_x p^{(0)} = \|\nabla_x p^{(0)}\|\mathbf{e}$. Thus, the velocity $\mathbf{u}^{(0)}$ and local pressure $p^{(1)}$ can be rewritten from Eqs. II.14, II.15:

$$\mathbf{u}^{(0)} = -\frac{\hat{\mathbf{k}}}{\eta^{(2)}}\|\nabla_x p^{(0)}\|, \tag{II.21}$$

$$p^{(1)} = -\hat{\chi}\|\nabla_x p^{(0)}\| + \bar{p}^{(1)}(x). \tag{II.22}$$

Inserting Eqs. II.21, II.22 into the Eqs. II.11, II.8 and II.9, we obtain the scaled dynamic Stokes cell problem reformulated with no-slip boundaries:

$$\begin{aligned} \frac{i\omega\rho_0}{\eta^{(2)}}\hat{\mathbf{k}} - \nabla_y^2\hat{\mathbf{k}} + \nabla_y\hat{\chi} &= \mathbf{e} \quad \text{in} \quad \Omega_f, \\ \nabla_y\cdot\hat{\mathbf{k}} &= 0 \quad \text{in} \quad \Omega_f, \\ \hat{\mathbf{k}} &= \mathbf{0} \quad \text{on} \quad \partial\Omega \\ \hat{\mathbf{k}} \quad \text{and} \quad \hat{\chi} \quad &\text{are} \quad \Omega\text{-periodic}. \end{aligned} \tag{II.23}$$

In these equations, the scaled-velocity $\hat{\mathbf{k}}$ has unit of permeability (m^2) and the scaled-pressure $\hat{\chi}$ has unit of length (m).

The heat conduction cell problem describing heat diffusion effects is identified from Eqs. II.12, II.10. The solution of unknown temperature $T^{(0)}$ can be given as [62, 56]:

$$T^{(0)}(x,y) = \frac{\tilde{k}'(y,\omega)}{\kappa^{(2)}} i\omega p^{(0)}(x), \tag{II.24}$$

in which $\tilde{k}(y,\omega)$ is a local Ω-periodic scalar. The application averaging operator II.16 to Eq. II.24 yields:

$$\langle T^{(0)}(x,y)\rangle = \frac{\langle\tilde{k}'(y,\omega)\rangle}{\kappa^{(2)}} i\omega p^{(0)}(x). \tag{II.25}$$

This equation defines the dynamic thermal permeability function $\mathcal{K}'(\omega)$ [56]:

$$\mathcal{K}'(\omega) = \langle\tilde{k}'(y,\omega)\rangle = \phi\langle\tilde{k}'(y,\omega)\rangle_f. \tag{II.26}$$

Inserting Eq. II.24 into Eqs. II.12, II.10 leads to the scaled dynamic thermal diffusion problem with isothermal boundaries:

$$\begin{aligned} \frac{i\omega\rho_0}{\kappa^{(2)}}\tilde{k}' - \nabla_y^2\tilde{k}' &= 1 \quad \text{in} \quad \Omega_f, \\ \tilde{k}' &= 0 \quad \text{on} \quad \partial\Omega, \\ \tilde{k}' \quad &\text{is} \quad \Omega\text{-periodic}. \end{aligned} \tag{II.27}$$

The scaled-temperature $\tilde{k}'$ has unit of permeability (m^2).

By applying the averaging operator II.16 into three terms of Eq. II.13, we have:

$$\langle \nabla_x \cdot \mathbf{u}^{(0)} \rangle = \nabla_x \cdot \langle \mathbf{u}^{(0)} \rangle = \nabla_x \cdot \mathbf{U}(x), \tag{II.28a}$$

$$\langle \nabla_y \cdot \mathbf{u}^{(1)} \rangle = 0, \tag{II.28b}$$

$$\begin{aligned} \left\langle i\omega \left(\frac{p^{(0)}}{P_0} - \frac{T^{(0)}}{T_0} \right) \right\rangle &= i\omega \left(\frac{\left\langle p^{(0)} \right\rangle}{P_0} - \frac{\left\langle T^{(0)} \right\rangle}{T_0} \right) \cdots \\ &= i\omega \frac{\phi}{P_0} \left(1 - \frac{P_0}{T_0} \frac{i\omega}{\kappa^{(2)}} \left\langle \tilde{k}'(y,\omega) \right\rangle_f \right) p^{(0)}(x) \cdots \\ &= i\omega \frac{\phi}{P_0} \left(1 - \frac{P_0}{T_0} \frac{i\omega}{\phi \kappa^{(2)}} \mathcal{K}'(\omega) \right) p^{(0)}(x). \end{aligned} \tag{II.28c}$$

Thus, Eq. II.13 becomes:

$$\nabla_x \cdot \mathbf{U}(x) + i\omega \mathcal{B}_{ef}^{-1}(\omega) p^{(0)}(x) = 0. \tag{II.29}$$

This equation describes the harmonic sound propagation in a homogenized porous media having the effective bulk modulus $\mathcal{B}_{ef}$:

$$\mathcal{B}_{ef}(\omega) = \frac{P_0}{\phi} \left(1 - \frac{P_0}{T_0} \frac{i\omega}{\phi \kappa^{(2)}} \mathcal{K}'(\omega) \right)^{-1}. \tag{II.30}$$

In the case of an isotropic sound wave or a plane-wave propagating in the preferential direction, we have the dynamic viscous permeability tensor: $\underline{\underline{\mathbf{K}}}(\omega) = \mathcal{K}(\omega) \delta_{ij}$ where δ_{ij} is the Kronecker delta and the Darcy's velocity given by:

$$\mathbf{U}(x) = -\frac{\mathcal{K}(\omega)}{\eta^{(2)}} \nabla_x p^{(0)}(x). \tag{II.31}$$

The Eq. II.29 becomes the Helmholtz equation [47]:

$$\nabla_x^2 p^{(0)}(x) + \omega^2 \frac{\rho_{ef}(\omega)}{\mathcal{B}_{ef}(\omega)} p^{(0)}(x) = 0, \tag{II.32}$$

where the effective density ρ_{ef} is given by:

$$\rho_{ef}(\omega) = \frac{\eta^{(2)}}{i\omega \mathcal{K}(\omega)}, \tag{II.33}$$

thus, the effective wave number δ_{ef}, the effective sound speed c_{ef} and the effective characteristic impedance Z_{ef} are identified by the well-known relations: $\delta_{ef} = \omega \frac{\rho_{ef}}{\mathcal{K}}$, $c_{ef} = \sqrt{\frac{\mathcal{B}_{ef}}{\rho_{ef}}}$ and $Z_{ef} = \rho_{ef} c_{ef}$. The sound absorption of a porous layer of thickness H at normally-incident wave backed by impervious rigid wall can be estimated as:

$$\mathrm{SAC}_{\mathrm{NI}}(\omega) = 1 - \left| \frac{Z_s(\omega) - Z_0}{Z_s(\omega) + Z_0} \right|^2, \tag{II.34}$$

where $Z_s(\omega)$ is the surface impedance, given by:

$$Z_s(\omega) = -i \frac{Z_{ef}(\omega)}{\phi} \cot\left(\delta_{ef}(\omega) H \right). \tag{II.35}$$

In summary, it can be shown that the effective (complex-valued) properties (δ_{ef}, ρ_{ef}, $\mathcal{B}_{ef}$, ...) of a porous media are determined if we know a response function related to viscous effect, for example: the dynamic viscous permeability $\mathcal{K}(\omega)$, and a response function related to thermal effect, for example: the dynamic thermal permeability $\mathcal{K}'(\omega)$. Both of $\mathcal{K}(\omega)$ and $\mathcal{K}'(\omega)$ can be obtained numerically by averaging over the RVE of $\hat{\mathbf{k}}$ and $\tilde{k}'$, i.e., $\mathcal{K}(\omega) = \phi \left\langle \hat{\mathbf{k}}(\omega) \cdot \mathbf{e} \right\rangle_f$, $\mathcal{K}'(\omega) = \phi \left\langle \tilde{k}(\omega) \right\rangle_f$ which are the solutions of scaled dynamic Stokes problem II.23 and scaled thermal diffusion problem II.27, respectively. This approach requires the calculations for a set of frequency ω and is also known as the direct multiscale method.

II.4 Semi-phenomenological models and hybrid multiscale method

As demonstrated above, the acoustic behavior of rigid-frame porous media can be determined using a pair of complex response functions, one characterizes the viscous effect and the other concerns the thermal effect. The semi-phenomenological models propose the analytical expressions of the frequency dependent visco-inertial and thermal responses of porous media via effective dynamic density $\rho_{ef}(\omega)$ and effective dynamic bulk modulus $\mathcal{B}_{ef}(\omega)$.

In 1987, by introducing four transport parameters: the open porosity ϕ, the static air flow resistivity σ, the high-frequency tortuosity α_∞ and the viscous characteristic length Λ, Johnson Koplik and Dashen [49] presented a semi-phenomenological model to describe the effective dynamic density $\rho_{ef}(\omega)$ of a porous material with arbitrary pore shapes having a motionless skeleton:

$$\rho_{ef}(\omega) = \frac{\alpha_\infty \rho_0}{\phi}\left[1 + \frac{\phi\sigma}{i\omega\alpha_\infty\rho_0}\sqrt{1 + i\frac{4\alpha_\infty^2\eta\rho_0\omega}{\sigma^2\Lambda^2\phi^2}}\right], \tag{II.36}$$

where $\sigma = \eta/k_0$ is the flow resistivity of fluid and k_0 is the static viscous permeability. In 1991, based on the previous work of Johnson et al., and by adding the thermal characteristic length Λ', Champoux and Allard [20] proposed a formula of the effective dynamic bulk modulus $\mathcal{B}_{ef}(\omega)$ to describe the thermal effect for the same kind of porous material:

$$\mathcal{B}_{ef}(\omega) = \frac{\gamma P_0}{\phi}\left\{\gamma - (\gamma-1)\left[1 - i\frac{8\kappa}{\Lambda'^2 C_p\rho_0\omega}\sqrt{1 + i\frac{\Lambda'^2 C_p\rho_0\omega}{16\kappa}}\right]^{-1}\right\}^{-1}, \tag{II.37}$$

where γ is the specific heat ratio of the pore fluid. The formulas II.36 and II.37 describing visco-inertial and thermal dissipative effects with five transport parameters (ϕ, σ, α_∞, Λ, Λ') constitute the Johnson-Champoux-Allard (JCA) model.

The expression of $\mathcal{B}_{ef}(\omega)$ given by Champoux and Allard is then modified in 1993 by Lafarge et al. [56] who highlight a lack of information at low frequencies for thermal effects by introducing a new parameter, the static thermal permeability k_0', in order to describe the low frequency behavior of thermal effects:

$$\mathcal{B}_{ef}(\omega) = \frac{\gamma P_0}{\phi}\left\{\gamma - (\gamma-1)\left[1 - i\frac{\phi\kappa}{k_0' C_p\rho_0\omega\sqrt{1 + i\frac{4k_0'^2 C_p\rho_0\omega}{\kappa\Lambda'^2\phi^2}}}\right]^{-1}\right\}^{-1}. \tag{II.38}$$

The formulas II.36 and II.38 together with 6 transport parameters, i.e., 5 parameters as in the JCA model plus the static thermal permeability k_0' define the Johnson-Champoux-Allard-Lafarge (JCAL) model.

Finally, in the Johnson-Champoux-Allard-Pride-Lafarge (JCAPL) model, visco-inertial dissipative effects inside the porous media are refined by Pride et al. (1993) [79] by introducing a new macroscopic parameter, the static viscous tortuosity α_0, to improve the low-frequency asymptotic behavior of viscous dissipations. In 1997, D. Lafarge [56] also corrected the low frequency behavior of heat dissipation by adding the static thermal tortuosity α_0'. Thus, the final expressions for $\rho_{ef}(\omega)$ and $\mathcal{B}_{ef}(\omega)$ obtained as

$$\rho_{ef}(\omega) = \frac{\rho_0 \alpha_\infty}{\phi}\left[1 + \frac{\eta\phi}{i\omega\rho_0 k_0 \alpha_\infty}\left(1 - P + P\sqrt{1 + \frac{M}{2P^2}\frac{i\omega\rho_0 k_0 \alpha_\infty}{\eta\phi}}\right)\right], \tag{II.39}$$

$$\mathcal{B}_{ef}(\omega) = \frac{\gamma P_0}{\phi}\left\{\gamma - (\gamma-1)\left[1 + \frac{\phi\kappa}{i\omega\rho_0 C_p k_0'}\left(1 - P' + P'\sqrt{1 + \frac{M'}{2P'^2}\frac{i\omega\rho_0 C_p k_0'}{\phi\kappa}}\right)\right]^{-1}\right\}^{-1}, \tag{II.40}$$

where M, P, M', P' are non-dimensional factors, given by

$$M = \frac{8k_0\alpha_\infty}{\phi\Lambda^2}, \qquad P = \frac{M}{4\left(\alpha_0/\alpha_\infty - 1\right)}, \tag{II.41}$$

$$M' = \frac{8k_0'}{\phi\Lambda'^2}, \qquad P' = \frac{M'}{4\left(\alpha_0' - 1\right)}. \tag{II.42}$$

Notice that the JCAPL model requires a set of 8 transport parameters: 6 parameters as in the JCA model plus the static viscous tortuosity α_0 and the static thermal tortuosity α_0'. Also, the JCA and JCAL models can be obtained from the JCAPL one by setting, respectively, $M' = P = P' = 1$ and $P = P' = 1$.

Recently, the three semi-phenomenological models previously described are being widely used to characterize various poro-acoustical materials. Below, we will present how to numerically determine the input transports parameters.

The open porosity ϕ and the thermal characteristic length Λ' are pure geometrical parameter and their calculations are obvious:

$$\phi = \Omega_f/\Omega, \tag{II.43}$$

$$\Lambda' = 2\frac{\int_{\Omega_f} dV}{\int_{\partial\Omega} dS}. \tag{II.44}$$

The static viscous permeability which is defined by $k_0 = \lim_{\omega\to 0}\left(\mathcal{K}(\omega)\right)$ is obtained by resolving the scaled dynamic Stokes problem II.23 for $\omega \to 0$:

$$\begin{aligned} -\nabla_y^2\hat{\mathbf{k}}_0 + \nabla_y\hat{\chi}_0 &= \mathbf{e} \quad \text{in} \quad \Omega_f, \\ \nabla_y\cdot\hat{\mathbf{k}}_0 &= 0 \quad \text{in} \quad \Omega_f, \\ \hat{\mathbf{k}}_0 &= \mathbf{0} \quad \text{on} \quad \partial\Omega, \\ \hat{\mathbf{k}}_0 \quad \text{and} \quad \hat{\chi}_0 &\quad \text{are} \quad \Omega\text{-periodic}, \end{aligned} \tag{II.45}$$

and then, $k_0 = \phi\left\langle\hat{\mathbf{k}}_0\cdot\mathbf{e}\right\rangle_f$. The static viscous tortuosity α_0 is also calculated:

$$\alpha_0 = \frac{\left\langle\hat{\mathbf{k}}_0\cdot\hat{\mathbf{k}}_0\right\rangle_f}{\left\langle\hat{\mathbf{k}}_0\right\rangle_f\cdot\left\langle\hat{\mathbf{k}}_0\right\rangle_f}. \tag{II.46}$$

Eq. II.45 describe a scaled Stokes problem for a steady-state viscous flow.

By definition, the high-frequency viscous tortuosity is given as $\alpha_\infty = \lim_{\omega\to\infty}\left(\alpha\left(\omega\right)\right)$ where $\alpha\left(\omega\right)$ is the dynamic viscous tortuosity defined as:

$$\alpha\left(\omega\right) = \frac{\phi\rho_{ef}\left(\omega\right)}{\rho_0} = \frac{\phi\eta}{i\omega\rho_0\mathcal{K}\left(\omega\right)}. \tag{II.47}$$

In high-frequency regime, the viscosity of fluid can be neglected, i.e., $\eta = 0$ and the fluid becomes inviscid. The dynamic Stokes equations II.11, II.8 and II.9 become:

$$-i\omega\rho_0\mathbf{u}^{(0)} = \nabla_x p^{(0)} - \nabla_y p^{(1)} \quad \text{in} \quad \Omega_f, \tag{II.48}$$

$$\nabla_y \cdot \mathbf{u}^{(0)} = 0 \quad \text{in} \quad \Omega_f, \tag{II.49}$$

$$\mathbf{u}^{(0)} \cdot \mathbf{n} = 0 \quad \text{on} \quad \partial\Omega. \tag{II.50}$$

Note that the no-slip boundary condition (II.9) was replaced by the no-penetration condition (II.50), where $\mathbf{n}$ is the normal unit vector of interface boundary $\partial\Omega$. The solution of the velocity $\mathbf{u}^{(0)}$ and the pressure $p^{(0)}$ can be given by [14]:

$$\mathbf{u}^{(0)}\left(x,y\right) = -\frac{\tilde{\underline{\underline{\mathbf{E}}}}\left(y\right)}{i\omega\rho_0} \cdot \nabla_x p^{(0)}\left(x\right), \tag{II.51}$$

$$p^{(1)}\left(x,y\right) = -\tilde{\boldsymbol{\varphi}}\left(y\right) \cdot \nabla_x p^{(0)}\left(x\right) + \bar{p}^{(1)}\left(x\right), \tag{II.52}$$

where $\tilde{\underline{\underline{\mathbf{E}}}}\left(y\right)$, $\tilde{\boldsymbol{\varphi}}\left(y\right)$ are a local tensor and a local vector, respectively, $\bar{p}^{(1)}\left(x\right)$ is a constant. $\tilde{\underline{\underline{\mathbf{E}}}}\left(y\right)$, $\tilde{\boldsymbol{\varphi}}\left(y\right)$ are Ω-periodic fields. In the case of isotropic media or the sound wave propagate in a preferential direction $\mathbf{e}$, by introducing the vector field $\mathbf{E}\left(y\right) = \tilde{\underline{\underline{\mathbf{E}}}}\left(y\right) \cdot \mathbf{e}$ and scalar field $\varphi\left(y\right) = \tilde{\boldsymbol{\varphi}}\left(y\right) \cdot \mathbf{e}$, the choice of locally-constant pressure gradient: $\nabla_x p^{(0)} = \|\nabla_x p^{(0)}\|\mathbf{e}$ leads to:

$$\mathbf{u}^{(0)}\left(x,y\right) = -\frac{\mathbf{E}\left(y\right)}{i\omega\rho_0} \cdot \|\nabla_x p^{(0)}\left(x\right)\|, \tag{II.53}$$

$$p^{(1)}\left(x,y\right) = -\varphi\left(y\right) \cdot \|\nabla_x p^{(0)}\left(x\right)\| + \bar{p}^{(1)}\left(x\right). \tag{II.54}$$

Inserting these relations into Eqs. II.48-II.50, we obtain the electric conduction problem [14, 25]:

$$\begin{gathered}
\mathbf{E} = \mathbf{e} - \nabla_y\varphi \quad \text{in} \quad \Omega_f, \\
\nabla_y \cdot \mathbf{E} = 0 \quad \text{in} \quad \Omega_f, \\
\mathbf{E} \cdot \mathbf{n} = 0 \quad \text{on} \quad \partial\Omega, \\
\mathbf{E} \quad \text{and} \quad \varphi \quad \text{are} \quad \Omega\text{-periodic}.
\end{gathered} \tag{II.55}$$

Here, where $\mathbf{e}$ is a given macroscopic electric field while $\mathbf{E}$ is local electric field, φ being the local electric potential is the solution of the Laplace's problem:

$$\nabla_y^2\varphi = 0 \quad \text{in} \quad \Omega_f, \tag{II.56}$$

$$\nabla_y\varphi \cdot \mathbf{n} = \mathbf{e} \cdot \mathbf{n} \quad \text{on} \quad \partial\Omega. \tag{II.57}$$

Therefore, the high-frequency viscous tortuosity can be calculated as:

$$\alpha_\infty = \frac{\left\langle \mathbf{E} \cdot \mathbf{E} \right\rangle_f}{\left\langle \mathbf{E} \right\rangle_f \cdot \left\langle \mathbf{E} \right\rangle_f}. \tag{II.58}$$

The viscous characteristic length is given as [49]:

$$\Lambda = 2\frac{\int_{\Omega_f} \mathbf{E} \cdot \mathbf{E} dV}{\int_{\partial\Omega} \mathbf{E} \cdot \mathbf{E} dS}. \tag{II.59}$$

Finally, for the thermal effect, the static thermal permeability is defined as $k_0' = \lim_{\omega \to 0} \left(\mathcal{K}'(\omega)\right)$, the scaled dynamic thermal diffusion problem II.27 at $\omega = 0$ becomes the Poisson's equation:

$$\begin{aligned} -\nabla_y^2 \tilde{k}_0' &= 1 \quad \text{in} \quad \Omega_f, \\ \tilde{k}_0' &= 0 \quad \text{on} \quad \partial\Omega, \\ \tilde{k}_0' &\quad \text{is} \quad \Omega\text{-periodic}. \end{aligned} \tag{II.60}$$

Then, the static thermal permeability and the static thermal tortuosity are calculated as:

$$k_0' = \phi \left\langle \tilde{k}_0' \right\rangle_f, \tag{II.61}$$

$$\alpha_0' = \frac{\left\langle \tilde{k}_0'^2 \right\rangle_f}{\left\langle \tilde{k}_0' \right\rangle_f^2}. \tag{II.62}$$

In summary, the so-called hybrid multiscale method resolving three uncoupled, frequency-independent and real-valued problems, i.e., the scaled Stokes problem II.45, the Laplace's problem II.56 and the Poisson's problem II.60 for the transport parameters. These parameters are then used as inputs for each of the semi-phenomenological models, i.e., JCA, JCAL or JCAPL model to approximate effective properties of the porous media studied. This method requires significantly less calculation cost than the direct simulation and direct multiscale method described above and usually provides accurate predictions.

II.5 Biot's theory of poroelasticity for predicting the sound absorption coefficient at normal incidence

When a porous material has elastic skeleton, its effective acoustical properties can be influenced by the deformation of the skeleton. M.A.Biot (1956) proposed a theoretical formalism to describe the elastic wave propagation inside an isotropic porous medium saturated with a fluid [7, 8] where he considered the existence of three waves : two compressional waves and one shear wave with an assumption that the fluid properties can be considered as equivalent to their values when the solid phase is not in motion. In other words, the elastic properties of the material frame are considered independently from the properties of the fluid.

The motion of the poroelastic medium is described by the macroscopic displacement of solid and fluid phases represented by the vectors $\mathbf{u}^s$ and $\mathbf{u}^f$. In the harmonic regime, the equation of motion can be written in the following form [47]:

$$-\omega^2 \left(\tilde{\rho}_{11} + \mathbf{u}^s + \tilde{\rho}_{12}\mathbf{u}^f\right) = \left(P_B - N\right) \nabla\nabla \cdot \mathbf{u}^s + N\nabla^2\mathbf{u}^s + Q_B \nabla\nabla \cdot \mathbf{u}^f, \tag{II.63}$$

$$-\omega^2 \left(\tilde{\rho}_{22}\mathbf{u}^f + \tilde{\rho}_{12}\mathbf{u}^s\right) = R_B \nabla\nabla \cdot \mathbf{u}^f + Q_B \nabla\nabla \cdot \mathbf{u}^s, \tag{II.64}$$

with $\tilde{\rho}_{11}$, $\tilde{\rho}_{22}$ are the Biot's density of the solid and fluid phases, respectively; $\tilde{\rho}_{12}$ is the Biot's density which account for the coupling of the solid and fluid phases:

$$\tilde{\rho}_{11} = \rho_{11} - i\sigma\phi^2 \frac{G(\omega)}{\omega}, \tag{II.65}$$

$$\tilde{\rho}_{22} = \rho_{22} - i\sigma\phi^2 \frac{G(\omega)}{\omega}, \tag{II.66}$$

$$\tilde{\rho}_{12} = \rho_{12} + i\sigma\phi^2 \frac{G(\omega)}{\omega}, \tag{II.67}$$

here $\rho_{12} = -\phi\rho_0\left(\alpha_\infty - 1\right)$; $\rho_{11} = \rho_1 - \rho_{12}$ and $\rho_{22} = \phi\rho_0 - \rho_{12}$. ρ_1 is the mass density of porous material. The coefficient $G\left(\omega\right)$ was first assumed constant by Biot [7, 8] but in order to account for the viscous effect, it was improved by Johnson et al. [49] in the JCA and JCAL models and by Pride et al. [79] in the JCAPL model:

$$G\left(\omega\right)_{\text{Johnson}} = \sqrt{1 + i\frac{4\alpha_\infty^2\eta\rho_0\omega}{\sigma^2\Lambda^2\phi^2}}, \tag{II.68}$$

$$G\left(\omega\right)_{\text{Pride}} = 1 - P + P\sqrt{1 + \frac{M}{2P^2}\frac{i\omega\rho_0 k_0\alpha_\infty}{\eta\phi}}. \tag{II.69}$$

where M and P are non-dimensional shape factors determined by Eq. II.41. Therefore, $\tilde{\rho}_{22} = \phi^2\rho_{ef}$.

In the Eqs. II.63 and II.64, the elastic coefficients P_B, Q_B and R_B are given by:

$$P_B = \frac{4}{3}N + \frac{\left(1-\phi\right)\left(1-\phi-B_b/B_s\right)B_s + \phi K_b B_s/B_f}{1-\phi-B_b/B_s+\phi B_s/B_f}, \tag{II.70}$$

$$Q_B = \frac{\phi B_s\left(1-\phi-B_b/B_s\right)}{1-\phi-B_b/B_s+\phi B_s/B_f}, \tag{II.71}$$

$$R_B = \frac{\phi^2 B_s}{1-\phi-B_b/B_s+\phi B_s/B_f}. \tag{II.72}$$

If the material constituting the frame is not compressible, i.e., $B_s = +\infty$:

$$P_B = \frac{4}{3}N + B_b + \frac{\left(1-\phi\right)^2}{\phi}B_f, \tag{II.73}$$

$$Q_B = B_f\left(1-\phi\right), \tag{II.74}$$

$$R_B = \phi B_f, \tag{II.75}$$

where $B_f = \phi\mathcal{B}_{ef}$ the bulk modulus of the fluid in the pore, the bulk modulus of solid frame B_b can be evaluated by the following equation:

$$B_b = \frac{2N\left(\nu_e+1\right)}{3\left(1-2\nu_e\right)}, \tag{II.76}$$

The shear modulus of the material N is estimated by

$$N = \frac{E\left(1+i\eta_e\right)}{2\left(1+2\nu_e\right)}, \tag{II.77}$$

where E, ν_e, η_e are the Young's modulus, Poisson's coefficient and the loss factor of the frame, respectively.

In a normal acoustic field (normal incidence), the shear wave is not excited and only the compression waves propagate in the material. Let us denote φ^s and φ^f are scalar potentials for the compressional waves in the frame and in the fluid, respectively:

$$\mathbf{u}^s = \nabla\varphi^s, \tag{II.78}$$

$$\mathbf{u}^f = \nabla\varphi^f. \tag{II.79}$$

Eqs. II.63 and II.64 can be reformulated as

$$-\omega^2\begin{bmatrix}P_B & R_B\\ R_B & Q_B\end{bmatrix}^{-1}\begin{bmatrix}\tilde{\rho}_{11} & \tilde{\rho}_{12}\\ \tilde{\rho}_{12} & \tilde{\rho}_{22}\end{bmatrix}\begin{bmatrix}\varphi^s\\ \varphi^f\end{bmatrix} = \nabla^2\begin{bmatrix}\varphi^s\\ \varphi^f\end{bmatrix}, \tag{II.80}$$

The squared complex wave numbers δ_k^2 of the two compressional waves ($k = 1, 2$) are obtained from the eigenvalue problem, $-\delta_k^2 [\varphi_k] = \nabla^2 [\varphi_k]$, given as

$$\delta_k^2 = \frac{\omega^2}{2\left(P_B R_B - Q_B^2\right)} \left[P_B \tilde{\rho}_{22} + R_B \tilde{\rho}_{11} - 2Q_B \tilde{\rho}_{12} \pm \sqrt{\Delta}\right] \quad \text{with} \quad k = 1, 2, \tag{II.81}$$

where

$$\Delta = \left[P_B \tilde{\rho}_{22} + R_B \tilde{\rho}_{11} - 2Q_B \tilde{\rho}_{12}\right]^2 - 4\left(P_B R_B - Q_B^2\right)\left(\tilde{\rho}_{11}\tilde{\rho}_{22} - \tilde{\rho}_{12}^2\right), \tag{II.82}$$

μ_1, μ_2 are the ratio of the velocity of the air over the velocity of the solid phase for the two compressional waves:

$$\mu_k = \frac{P_B \delta_k^2 - \omega^2 \tilde{\rho}_{11}}{\omega^2 \tilde{\rho}_{12} - Q_B \delta_k^2} \quad \text{with} \quad k = 1, 2. \tag{II.83}$$

The characteristic impedances in the solid (superscript s) and fluid phase (superscript f) of first (index 1) and second (index 2) Biot compressional waves Z_k^s, Z_k^f are:

$$Z_k^s = \left(P_B + Q_B \mu_k\right) \frac{\delta_k}{\omega} \quad \text{with} \quad k = 1, 2, \tag{II.84}$$

$$Z_k^f = \left(R_B + \frac{Q_B}{\mu_k}\right) \frac{\delta_k}{\phi\omega} \quad \text{with} \quad k = 1, 2. \tag{II.85}$$

The surface impedance at normal incidence for a H-thickness layer of porous material backed by an impervious rigid wall in that case is predicted by:

$$Z_s^{\text{Biot}} = -i \frac{\left(Z_1^s Z_2^f \mu_2 - Z_2^s Z_1^f \mu_1\right)}{D_Z}, \tag{II.86}$$

where D_Z is given by

$$\begin{aligned} D_Z = {} & \left(1 - \phi + \phi\mu_2\right)\left[Z_1^s - \left(1 - \phi\right) Z_1^f \mu_1\right] \tan\left(\delta_2 H\right) \\ & + \left(1 - \phi + \phi\mu_1\right)\left[\left(1 - \phi\right) Z_2^f \mu_2 - Z_2^s\right] \tan\left(\delta_1 H\right). \end{aligned} \tag{II.87}$$

The sound absorption coefficient is then calculated by Eq. II.34. The model using JCAL (JAC, JCAPL) semi-phenomenological model to estimate the effective properties of fluid (ρ_{ef} & $\mathcal{B}_{ef}$) and the Biot's theory to predict surface impedance at normal incidence is called Biot-JCAL (Biot-JCA, Biot-JCAPL, respectively). This model makes it possible to take into account the effect of elasto-acoustic coupling on the SAC_{NI}.

II.6 Conclusion

Acoustic properties of a rigid-frame porous material can be obtained by a direct simulation of coupled visco-thermal problems in harmonic regime at macroscopic scale or at microscopic scale of a periodic porous domain by direct multi-scale method consisting two uncoupled dynamic visco-thermal problems: the scaled harmonic viscous incompressible flow with no-slip boundary conditions on solid-fluid interface and scaled harmonic thermal diffusion with isothermal boundary conditions on solid-fluid interface. Therefore, the hybrid multi-scale method which rely on three uncoupled frequency-independent problems corresponding to the asymptotic behavior at low frequencies of scaled harmonic viscous flow (scaled Stokes flow) and scaled harmonic thermal diffusion (Poisson's problem) as well as the asymptotic behavior at high frequencies of scaled harmonic

viscous flow (Laplace's problem), gives approximate transport parameters which are the input of the semi-phenomenological models for the estimation of effective properties of equivalent fluid. The Biot's theory assuming the independence of equivalent fluid with the deformation of elastic frame can be used to simulate the effect of the coupled elasto-acoustic on sound absorption coefficient at normal incidence.

Chapter III

Experimental characterization and microstructure reconstruction

Contents

III.1 Introduction

This chapter is devoted to the experimental characterization of both microstructural features and physical properties for polydisperse foams. Here, the foam microstructure is characterized through 2D and 3D imaging, and the information thus obtained is used to generate a periodic representative volume element (PRVE), based on a Laguerre tessellation. These results will be used, in particular, as inputs for subsequent numerical analyses (e.g., as input parameters for the semi-phenomenological JCAL and Biot-JCAL models).

III.2 Graphite polyurethane foams

A polyurethane (PU) foam is a polymer material presenting a cellular structure. It is derived from polyurethane (which is the product resulting from the polymerization of isocyanates and polyols), which is combined with other additives through different foaming techniques (e.g., free rising, water blown, or cast molding). The combustion of PU foam produces large quantities of toxic fumes with high concentration of carbon monoxide and hydrogen cyanide. Graphite particles are commonly introduced during the foaming process to improve fire resistance [101, 33, 105, 106, 21, 108]. The addition of graphite particles affects not only flame retardancy, but also other physical properties such as density, thermal stability, and mechanical properties [21, 68]. In particular, the presence of graphite particles strongly impacts the morphology of the PU foam. Small graphite particles can be wrapped and uniformly dispersed in the foam matrix, hence resulting in a strut-like system, while graphite particles with a size of the same order as pore size tend to be predominantly located between pore walls [70, 68, 63, 21, 65]. High concentrations of large graphite particles having poor compatibility with the foam matrix can ultimately result in the collapse of the pores, which may destroy the closed cellular polyhedra of an otherwise neat foam microstructure [68, 21] (see Fig.III.1).

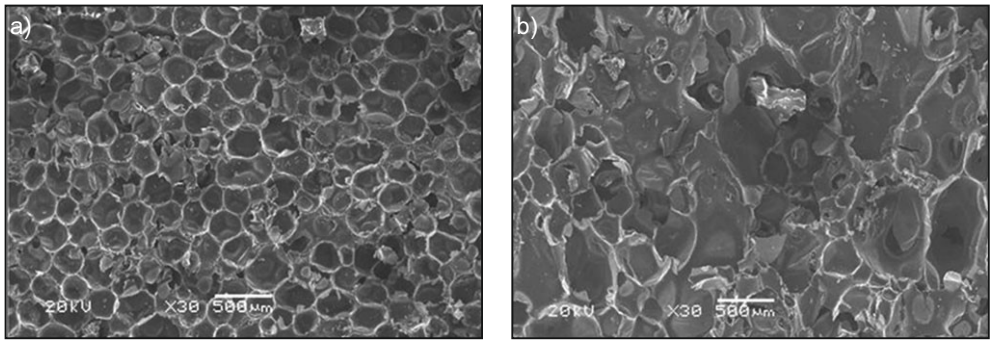

Figure III.1: Micrographs of a pure PU foam (left) and a PU foam with 15 wt% graphite particles (right) [68].

Moreover, the graphite particles were shown to modify the distribution of pore size and to increase the heterogeneity in the PU foam [63, 2]. In this work, we consider a polyurethane foam which is obtained by adding graphite particles during the manufacturing step, following a nucleation perturbation technique. Graphite particles with a so called standard size (DE CH0334) are introduced at 7.3 wt% (≈0.5 mm).

III.3 Experimental characterization of physical properties

As introduced in the previous chapter, numerical approaches for acoustic porous media require the determination of physical properties such as the porosity ϕ, the mass density ρ_1, the static airflow resistivity σ, as well as of the elastic properties: Young's modulus E, Poisson's coefficient ν_e, and loss factor η_e for the application of Biot's theory.

III.3.1 Characterization of open porosity and mass density

Salissou and Panneton [86] developed a pressure/mass method to measure open porosity and mass density of porous materials, based on the perfect gas law. The principle of this method is to measure the mass of a closed chamber at two different pressure states - one with an empty chamber and one with a chamber containing the porous material to be characterized; see Fig. III.2.

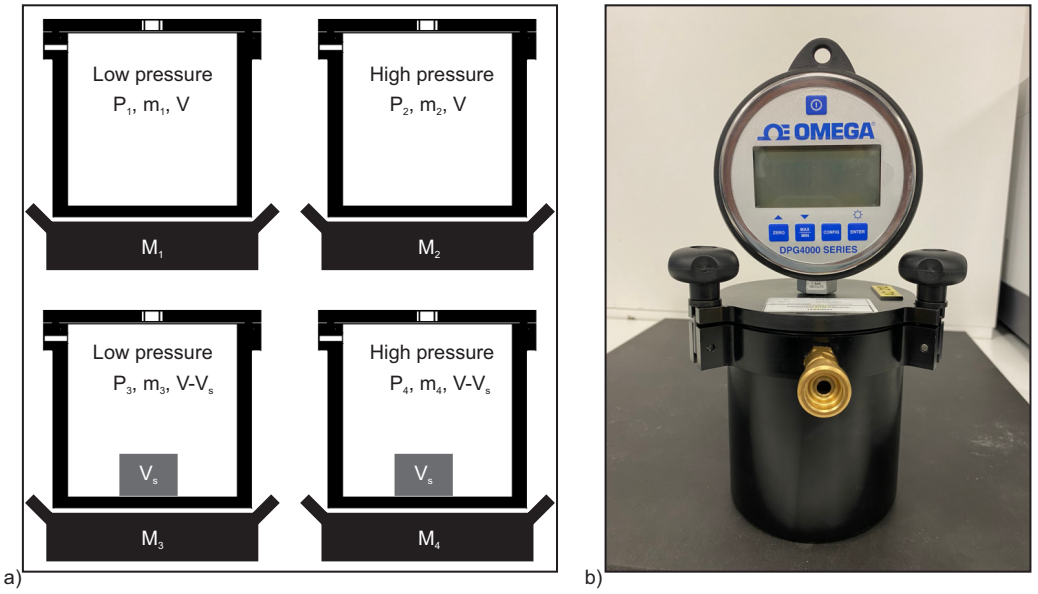

Figure III.2: Measurement of open porosity: a) Schematic of the experimental setup, b) Picture of the chamber containing the porous material (available at CERA).

The open porosity ϕ and the mass density ρ_1 of porous material are determined by the following equations:

$$\phi = 1 - \frac{R_g T}{V_t}\left(\frac{M_2 - M_1}{P_2 - P_1} - \frac{M_4 - M_3}{P_4 - P_3}\right), \tag{III.1}$$

$$\rho_1 = \frac{M_3 - M_1}{V_t} + \frac{(P_1 - P_3)\,V + P_3 V_s}{R_g T V_t}, \tag{III.2}$$

where R_g is the specific gas constant and T is the temperature (in [K]). In addition, V, V_s, and V_t are the volume of chamber at the vacuum condition without sample, the volume of the solid phase, and the total bulk volume of the porous aggregate, respectively. The mass M_i is the total mass measured on the balance, m_i is the mass of gas in the chamber, and P_i is the pressure for the configuration $i \in \{1, 2, 3, 4\}$ illustrated in Fig. III.2 (a). The values of the open porosity ϕ and the density ρ_1 of the material are estimated from three measurements, performed on samples with a thickness estimated to 21 [mm]. These results are listed in Tab. III.1.

Notice that for each measurement, it is necessary to stack up samples to obtain a pile of material with a total height of about 60 [mm] (see Fig. III.3).

	$\phi \pm \delta\,(-)$	ρ_1 [kg/m^3]
Measurement #1	0.912 ± 0.024	13.31
Measurement #2	0.923 ± 0.024	13.59
Measurement #3	0.938 ± 0.017	13.21
Mean $\pm\sigma_X$	0.924 ± 0.013	13.37 ± 0.19

Table III.1: Measured open porosity and mass density of the foam. Here, δ represents the error on the measured open porosity, which is mostly controlled by the uncertainty on mass and pressure reading and the thickness estimation, and σ_X denotes the standard deviation estimated with the experimental values.

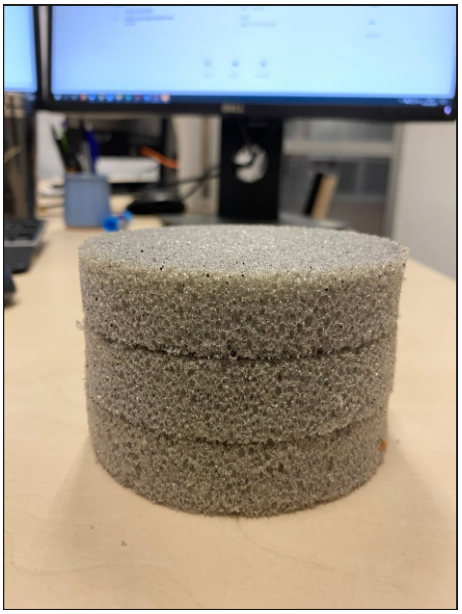

Figure III.3: Stack of samples used for the measurement of the open porosity and mass density.

It can be seen that this foam is lightweight, $\rho_1 = 13.37 \pm 0.19\,\left[kg/m^3\right]$, and exhibits a high porosity rate, $\phi \geq 0.9$.

III.3.2 Characterization of static airflow resistivity

The static airflow resistivity σ [N.s.m^{-4}] is defined as the ratio of pressure difference to flow velocity per unit length. It is related to the static viscous permeability k_0 [m^2] through the viscosity of the air saturating the interconnected pores, $\eta = \sigma k_0$ [Pa.s]. This parameter is often measured by a standard test method described in DIN EN 29053 (ISO 9053), based on the work of Stinson and Daigle [93]. The airflow resistance is determined by measuring the pressure drop between the two faces of a sample, subjected to a constant laminar air flow. The air flow is generated by a compressor and controlled by a mass flow meter. The pressure difference ΔP [Pa] is measured for several flow velocities, all greater than 0.5 [mm/s], and the value at velocity 0.5 [mm/s] (which is recommended by the ISO standard) is typically estimated by means of a linear regression. The airflow resistance R_f [N.s.m^{-3}] is calculated through the volume flow Q_f [m^3/s] and sample surface A_s [m^2]:

$$R_f = \frac{\Delta P}{Q_f} A_s \,. \tag{III.3}$$

Finally, the static airflow resistivity σ can be deduced as

$$\sigma = R_f / t_s \ , \tag{III.4}$$

where t_s [m] denotes the thickness of the sample. In this work, an AFD 300 - AcoustiFlow airflow resistivity meter was used to conduct measurements for airflow resistivity (see Fig. III.4).

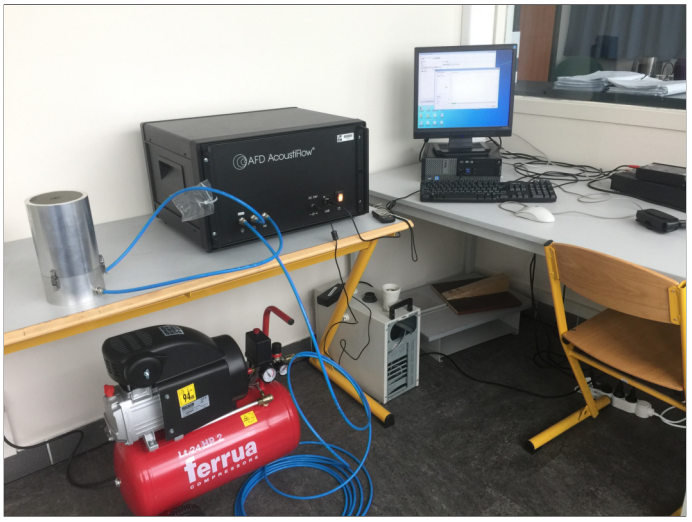

Figure III.4: AFD 300 - AcoustiFlow Airflow resistivity meter.

Results for static airflow resistivity measurements on 6 foam samples (21 [mm] in thickness; see Fig. III.5) are provided in Tab III.2. It should be noted that these samples are those used for

Sample #	$\sigma \pm \delta\sigma$ [N.s.m^{-4}]
A_I	55600 ± 3000
A_{II}	65400 ± 2700
B_I	73500 ± 9700
B_{II}	80100 ± 6300
C_I	65100 ± 7100
C_{II}	65400 ± 3000
Mean $\pm\sigma_X$	67500 ± 9900

Table III.2: Static airflow resistivity measured on 6 foam samples. Here, $\delta\sigma$ represents the uncertainty due to the equipment, and σ_X denotes the standard deviation over all measurements.

open porosity measurements, and that the coefficient of variation between the results (about 14%) indicates significant heterogeneity between foam samples.

III.3.3 Visco-elastic parameters

The visco-elastic parameters such as the Young's modulus E, the Poisson's coefficient ν_e, and the lose factor η_e can be estimated by the dynamic method of quasi-static compression, proposed by C. Langlois et al. [57]. In this method, the porous sample is positioned between two rigid plates, and an accelerometer is fixed to the bottom plate to measure the vertical acceleration $a\,(\omega)$. The top plate is mounted on a force transducer, fixed to a rigid wall, to measure the reaction force $F\,(\omega)$. This system is then put on a shaker driven by a pseudo-random noise, as illustrated in Fig. III.6.

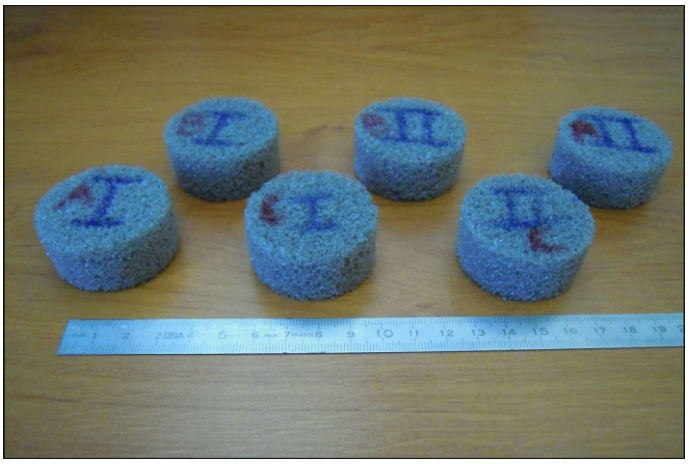

Figure III.5: Samples used for the characterization of the resistivity and acoustic properties.

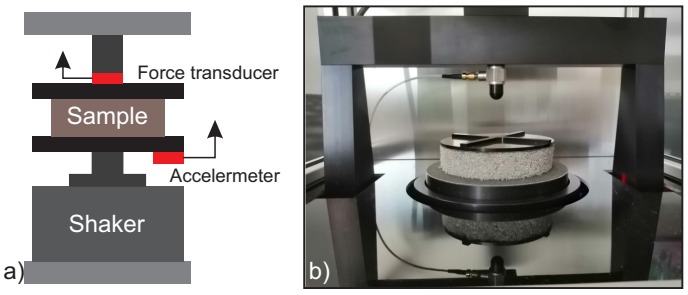

Figure III.6: Elastic parameter measurements: a) Schematic of the experimental setup, b) Picture of the setup including the foam sample.

The mechanical impedance, defined as $Z_m(\omega) = K_m(\omega)\left(1 + i\eta_e(\omega)\right)$, is computed from the reaction force $F(\omega)$ and the acceleration $a(\omega)$. The apparent compression stiffness $K_m(\omega)$ and the loss factor $\eta_e(\omega)$ are then obtained as:

$$K_m(\omega) = \Re\left(Z_m(\omega)\right) , \tag{III.5}$$

$$\eta_e(\omega) = \frac{\Re\left(Z_m(\omega)\right)}{\Im\left(Z_m(\omega)\right)} . \tag{III.6}$$

Furthermore, the apparent Young's modulus is given by:

$$E' = \lim_{\omega \to 0} K_m(\omega) \frac{t_s}{A_s} , \tag{III.7}$$

where t_s and A_s are the thickness and cross-section of the sample, respectively. The ratio of apparent Young's modulus E' to the intrinsic Young's modulus E defines a polynomial P that depends on both the Poisson's coefficient ν_e and the shape factor f^{sh}, which is defined as half the radius to the thickness ratio of the sample (that is, $f^{sh} = r_s/2t_s$). The polynomials $P\left(\nu_e, f_2^{sh}\right)$ are pre-computed by EFM simulations (Fig. III.7 left part). By testing two samples with two different shape factors, Poisson's coefficient ν_e can be estimated by solving the nonlinear equation (Fig. III.7 right part):

$$\frac{E_1'}{P_1\left(\nu_e, f_1^{sh}\right)} = \frac{E_2'}{P_2\left(\nu_e, f_2^{sh}\right)} . \tag{III.8}$$

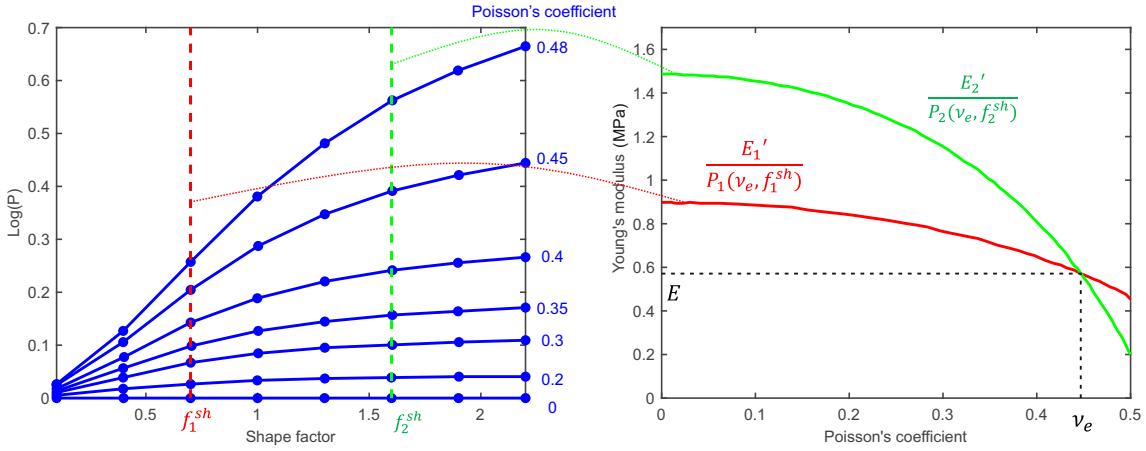

Figure III.7: Estimation of Young's modulus and Poisson's coefficient of porous material by polynomial relations [57].

In this work, two different form samples are utilized, with diameters $\Phi = 40$ [mm] and $\Phi = 100$ [mm] (the latter being used for porosity and static resistivity measurements). Measurement conditions were as follows: the ambient temperature was 25 [C], the ambient pressure was 1.003 [hPa], the applied compression rate was set to 1%, and the frequency interval was $[20 - 60]$ [Hz]. The results are given below, in Tab. III.3.

Test #	E [kPa]	η_e	ν_e
1	172	0.164	0.49
2	137	0.163	0.49
3	134	0.154	0.43
4	198	0.152	0.46
5	185	0.151	0.47
6	180	0.161	0.44
7	189	0.158	0.46
8	177	0.158	0.47
9	173	0.152	0.47
Mean $\pm\sigma_X$	172 ± 19	0.157 ± 0.005	0.46 ± 0.02

Table III.3: Measured elastic parameters for the foam. Here, σ_X denotes the standard deviation over the nine samples.

III.4 Characterization of the microstructure

The properties of a material strongly depend on its microstructure. The characterization of a porous material is often carried out by 2D or/and 3D imaging techniques. Many 2D imaging techniques such as optical microscopy and scanning and transmission electron microscopy can be used for microstructural characterization. Optical microscopy allows for an observation on the shapes, dimensions, and morphology of the microstructure in a near-planar representation. It is inexpensive and easy to use, but its magnification is usually less than 1500 (resolution of a few tens of micrometers). In many cases, optical microscopy is supplemented by scanning electron microscopy (SEM). In general, SEM provides a much finer resolution, on the order of a nanometer. Regarding the analysis of foams, the geometry of the struts (e.g., their lengths and

thicknesses) and cells (including their sizes and anisotropy degrees) can be extracted from the images [43, 76, 15]. Furthermore, overall information related to the existence of membranes can simply be quantified by evaluating the ratio of the numbers of open and partially-open membranes [29, 94, 37, 97]. X-ray microtomography is a 3D imaging technique allowing one to visualize interior features of materials by reconstructing a three dimensional representation. It provides an accurate and detailed information of the microstructure. However, visualizing thin membranes (with a thickness less than one micrometer) requires a scanner with high resolution (in the order of a few nanometers), which leads to a high cost in terms of scanning time and image processing. Thus, the X-ray microtomography is often coupled with 2D imaging (e.g., optical microscopy or/and SEM) to characterize foam microstructures [37]: the struts and pore size distribution are specifically extracted from X-ray microtomography, while membrane opening and distribution are obtained from the 2D images.

In this work, the microstructure of PU foams is characterized using both X-ray CT and SEM. The X-ray CT will be used for the characterization of pore size, sphericity, and number of neighbors. Membrane properties (including the thickness, the opening, and the number of edges per membrane) will be studied on the SEM images.

III.4.1 Pore size and sphericity

X-ray CT setup

X-ray microtomography involves measuring the X-ray intensity of an incident beam, before and after it passes through the sample. In this method, the sample is positioned on a rotating support and a source sends an X-ray beam on the sample. The transmitted beam is recorded by a two-dimensional detector which is generally a combination of a charged coupled device (CCD) sensor and a scintillator screen (i.e., a material that converts X-ray energy to visible light)—for various angular positions of the sample. The ratio between the incident and transmitted photon numbers is then used to digitally reconstruct a 3D image. A schematic illustration of X-ray microtomography is presented in Fig. III.8a).

In this work, X-Ray micro-tomography experiments were performed at the F2M microtomography platform (Ultratom from RX-Solution — see Fig. III.8b), using a micro-focus source Hamamatsu (230 kV or 160kV) and a "flat-panel" imager Varian (or Photonic Science). A cylindrical sample of the graphite PU foam (diameter: 3-5 [mm]; height: 15-20 [mm]) was scanned with a spatial resolution of 6 μm/voxel. For the preliminary test, tube voltage and current were set to 60 [kV] and 100 [μA], respectively.

X-ray CT images processing

Adapted filters and a binarization are needed to reconstruct the struts in foam images. Fig. III.9 shows a μCT image and the strut system reconstructed on the PU foam studied in this thesis with membranes.

It can be seen in the resulting 3D images that the pores are usually connected, even in the ideal closed-cell foams (due to the fact that membranes often disappear because of poor X-ray mass attenuation coefficients). Therefore, for further morphological analysis, the pores have to be separated as individual ones, which requires some additional steps of processing involving, e.g., a watershed transform [71, 73, 98].

In this study, X-ray CT image processing for graphite PU foams are performed as follows:

1. First, noise elimination is performed by selecting the domain center, and by applying a ball-shaped dilatation filter with a radius of 2 voxels.

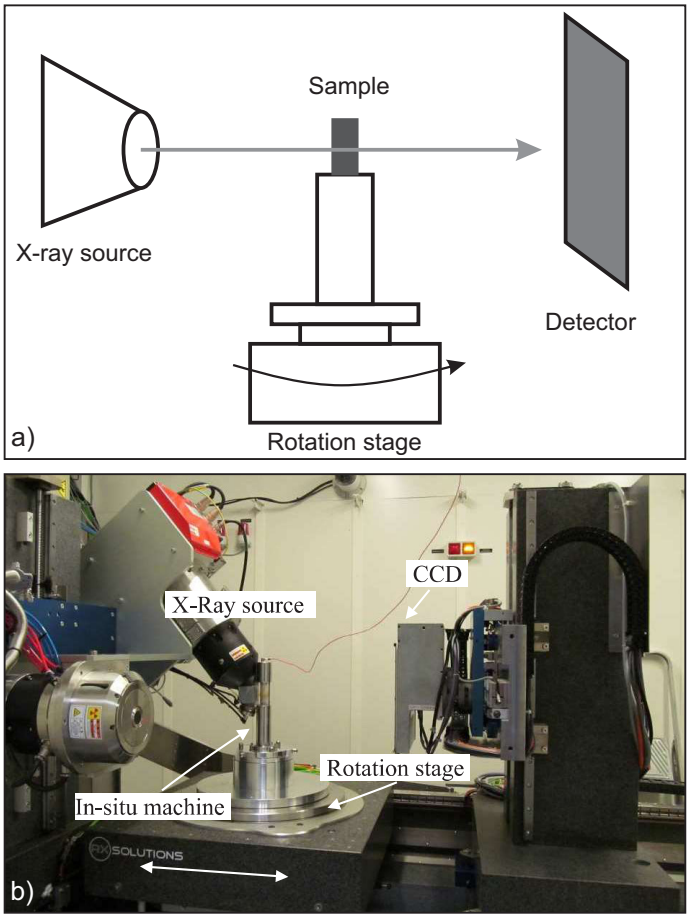

Figure III.8: Micro X-ray measurements: a) Schematic of the system, b) Picture of the experimental setup [72].

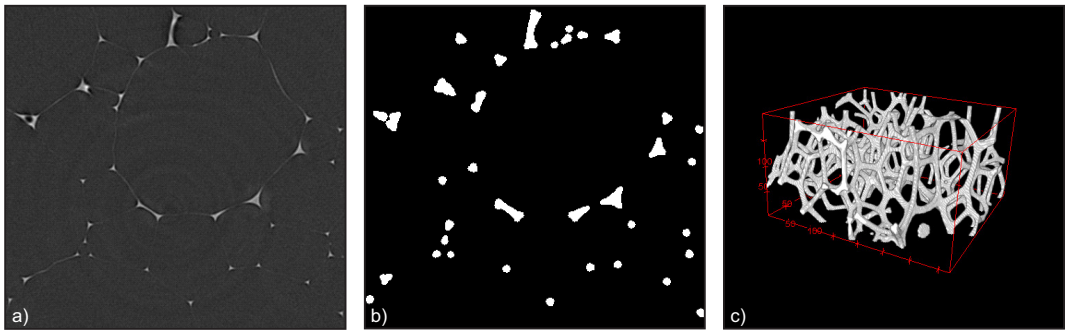

Figure III.9: Example of μCT image processing for a PU foam with membranes: a) Original image, b) Binarized image, c) Strut system reconstruction.

2. Second, foam struts are obtained through a binarization, by applying Ostu's method [74] with an adapted threshold (which is calculated on the fly for each image).

3. Third, a 3D distance transform map of individual pores is computed, together with an inversion of the images obtained in the second step.

4. Last, a segmentation by watershed transform is performed to detect the borders separating one pore from the others, and the pores thus detected are colored.

When the above procedure is performed as illustrated in Fig. III.10, the distribution of pore size can be estimated from the 3D reconstructed foam.

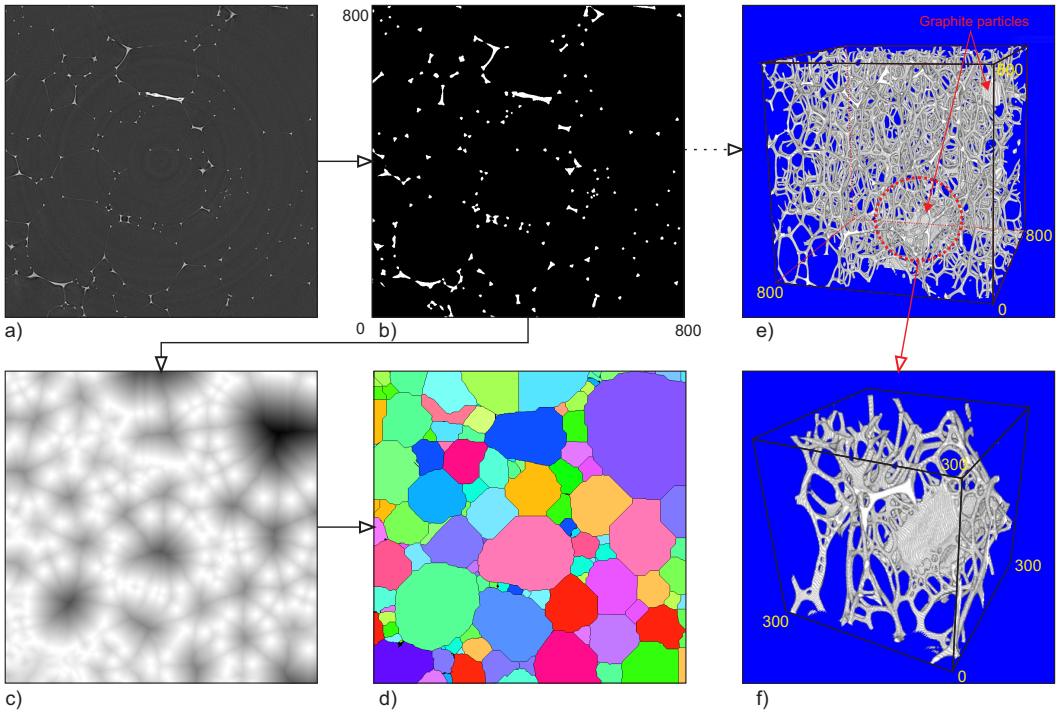

Figure III.10: Detection and pore size distribution from X-ray μCT and image analysis. a) Original image. b) Binarized image generating the strut system of the foam. c) Image obtained after distance transform and inversion. d) Coloration of the pores detected after segmentation (by watershed transform). e) and f) 3D visualization of the strut system and graphite particles.

It should be noticed that the procedure also provides us with the relative position of each pore, together with the corresponding neighboring pores. In order to proceed with pore size estimation, only complete pores were considered (that is, pores intersecting image borders were be discarded). On the contrary, pores located at the borders were preserved to estimate the number of neighbors for the complete pores. All image processing and analysis steps were carried out by using the open-source FIJI software with the MorphoLibJ plugins [61, 89].

In the pore size distribution, the pore size is represented by a so-called equivalent diameter d, which represents the diameter of a sphere with a volume equivalent to the volume of the corresponding pore. From now on, and unless otherwise stated, the pore size and normalized pore size will be referred to as d and $d/\langle d\rangle$, respectively, where $\langle d\rangle$ is the average diameter over all pores. It is necessary to distinguish between the average of equivalent diameters $\langle d\rangle$ and the equivalent diameter of a sphere with average volume D.

The pore sphericity index s, which can be defined as the ratio of the surface area of the sphere of equivalent volume to the surface area S of the corresponding pore, is another interesting shape parameter. The pore sphericity index takes a maximal value of one for a spherical pore and takes smaller values if the pore shape significantly differs from a sphere. This index is defined by:

$$s = \left(36\pi \frac{V^2}{S^3}\right)^{1/3}, \tag{III.9}$$

and is applicable to represent the anisotropic character of the pores.

A 3D visualization of strut system is shown in Fig. III.10, e) and f). The effect of graphite particles on the foam structure can be observed: small pores were created around the graphite particles that contribute to the rigid skeleton. In this work, a volume of $6 \times 6 \times 6$ [mm^3] containing 2131 pores was analyzed. The distribution of pore size, together with the complement of the sphericity index $1 - s$, are shown in Fig. III.16.

III.4.2 Membrane characterization

The characterization of membranes is performed by analyzing the surfaces of foam samples in SEM images. SEM is based on the detection of secondary electrons emerging from the surface under the impact of a very fine brush of primary electrons (sweeping across the observed surface). It therefore requires electrically conductive materials. For non-conductive materials, a metallization of the samples is needed. A high performance metallizer by cathode sputtering, coupled with a magnetron source (Cressington sputter coater 208HR), makes it possible to deposit a conductive film of a few nanometers (controlled by a quartz probe, here a Cressington MTM 20) on the surface of the samples. Fig. III.11 shows a picture of the MERLIN - Carl Zeiss Scanning Electronics Microscope system used in this study.

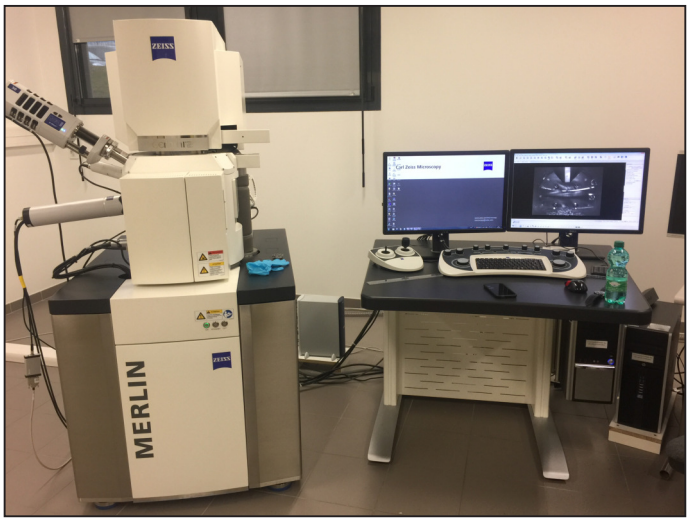

Figure III.11: Picture of the Scanning Electronics Microscope system (available at the Institute of Chemistry and Materials of Paris-Est University (ICMPE), France).

A polygon is superimposed over each individual window in the images thus obtained. For each open membrane, an another polygon is used to characterize the area of the corresponding aperture size (see Fig. III.12). The area of the superimposed polygons is then determined. The proportions of closed and open membranes, which are denoted by x_c and x_o respectively, are also identified. The aperture ratio of open membranes is estimated as $t_o = \sqrt{A_{ap}/A_{ow}}$, where A_{ow} is the area of a polygon corresponding to a window for which the membrane is open, and A_{ap} is the area of the polygon associated with the given aperture. Note that if a membrane has several apertures, A_{ow} is their total area. The average of aperture ratio $\langle t_o \rangle$ is subsequently deduced. The number of edges per membrane N_e is also characterized. Due to sample cutting, some membranes may be destroyed or damaged, in which case they are discarded in the analysis.

For the PU foam under study, dozens of SEM images associated with both the top and bottom sample surfaces were analyzed, leading to the characterization of hundreds of membranes. The foam presents many fully-closed membranes. The mean value for the proportion of fully-closed

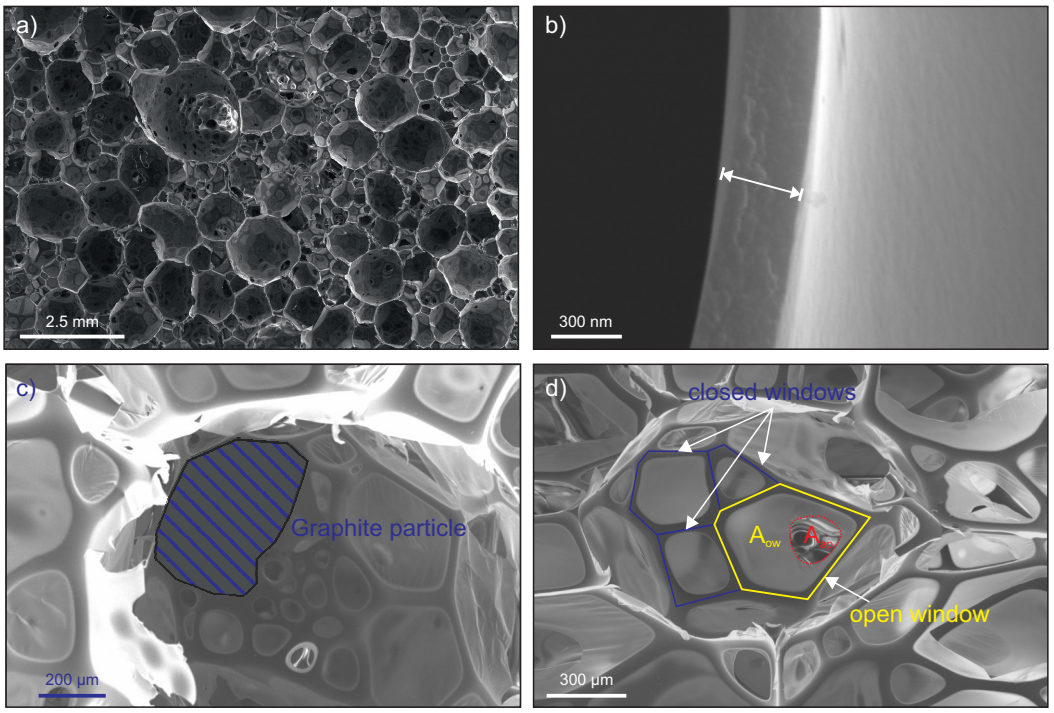

Figure III.12: Characterization of membranes on SEM images: top view of foam sample (a), membrane thickness (b), graphite particle (c), and open membrane aperture ratio (d).

membranes is $\langle x_c \rangle = 0.72$, and the average of aperture ratio for the open membranes is estimated to $\langle\, t_o \rangle = 0.51$ (see Tab. III.4).

d [μm]	$1 - s$ [–]	$\langle x_o \rangle$ [–]	$\langle t_o \rangle$ [–]
360 ± 290	0.23 ± 0.068	0.28 ± 0.05	0.51 ± 0.17

Table III.4: Geometrical properties of the PU foam.

The thickness of a membrane is also estimated through SEM images (see Fig. III.12b). Its average value is in the order of a magnitude of 0.3 [μm], which is slightly smaller than the values reported elsewhere for polyurethane foams [37, 97]. One can note that the membrane thickness is very thin when compared to the average pore size $\langle d \rangle = 360$ [μm]. This property will be used later on to justify that the thickness of the walls separating the cells can be ignored (in order to reduce the size of the finite element model; see chapter VI).

III.5 Microstructure reconstruction and discussion

As discussed in the previous section dedicated to 2D/3D image processing, the studied foam samples exhibit a complex cellular structure comprised of struts (or ligaments, or Plateau borders) and membranes. The membranes can be closed, open, or totally missing, hence allowing the pores to be connected through windows. The local microstructure obeys Plateau's laws [52]:

1. Each membrane has a constant mean curvature, to balance the pressure difference between adjacent pores;

2. Three membranes meet at equal dihedral angles of 120° at each strut; and

3. Four struts join at equal tetrahedral angles of $109.47°$ at each node.

The struts have a concave triangular section and a locally varying thickness, which is highest at the junction (node) and minimal at the center (see Fig. III.12).

From a modeling viewpoint, foams are usually represented as an irregular packing of space-filling polyhedrons. Kelvin-cell structures, which are tetrakaidecahedron cells that can fully fill the space and almost minimize the surface energy [96], are widely employed to model monodisperse foams. Several studies on the Kelvin-cell structure have shown that the acoustic behavior of foams can be controlled by the presence of membranes [94, 29, 37, 97]. However, the Kelvin-cell structure cannot describe the effect of a wide distribution of pore size in polydisperse foams. To circumvent this issue, a systematic procedure for the virtual reconstruction of foam structures based on a random Laguerre tessellation is presented in the next section.

III.5.1 Laguerre tessellation based on a random sphere packing

A random Laguerre tessellation is essentially a weighted generalization of the well-known Voronoi tessellation. Its construction proceeds as follows (in $\mathbb{R}^3$) [4]. Consider a set of random spheres

$$S = \{s_i(\mathbf{x}_i, r_i),\ \mathbf{x}_i \in \mathbb{R}^3,\ r_i > 0,\ i \geq 1\}, \tag{III.10}$$

in $\mathbb{R}^3$, where $\mathbf{x}_i$ and r_i are the center and radius of the sphere s_i, respectively. The 3D space is then filled with a system of convex polytopes, the so-called Laguerre cells $C = \{c_i,\ i \geq 1\}$, which are defined as

$$c_i = \{\mathbf{x} \in \mathbb{R}^3 : \|\mathbf{x} - \mathbf{x}_i\|^2 - r_i^2 \leq \left\|\mathbf{x} - \mathbf{x}_j\right\|^2 - r_j^2,\ \forall j \neq i\}\ , \tag{III.11}$$

where $\|\cdot\|$ denotes the Euclidean norm in $\mathbb{R}^3$. If all the spheres have the same radius, then the classical Voronoi tessellation is obtained. Because cell facets are not forced to be equidistant to the cell generators (i.e., the center of the sphere), the Laguerre tessellation is able to generate a wider range of morphologies as compared to the Voronoi tessellation. Note that, in $\mathbb{R}^3$, the Laguerre tessellations are a *normal* tessellation [60], which means that each facet is the intersection of exactly two cells and each edge is the intersection of exactly three facets. For a detailed discussion about Laguerre tessellations, we refer the reader to [60, 4] for instance.

For foam reconstruction, the Laguerre tessellation often relies on the centers and radii obtained by a random multi-sized dense sphere packing. There are many methods to generate a random dense multi-sized sphere packing, e.g., sequential deposition, molecular dynamics, or collective rearrangement methods [16]. An example of foam structure reconstruction based on the discrete element method (with sphere packing generated with the open source code LIGGGHTS [103]) is shown in Fig. III.13. Here, N spherical particles with an arbitrary radius distribution are randomly generated within a cube, with no initial velocity. In the initial state, we have a system of overlapping spheres. Spheres are then allowed to drift because of an elastic repulsive force (with pair interactions), defined by the Hertz model [107]. In order to avoid boundary effects, periodic boundary conditions are imposed. When a steady state is reached (i.e., zero velocity for all spheres), the simulation stops. The dimensions of the cube are chosen to obtain the desired volume fraction of packing, given by $f_p = \sum V_{\text{sphere}}/V_{\text{cube}}$. In Fig. III.13, a), sphere packing is generated with $N = 100$, $f_p = 0.7$, and sphere volume is assumed to follow a Gamma distribution.

III.5.2 Fitting Laguerre tessellations to foam structures

The Laguerre tessellation strongly depends on the sphere packing simulation. In practice, input parameters must be calibrated in order to represent a particular foam structure, which is an inverse problem that can be solved by minimizing the discrepancy between the model predictions

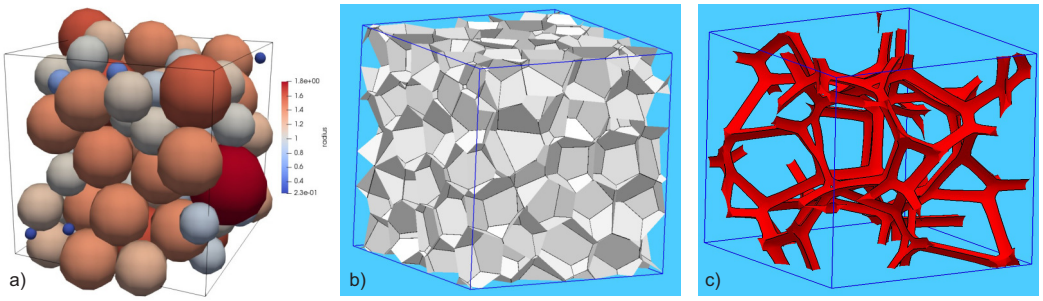

Figure III.13: Reconstruction of a foam structure: a) Random sphere packing, b) Laguerre tessellation, c) Plateau borders.

and physical foam data. A simple least-square method can be used, in which case one seeks to minimize the objective function

$$\rho\left(\mathbf{w}\right) = \sqrt{\sum_{i=1}^{n} \left(\frac{c_i(\mathbf{w}) - \tilde{c_i}}{\tilde{c_i}} \right)^2}, \tag{III.12}$$

where $\mathbf{w}$ conceptually denotes the set of parameters to be identified and the sets $\tilde{c} = \{\tilde{c_i}\}$ and $c = \{c_i\}$ gather morphological characteristics of the pores in the physical and generated data, respectively [82]. Various characteristics can be selected, including all second-order moments for the volume, surface area, number of neighbors, and diameter of the pores. This method was used to study the elastic properties of closed foams with strongly varying pore sizes in [81], and of open-cells foams in [64]. One drawback of this strategy is that it requires a large amount of tessellation-based data to assess model adequacy. In addition, the simulation-based pore size distribution is generally found in poor agreement with experimental data. The quality of the porous structure thus obtained (and particularly, the edge-length distribution) may be improved through a relaxation with Surface Evolver [13]; see [98]. In order to generate the Plateau borders (see Fig. III.13c), tessellation edges are first replaced by struts with triangular sections, and the system of cells and struts is then relaxed by Surface Evolver. Finally, tessellation faces can be perforated to simulate open membranes.

III.5.3 Microstructure reconstruction using Neper software

Recently, R. Quey et al. [80] developed an improved algorithm involving Laguerre tessellations for the polyhedral description of 3D polycrystals. The principle is to sequentially update the parameters of the seeds in the tessellation model, optimizing through a genetic algorithm until some pore properties match with the properties extracted from the experimental data. This strategy was shown to reproduce the pore size, the pore sphericity distribution, and the number of neighbors satisfactorily. This algorithm is available in the open-source package Neper, which was used in this thesis to generate virtual microstructures of foams.

Because the graphite PU foam is highly porous and exhibits many thin membranes, membrane thickness and Plateau's borders are not modeled (which reduces the computational cost associated with subsequent finite element analyses). The proportion of open membranes x_o and the aperture ratio t_o for the open membranes are taken into account through their average values $\langle x_o \rangle$ and $\langle t_o \rangle$ as follows:

1. A fraction of $\langle x_o \rangle$ membranes are randomly selected amongst all membranes. These membranes will be opened with the same aperture ratio $\langle t_o \rangle$.

2. The graphite PU foam structures are generated with the Neper software. Here, the pore size and the sphericity s (or equivalently, the transformed variable $1-s$) are assumed to follow probability laws which are identified using the experiments (see Fig. III.16).

3. The structures are then imported in COMSOL (as STL files) to open the membranes (see Fig. III.14). In order to open a membrane, the centroid C of the membrane under consideration (polygon form) is computed, and the initial polygon is scaled by a factor $\langle t_o \rangle$ (homothety with respect to C). The initial polygon is then perforated using a Boolean operation (subtraction).

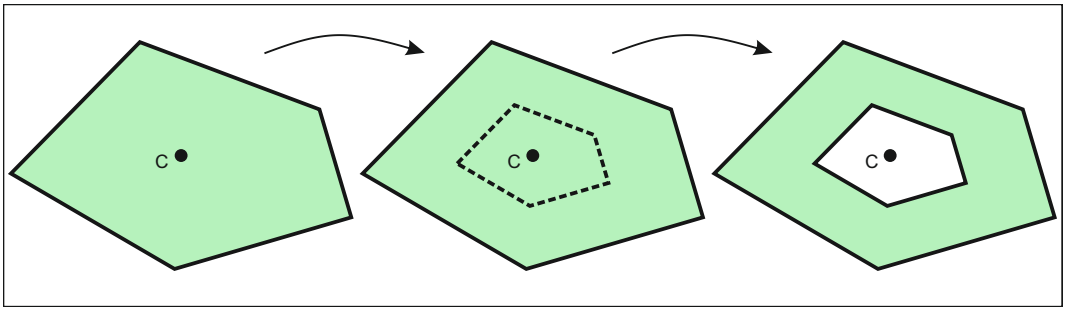

Figure III.14: Schematic of the opening procedure for a membrane.

With a view towards finite element discretization, it is recommended to discard small faces (or membranes) in the opening procedure. Specifically, facets are ignored when the condition $\lambda < \epsilon\langle\lambda\rangle$ is met, where λ is the facet area, $\langle\lambda\rangle$ is the average area, and ϵ is a given threshold which is typically taken as $0.01 \leq \epsilon \leq 0.10$ [53]. In this work, we used $\epsilon = 0.05$ for the sake of regularization. Fig. III.15 shows a configuration of periodic geometry of 453 pores and corresponding mesh.

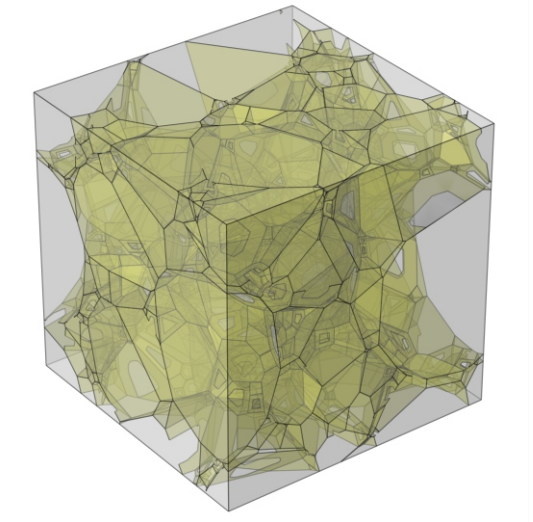

Figure III.15: Periodic geometry of a foam containing 453 pores.

In Fig. III.16, we show the probability density functions of pore size and $1-s$ estimated from the data, fitted with lognormal models, and estimated after the reconstruction.

The coefficient of variation for the pore size is estimated to $c = \sigma_d/\langle d \rangle = 0.79$ (with σ_d the standard deviation of the pore size d), which indicates significant variability. The lognormal fit for

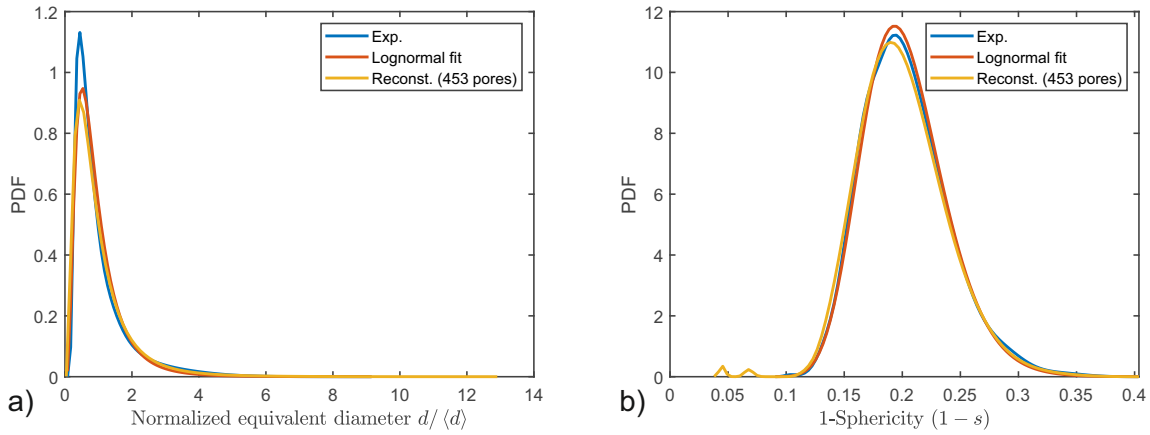

Figure III.16: Reconstructed (orange solid line), reference (blue solid line), and fitted (red solid line) probability density functions for (a) pore size distribution and (b) the quantity $1-s$.

the pore size distribution is found in good agreement with the experimental results, with is consistent with other results provided elsewhere for cellular materials [82]. Similarly, the lognormal fit provides a fairly good approximation of the empirical function for the quantity $1-s$ (recall that s is the sphericity). It is seen that the distributions for the pore diameter and sphericity are properly captured in the proposed methodology.

In order to further discuss model adequacy, results on various quantities of interest obtained through the experimental characterization and through the numerical reconstruction (with 453 pores) are shown in Fig. III.17.

The number of neighboring pores in the reconstructed structure is $N_v = 12.5 \pm 8.9$, which is larger than the corresponding number $N_v = 9.1 \pm 8.6$ in the physical foam. This discrepancy could be explained by a number of factors. First, simulated pores are modeled as convex polyhedrons with straight struts, which is a simplification with regard to the complexity of the real foam structure. Second, the presence of graphite particles can affect the polyhedral microstructure of PU foams, hence decreasing the number of neighboring pores [68, 21]. A small value for the number of neighboring pores could also be induced by the pore size distribution, as shown in [54, 98]. Fig. III.17, b), suggests that the number of neighboring pores and pore size are, indeed, correlated—small pores have fewer neighbors than larger ones, in both the experimental and simulated results. On the other hand, the average number of edges per face for the simulated microstructure, 5.07 ± 1.39, is close to the value obtained on the experimental microstructure, 5.07 ± 1.31 (see Fig.III.17, (c)).

These results support the relevance of the proposed methodology to sample microstructures on graphite PU foams.

III.6 Conclusion

In this chapter, we presented the experimental methodologies used to characterize morphological and elastic properties on graphite PU foams. It was shown that the foam sample under investigation is lightweight, highly porous, and exhibits significant spatial heterogeneity in terms of airflow resistivity.

The foam microstructure was characterized through X-ray CT microtomography and SEM. The former technology was used to extract the distributions of pore size, pore sphericity, and number of neighboring pores. SEM images were used to estimate the average proportion of closed/open

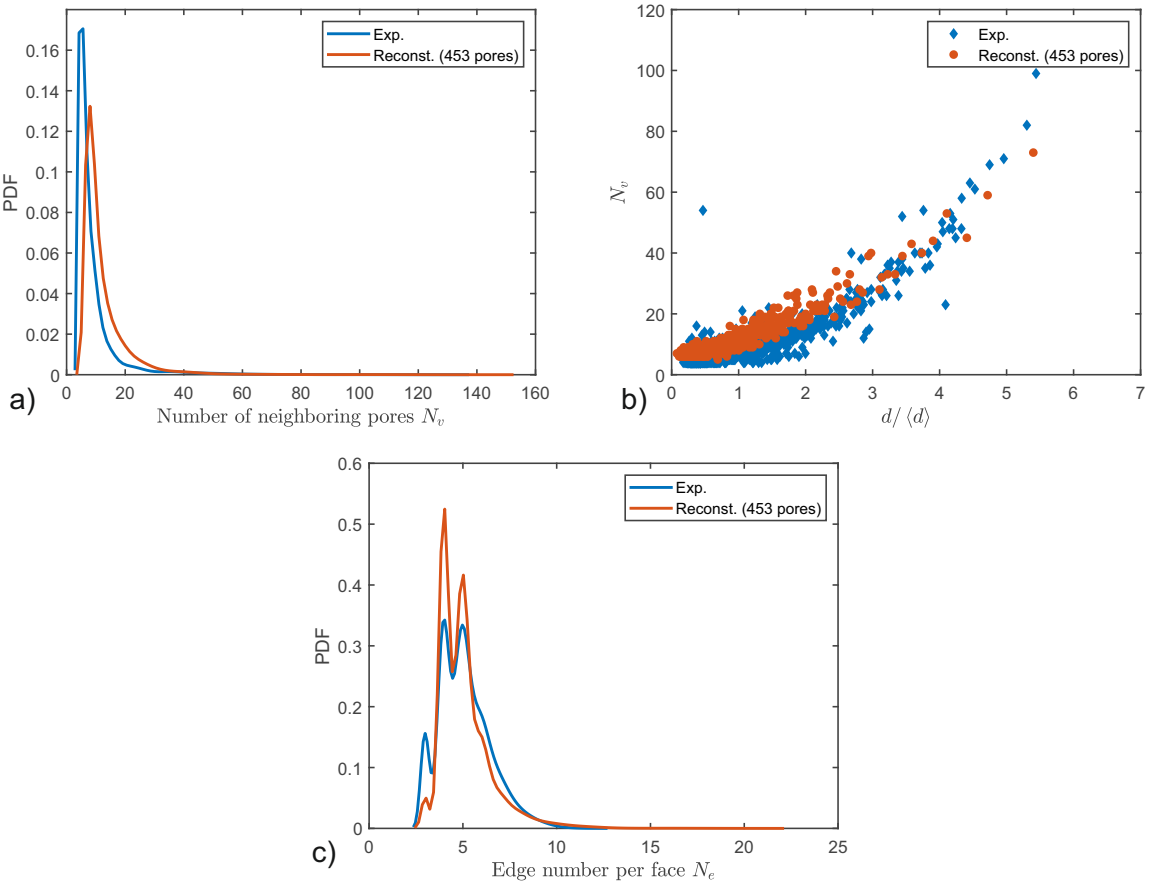

Figure III.17: Comparison of foam morphology between the experimental results and the data estimated on the numerical model, for (a) the number of neighbor, (b) the correlation between the number of neighbors and the normalized equivalent diameter, and (c) the number of edges per face.

membranes, as well as the average aperture ratio of open membranes. Data show that the foam contains many membranes and has a wide pore size distribution, which could be related to graphite particle addition during the fabrication stage. The pore size and pore sphericity distributions can be well approximated by lognormal models.

A Laguerre tessellation was used to reconstruct a periodic representative volume element of the foam. Parameters in the numerical model were calibrated by solving an inverse problem involving experimentally determined morphological properties. Model adequacy was finally confirmed by comparing a set of relevant morphological properties on digital and physical microstructural data.

Chapter IV

Static permeability of polydisperse foams

Contents

IV.1 Introduction

Fluid flow through solid foam is involved in various applications, such as heat-exchanger, catalyser, filter, acoustic insulator,... [28]. Therefore, for such applications, the permeability is a key parameter to control and to ensure the efficiency of foam material.

Different works have focused on morphological parameters - pore or strut diameter, porosity, specific surface area, interpore aperture size, etc. - on permeability of monodisperse open-cell foam [28, 32, 55]. The effect of partially or fully closed membranes on foam permeability have recently been investigated [58].

Different approaches for modelling foam permeability can be found in the literature. A first approach is based on the so-called Carman-Kozeny equation [18]: $K = C((1-\phi)^2/\phi^3)d_c^2$ where d_c is the inverse of the specific surface area a_c (pore surface/solid volume), ϕ is the porosity, and C is a dimensionless constant depending on the microstructure geometry. In the case of foam permeability, some alternative choices for the characteristic micro-structure length d_c have been proposed in the literature, such as the pore size or the hydraulic radius $d_h = 4\phi/a_c$ (see [55] for a recent review). As C depends on the microstructure geometry, these approaches cannot give a full analytical formulation and require numerical calculations to elucidate the relationship between C and the microstructure geometry.

A second approach, especially relevant for foam having membranes [58] or porous media having small constrictions connecting large pores [28, 78], was suggested by Despois and Mortensen [28]. In this approach, the fluid flow passing through constrictions is supposed to be governed by the difference of fluid pressures between interconnected pores. The relationship between fluid flow and pressure drop used by Despois and Mortensen is due to Sampson's law [88]. For monodisperse foam, the foam permeability can be fully derived by considering PUC symmetries in the case of ordered foams [58], or by considering a mean pore in the case of disordered foams [78]. This approach gives a very accurate estimation of foam permeability in a large range of constriction sizes. Moreover, this approach is similar to the pore-network approach introduced by Fatt [34] to study the permeability of a network of tubes. The pore-network approach is also very useful to study the permeability of percolating porous media [50] and can be easily implemented in numerical calculations with low computational costs comparing to others numerical methods (finite element, finite volume, boundary element). If the permeability of monodisperse and ordered foam has been extensively studied, the permeability of polydisperse and disordered foam still has to be elucidated. Due to the natural polydispersity of soil, different equations for permeability can be found in the literature. For example, Hazen (1920) [44] proposed $K = C_{\text{Hazen}} D_{10}^2$ where D_{10} is the grain size for which 10% of grains (in mass) are smaller than D_{10} and C_{Hazen} is an empirical constant. This formula suggests that D_{10} is an effective grain size for the permeability. Indeed, Hazen's formula is not very accurate to predict the permeability. Formulations derived from the Carman-Kozeny [51, 17] formula give better predictions. For example, Carrier [19] proposed to use $d_c = (\sum_i x_i/d_i)^{-1}$ for the effective grain size to be used in the Carman-Kozeny formula.

In this chapter, the pore-network simulation is validated and used to study the permeability of random polydisperse foams with various membranes contents. An approximation of mean pressure field is proposed to estimate the permeability of the fully open-cell foam, i.e., containing no closed membranes. The effect of small pores in polydisperse foams is studied and the effective pore size is proposed to estimate the permeability of a polydisperse foam through a monodisperse one. To complement, the effect of closed membrane proportion is investigated in order to provide a permeability prediction of a polydisperse foam with random open membrane proportion through the fully open-cell foam.

IV.2 Pore-network model for permeability

IV.2.1 Pore-network model for monodisperse foams

Recently, pore-network was proposed for permeability of monodisperse foams having thin and partially closed membranes [58]. In this model, the fluid flow in foam is governed by the pressure drops that occur when the fluid flows through the membrane aperture. In the case of circular aperture, the pressure drops are described by a local flow conductance established by Sampson [88]:

$$q^{(i)} = G_{fl}^{(i)} \Delta P^{(i)}, \quad \text{with} \quad G_{fl}^{(i)} = \frac{r_{o,i}^3}{3\eta}, \tag{IV.1}$$

where $q^{(i)}$, $\Delta P^{(i)}$ are the local volume fluid flow rate passing through the membrane aperture i of radius $r_{o,i}$ and the local pressure drop, respectively. $G_{fl}^{(i)}$ is the local conductance and η is the dynamic viscosity of the fluid. The pore-network model describes the foam pore-space as a network of fluid flow conductances. A steady flow of an incompressible fluid is considered. Consequently, the sum of current flowing towards or away from to the pore i is equal to zero (similarly to Kirchhoff's junction rule): $\sum_{j=1}^{Nv_i} G_{fl}^{(ij)}(P_i - P_j) = 0$ where P_j is the pressure of pore j being in the neighborhood of pore i which has Nv_i neighbors. A macroscopic pressure gradient is imposed by imposing a pressure difference between top and bottom pores. When the pores are connected from top to bottom, the pressure in each inner pore can be calculated from the following matrix form equation:

$$[G][P] = [F], \tag{IV.2}$$

here, $[P]$ is a vector containing the pressure of inner pores. $[G]$ is a matrix of local conductances: $-\sum_{j=1}^{Nv_i} G_{fl}^{(ij)}$ on the diagonal and $G_{fl}^{(ij)}$ elsewhere. $[F]$ is a vector containing zeros except for inner pores having top pores or bottom pores as neighbors where $F_i = \sum G_{fl}^{(ij)}(P_i - P_j)$ in which P_j is the pressure of top or bottom pores. From the knowledge of pores pressures, the permeability K is calculated from the flow of fluid Q passing through a cross-section A of foam:

$$K = \eta \frac{Q}{A} \frac{1}{\lambda}, \tag{IV.3}$$

where $\lambda = \frac{\Delta P}{H}$ with ΔP is the macroscopic pressure gradient applying on foam sample of thickness H. The flow rate Q is equal to the sum of the flow rates passing through N_{WA} open membranes which cover the section A (see Fig. IV.1):

$$Q = \sum_{i=1}^{N_{WA}} q^{(i)} = \sum_{i=1}^{N_{WA}} G_{fl}^{(i)} \Delta P^{(i)}. \tag{IV.4}$$

Note that this pore-network model with Sampson's law has been successfully validated by comparing its predictions to FEM calculations on Kelvin structure and used for monodisperse foam having thin open membranes [58, 59, 78].

IV.2.2 Validation of Sampson's law for polydisperse foams

In this section, we want to check the validity of Sampson's law as well as pore-network method for the application on polydisperse foam by considering a simple structure of foam: two cylindrical pores of different sizes R_1 and R_2 are connected by thin membranes having a circle window of

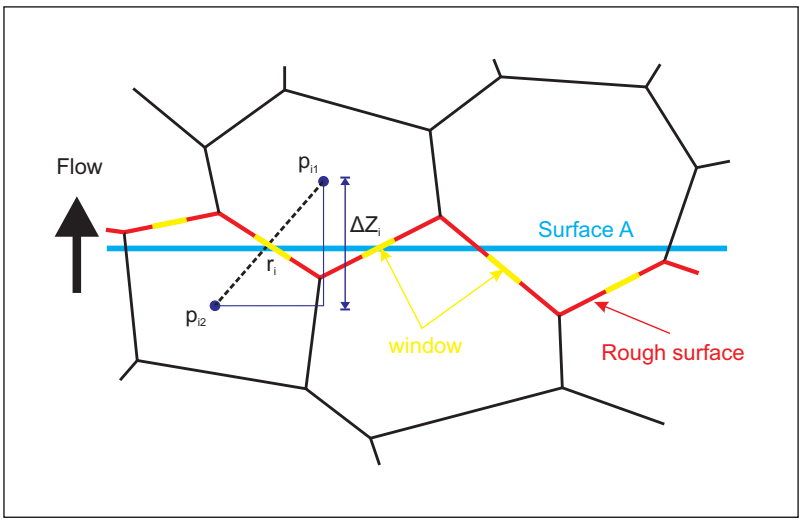

Figure IV.1: An illustration of pore-network method in 2D.

radius r_o as described in Fig. IV.2. Following Sampson's law, the fluid flow conductance is given by $G_{fl}^{\text{Sampson}} = r_o^3/3\eta$. By using FEM simulation, the fluid flow conductance is calculated:

$$G_{fl}^{\text{Compt.}} = \frac{Q}{(\Delta P/2)}, \tag{IV.5}$$

with the flow rate Q is calculated by

$$Q = \frac{\int_{\Omega_f} u_z dV}{2\,(R_1 + R_2)}, \tag{IV.6}$$

where u_z is the component of the velocity following direction of the fluid flow.

Fig. IV.3 shows the normalized fluid flow conductance $G_{fl}^{\text{Comput.}}/G_{fl}^{\text{Sampson}}$ as a function of membrane aperture sizes r_o/R_2 for various pore size ratios R_2/R_1.

It appears that as long as the membrane aperture sizes $r_o/R_2 \leq 0.6$, the effect of pore size ratio R_2/R_1 is less than 10%, and, Sampson's law can predict well the fluid flow conductance. The prediction of Sampson's law for polydisperse foams ($R_2/R_1 \ll 1$) is even better than for monodisperse foams (R_2/R_1) $\rightarrow 1$. Moreover, when the membrane aperture sizes $r_o/R_2 \rightarrow 1$, the fluid flow conductance diverges and Sampson's law cannot reproduce the FEM result (Fig. IV.3).

In fact, this configuration of two cylindrical pores can be described by an equivalent pore-network model as shown in Fig. IV.1b, consisting of 2 conductances G_{12} and G_{21} associated with the behavior of the fluid passing from pore 1 to pore 2 and from pore 2 to pore 1, respectively. Because the two membranes have the same opening size r_o, we have: $G_{12} = G_{21}$. We also could break down each conductance into 2 parts G_1 and G_2 corresponding to pore 1 and pore 2 (see Fig. IV.2c). Therefore, the local conductance can be calculated as:

$$G_{\text{local}} = G_{12} = G_{21} = \frac{G_1 G_2}{G_1 + G_2}. \tag{IV.7}$$

Considering that G_i with $i = 1, 2$ is the semi-conductance of the local conductance G_{mono} in the case of mono-pores which have size R_i. FEM results show that G_{mono} depends on the aperture size r_o/R_i, see Fig. IV.3 with $R_2/R_1 = 1$ for mono cylindrical pore or Fig. 1 in the Ref. [59] for

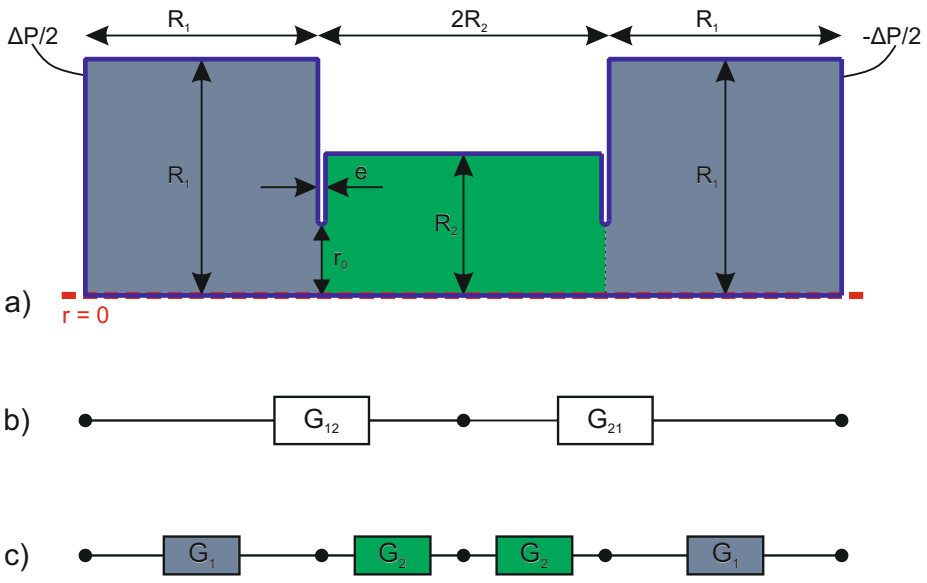

Figure IV.2: Two cylindrical pores of different sizes are connected by perforated membranes. A pressure drop is applied between the top and the bottom faces, a no-slip condition is applied over the membrane, and a slip condition is applied on the lateral faces.

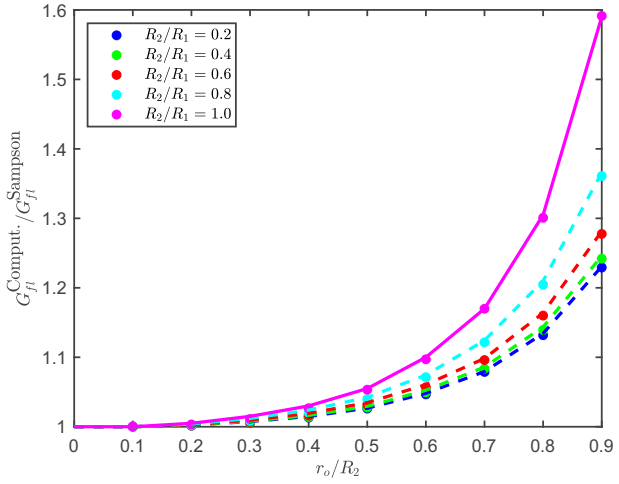

Figure IV.3: Normalized fluid flow conductance $G_{fl}^{\text{Comput.}}/G_{fl}^{\text{Sampson}}$ of two interconnected pores as a function of the membrane aperture size r_o/R_2 for various pore size ratios R_1/R_2. Comparison between FEM results (symbols) and predictions of Eq. IV.8 (dashed lines) based on FEM results of mono-size (i.e., $R_2/R_1 = 1$ with solid line).

mono cubic pore. Thus, $G_i = 2G_{\text{mono}}\left(r_o/R_i\right)$. Based on the numerical data of G_{mono} depending on r_o/R_i, the local conductance of polydisperse pore size in the considered case can be predicted:

$$G_{\text{local}} = \frac{2G_{\text{mono}}\left(r_o/R_1\right)G_{\text{mono}}\left(r_o/R_2\right)}{G_{\text{mono}}\left(r_o/R_1\right)+G_{\text{mono}}\left(r_o/R_2\right)}. \tag{IV.8}$$

As shown in Fig. IV.3, this pore-network model enables to reproduce the FEM results. In the case

of pore size polydispersity ($R_2/R_1 \ll 1$), aperture size becomes small $r_o/R_1 \to 0$ increasing the prediction of Sampson's law for the larger pore.

In the following sections, we will consider that Sampson's law is always valid and the pore-network simulation is suitable for calculating the permeability of polydisperse foams. Note that a possible improvement of the pore-network model could be possible by choosing a local conductance given by eq. IV.8 rather than by Sampson's law.

IV.3 Numerical microstructure of random polydisperse foams

Microstructures of random foams can be simulated by Neper software using the distribution of pore size and pore sphericity as inputs. Note that, here, the pore size is represented by the diameter d of a sphere having the same volume. We define the pore size variation coefficient c_d as:

$$c_d = \frac{\sigma_d}{\langle d \rangle}, \tag{IV.9}$$

where $\langle d \rangle$, σ_d are respectively the average and standard deviation of pore sizes. Similarly, the pore sphericity is determined by the average $\langle s \rangle$ and the standard deviation σ_s value or the pore sphericity variation coefficient $c_s = \sigma_s/\langle s \rangle$.

A literature review shows that monodisperse foams tend to take on an ordered structure similar to Kelvin cell [42, 76, 37]. Another ordered monodisperse structure is the Weaire-Phelan structure which can be more accurate. For these two monodisperse structures, we have $c_d = 0$, $\langle s \rangle$ around 0.91 and $c_s = 0$. These two structures differ in particular by the number of average neighbors 14 in the Kelvin structure and 13.5 in the Weaire-Phelan structure. A realistic monodisperse foam has an average neighbor number in the range of 13-14 [82, 98, 37]. Geometrical features of polydisperse foams have not been extensively studied, mostly the pore sphericity. The graphite PU foam characterized in previous chapter shows a distribution of pore sphericity of $s = 0.77 \pm 0.07$ with $c_d = 0.79$. Clearly, pore size and pore sphericity are not independent in real foams. Unfortunately, from our knowledge, no study in literature has explicitly shown their interdependence function. Therefore, in this work, the pore sphericity of polydisperse foams (mean value and standard deviation) is linearly interpolated between the pore sphericity of monodisperse foam which corresponds to $c_d \approx 0$ and $s = 0.91$ and the pore sphericity of the real graphite PU foam having $c_d = 0.79$ and $s = 0.77 \pm 0.07$. In accordance with the observation on real foams in the previous chapter, the pore size and pore sphericity are assumed to follow two lognormal distributions.

The permeability of foam depends not only on connection size (window size) but also on the network of pore connections or more precisely, on the number of windows per pore (number of neighbors). With the foam microstructures generated from Neper, the sizes of membranes and the neighbor number depend on the input distributions of pore size and pore sphericity. Therefore, sphericity is an important input parameter, and, an unsuitable choice of sphericity may lead to erroneous number of neighbors or size distribution of the membranes. For example concerning the sphericity effect, Fig. IV.4 shows the distribution of neighbor number and of faces area Fa of two monodisperse foam structures $c_d \approx 0$ with different distributions of pore sphericity: one with an experimental distribution observed in the graphite foam PU $s = 0.77 \pm 0.07$ and the other with the pore sphericity $s = 0.898 \pm 0.015$ close to that of Kelvin and Weaire-Phelan structures which has been found to be effective for the permeability of monodisperse foams.

Kelvin-like structure gives $N_v = 13.76 \pm 1.88$ in good agreement with the experimental value while the Neper microstructure calculated with the low sphericity of graphite PU foam gives $N_v = 16.26 \pm 2.70$ and fails to reproduce the experimental value. It can be shown that the low sphericity (graphite PU-like) and monodisperse microstructure create a large amount of small faces which contributes to increase the mean number of neighboring pores.

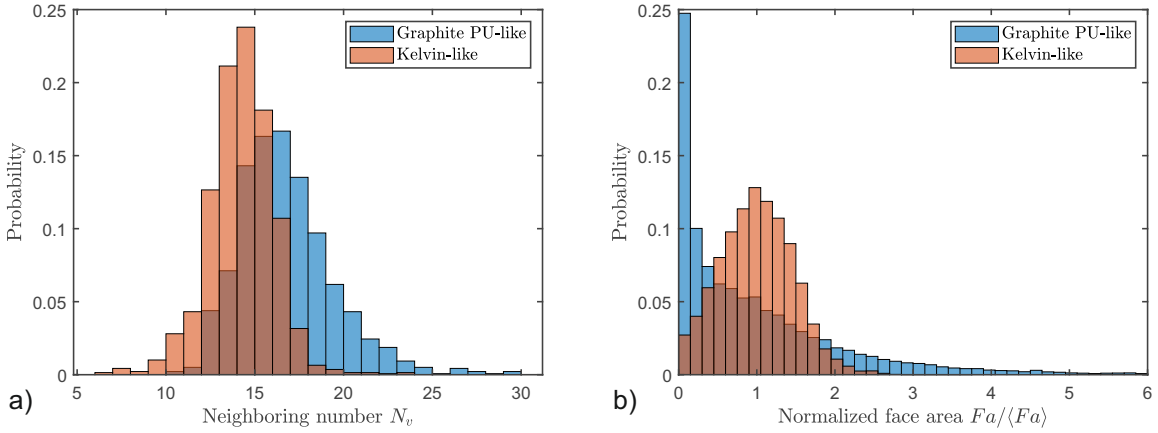

Figure IV.4: Neighboring number and face area distributions of a monodisperse foam structure with different distribution of pore sphericity. Histograms were converted into probability density functions.

The distribution of pore size and pore sphericity of Neper foam microstructures are given in Tab. IV.1 and also plotted in Fig. IV.5.

Foam	c_1	c_2	c_3	c_4	c_5	c_6
c_d	0.08	0.20	0.40	0.60	0.79	0.95
$\langle s\rangle$	0.898	0.875	0.840	0.805	0.770	0.735
σ_s	0.015	0.018	0.035	0.052	0.070	0.088

Table IV.1: Pore size variation coefficients c_d and pore sphericity $s = \langle s\rangle \pm \sigma_s$ of generated random foams.

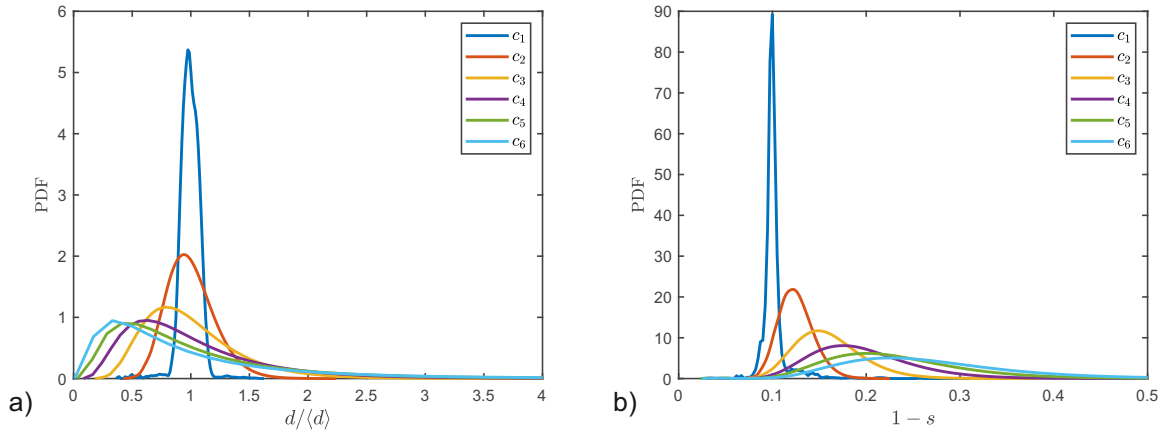

Figure IV.5: Distribution of a) Normalized pore size $d/\langle d\rangle$ and b) $1-$ Sphericity for generated random foams.

As shown in Fig. IV.6, we note that the path of evolution of pore sphericity s as a function of c_d encompasses a case observed on polycrystals for which the size distribution of the crystals is governed by the minimization of the interfacial energy as for foams [84].

The evolution of other geometrical properties with increasing c_d is shown in Fig. IV.7: The av-

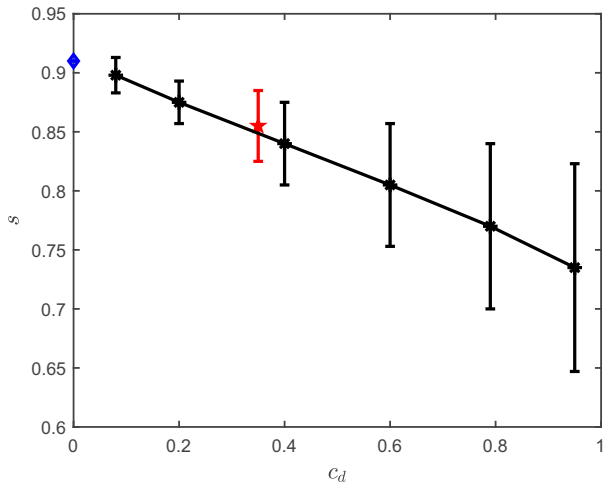

Figure IV.6: Evolution of pore sphericity s as a function of c_d in this work (in black). Sphericity of Kevin or Weaire-Phelan cell for modelisation of monodisperse foam (in blue) and sphericity of grain-growth materials reported in [92] (in red). Symbols represent mean values, error bars show standard deviation values.

erage number of neighboring pores slightly decreases while the corresponding deviation standard strongly increases. The average and the deviation standard of the membrane sizes tend to increase with c_d, polydisperse foams have more small membranes than monodisperse foam. This may be due to the increasing amount of small pores.

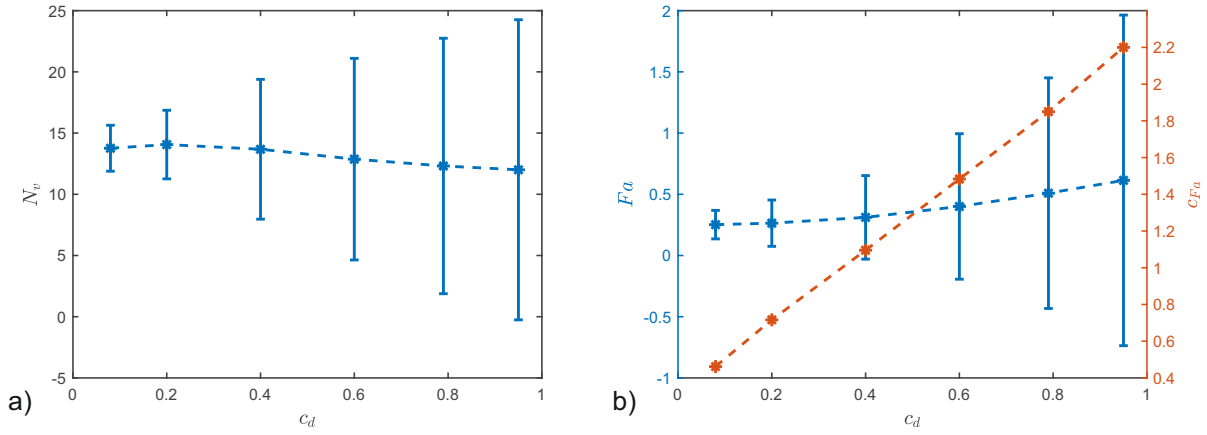

Figure IV.7: Geometrical properties: Neighbors pore number N_v, Membrane surface Fa and its variation coefficient c_{Fa} as a function of c_d. Symbols represent mean values, error bars show standard deviation values.

IV.4 RVE size for the permeability in random foams

Computations of the permeability are made on a Periodic Unit Cell (PUC) as a Representative Volume Element (RVE). A cubic box of dimension $L^{(i)}$ for iteration i plays the role of a PUC in which the pores are generated by imposing periodic conditions on both three directions. First, the distribution of pore size and pore sphericity are defined by their respective average and standard

deviation values. Among all faces, the open membrane fraction x_o and its aperture rate t_o are also imposed. Each iteration starts with a choice of cubic box size $L^{(i)}$, based on the pore size distribution and cubic box size, the pore number $N_p^{(i)}$ can be calculated through the following relation [80]:

$$\langle d \rangle = L^{(i)} \left(\frac{6}{\pi} \frac{1}{N_p^{(i)}} \right)^{1/3} \left[\int_0^\infty f_d(x) x^3 dx \right]^{-1/3}, \tag{IV.10}$$

where f_d is the probability density function of the diameters. For the lognormal distribution:

$$f_d = \frac{1}{d\sigma_p \sqrt{2\pi}} \exp\left(-\frac{\left(\ln d - \mu_p\right)^2}{2\sigma_d^2} \right), \tag{IV.11}$$

μ_p and σ_p are parameters of the lognormal distribution:

$$\sigma_p = \ln\left(c_d^2 + 1\right)^{1/2}, \tag{IV.12}$$

$$\mu_p = \ln\langle d \rangle - \tfrac{\sigma_p^2}{2}. \tag{IV.13}$$

Then, n structures are generated by Neper software (in this work $n = 5$). For each microstructure configuration (c_d, $\langle s \rangle$, σ_s), the permeability is calculated by the pore-network method following the three spatial directions and then the average over n structures is taken as the final permeability $K^{(i)}$ of iteration i. This procedure will stop at iteration i when both of two following conditions are satisfied: (i) the relative error between two consecutive iterations less than ε. (ii) pore number $N_p^{(i)} \geq 1.5 N_p^{(i-1)} \geq 50$. The latter ensures that the pore number in the generated structure is wide enough to represent the pore size distribution. The implemented algorithm is depicted in Fig. IV.8.

Fig. IV.9 shows the evolution of permeability versus the cubic box size for various polydisperse foams which have the same average pore size $\langle d \rangle$ and all membranes are opened $x_o = 1$ with the same constant aperture rate t_o . As the PUC size iteratively increases, the permeability K converges and the standard deviation vanishes. This trend is in good agreement with the work on permeability of a simple 2D random media of X. Du et al. [31]. Of course, the convergence rate to RVE depends on the acceptable error ε, however, it can be seen that the RVE size clearly increases with c_d: with a relative error $\varepsilon = 0.1$, the RVE of monodisperse foam ($c_d \approx 0$) can be reached at $\delta = L/\langle d \rangle = 3$ with 52 pores even smaller if the condition of the pore number required to represent a probability distribution, i.e., $N_p \geq 50$, is ignored, while for a polydisperse foam having $c_d = 1.0$ the RVE can only be reached at $\delta = 9$ with 231 pores.

IV.5 Permeability of polydisperse open-cell foam

In this section, we are interested in random foams with open membranes, i.e., $x_o = 1$, in order to study the effect of pore size variation c_d on the permeability.

IV.5.1 Pore-Network results

Three cases are considered: the first case is that all membranes are opened with an identical aperture size r_o ($r_{o,i} = r_o$ whatever the membrane i). The second case corresponds to all membranes having an identical aperture ratio t_o ($t_{o,i} = t_o$ whatever the membrane i where $t_{o,i} = \sqrt{Fa_{o,i}/Fa_i}$ with $Fa_{o,i}$ is the area of the membrane aperture and Fa_i is the total area of the membrane i including the aperture area) and the third case is that each membrane is opened with a random aperture

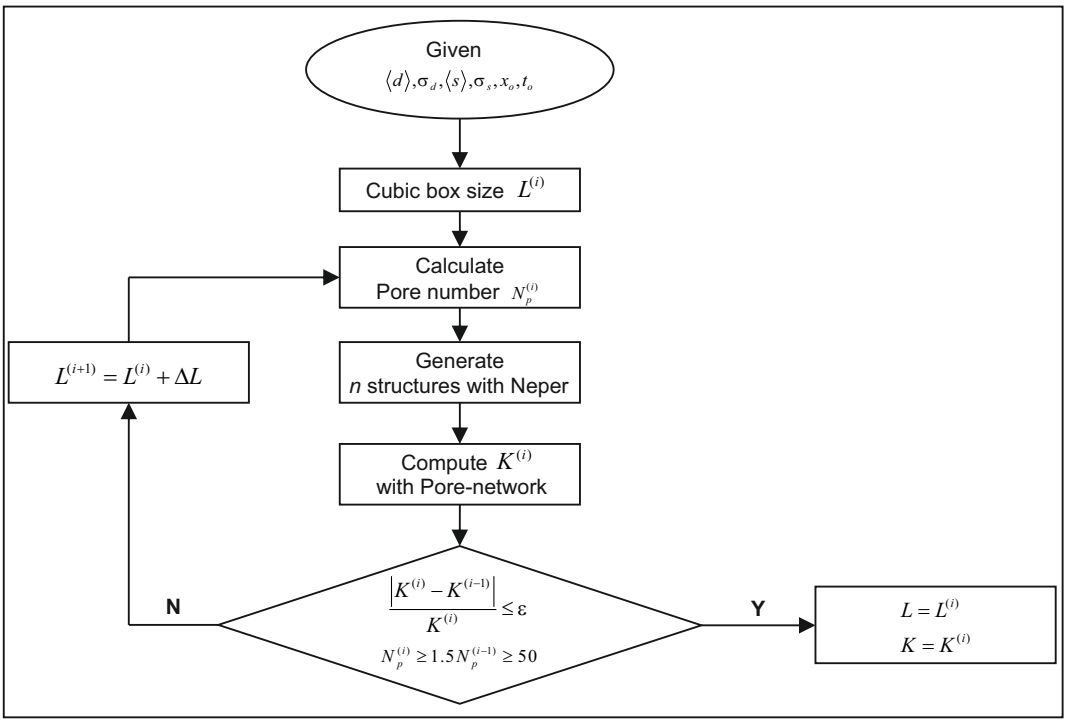

Figure IV.8: The iterative procedure for determination of RVE size.

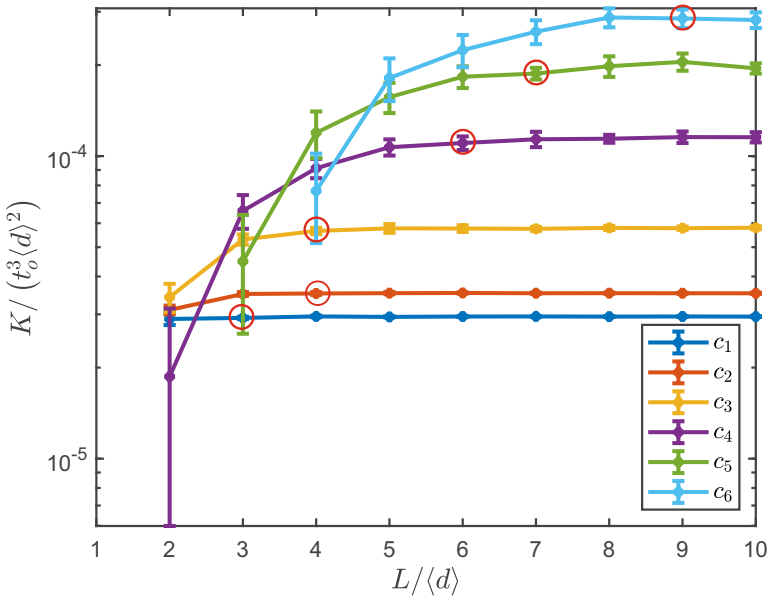

Figure IV.9: Permeability evolution versus the PUC size for various polydisperse foams. The mean permeability values are accompanied by a standard deviation corresponding to 15 realizations. Circle symbols (in red) denote the REV size corresponding to relative error $\varepsilon = 0.1$.

ratio. For the last case, a uniform law is used, the aperture ratios are chosen randomly in the interval $[0.5-\tau, 0.5+\tau]$ with τ varying between 0.01 and 0.49. The average ratio is consequently fixed $\langle t_o\rangle = 0.5$.

Fig. IV.10 shows that the permeability is quite insensitive to τ for various polydispersity degree. From a practical point of view, this result suggests that the calculation of the mean aperture ratio from experimental membranes characterization of a random foam is sufficient. Thus, thereafter, the case of random aperture ratio will not be considered.

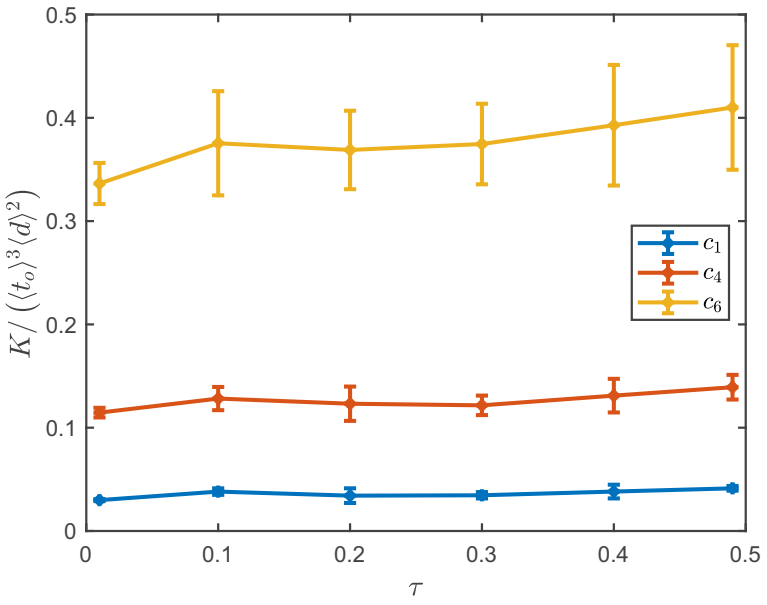

Figure IV.10: Permeability evolution versus the variation parameter of the aperture ratio. The average aperture ratio is fixed $\langle t_o\rangle = 0.5$. Symbols represent mean values, error bars show standard deviation values.

The evolution of permeability as a function of pore size variation c_d for the case of constant aperture size and constant aperture ratio is plotted in Fig. IV.11. It is quite surprising that the case of constant aperture size r_o gives a slightly decreasing trend of permeability with the polydisperse degree c_d while the permeability increases strongly for the case of constant aperture ratio t_o. With r_o constant, the effects of membranes size heterogeneity are not considered, and only the effect of the pore network structure remains. Therefore, the decreasing trend of permeability may be caused by the decreasing of the mean number of neighboring pores $\langle N_v\rangle$ (see Fig. IV.7a). A similar effect of closed membrane fraction or of N_v on permeability is observed in monodisperse foam [58]. On the contrary, for t_o constant, the aperture size is related to the membrane size. As shown in Fig. IV.7b, the mean area of membranes $\langle Fa\rangle$ slightly increases but the variation coefficient of membrane area $c_{Fa} = \sigma_{Fa}/\langle Fa\rangle$ (where σ_{Fa} is the standard deviation of membrane size) increases strongly with c_d. Also, the increase of permeability with the polydisperse degree has been found experimentally in the open-cell foams by Skibinski et al. [91]. Besides, the fact that increasing the variation coefficient of membranes size increases the permeability was also found in Westhoff et al. [104]. Of course, there is a close relationship between both effects: small pores have small membranes and consequently small apertures, and vice versa.

In the next section, the use of mean pressure field approximation to calculate the permeability of open-cell foam is investigated, and, the respective roles of pore-network structure and membrane aperture will be highlighted.

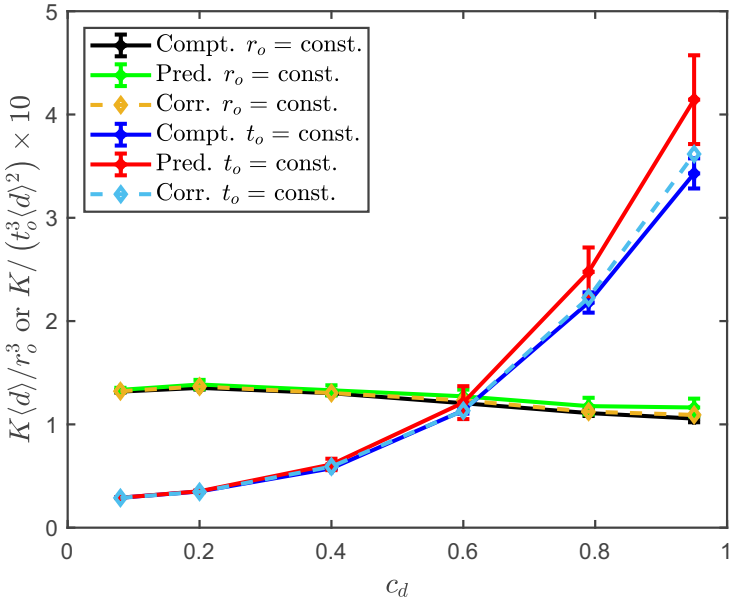

Figure IV.11: Permeability calculated by pore-network method (Compt.), predicted by Eq. IV.17 or Eq. IV.22 (Pred.) and Corrected by Eq. IV.20 (Corr.) for polydisperse foams having same aperture size r_o or same aperture rate t_o. Symbols represent mean values, error bars show standard deviation values.

IV.5.2 Mean pressure field approximation

As shown in IV.2, permeability is calculated from the total flow rate Q passing through all membrane apertures $\{i\}$ covering a foam cross-section (Eqs. IV.3 and IV.4). The flow rate passing through the membrane aperture i depends on the pressure difference ΔP_i between the pores sharing this aperture, and can be estimated from Sampson's law. Permeability is then given by:

$$K = \frac{1}{3A\lambda}\sum_{i=1}^{N_{WA}} r_{o,i}^3 \Delta P_i. \tag{IV.14}$$

Apart from Sampson's law, Eq. IV.14 has no strong assumption. Consequently, the accuracy of the permeability prediction depends on the accuracy of the pore pressure prediction. The most simple way to estimate the pore pressure is to consider the mean pressure field approximation. In this approximation, the pore pressure P_p is linearly dependent on the pore position Z_p in the direction of the macroscopic pressure gradient. Fig. IV.12 shows that the linear relationship between P_p and Z_p is satisfied on average:

$$\frac{P_p - P_{\min}}{P_{\max} - P_{\min}} \approx \frac{Z_p - Z_{\min}}{Z_{\max} - Z_{\min}}, \tag{IV.15}$$

where $P_{\max} - P_{\min} \approx \Delta P$ is the macroscopic pressure difference imposed between the top and the bottom of the sample, and $Z_{\max} - Z_{\min} \approx H$ corresponds to the thickness of the foam sample (or the spatial period in numerical simulations). For monodisperse foam (c_1), this relationship is almost perfectly satisfied while a random fluctuation around the mean trend is observed for polydisperse foam (c_6).

In terms of local pore pressure difference ΔP_i, the pressure mean-field approximation can be written $\Delta P_i = \lambda \Delta z_i$, where Δz_i is the difference between the positions of the centers of the two

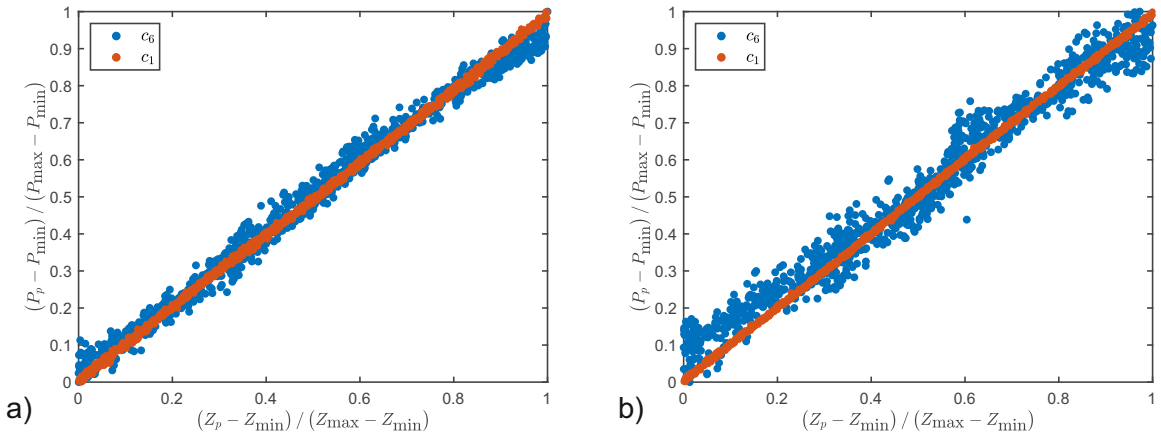

Figure IV.12: Relation between pressure in the pores P_p and their corresponding positions Z_p. a) constant aperture size, b) constant aperture ratio.

pores connected by the aperture i (measured along the direction of the macroscopic pressure gradient) and λ is the macroscopic pressure gradient. Thus, the error of the mean-field approximation can be estimated by the standard deviation of $(\Delta P_i - \Delta z_i \lambda)$:

$$\text{err} = \text{SD}\left(\frac{|\Delta P_i - \Delta z_i \lambda|}{\lambda \langle d \rangle}\right). \tag{IV.16}$$

As shown in Fig. IV.13, error clearly increases with the polydisperse degree c_d of foam. As mentioned previously, the increase of pressure prediction error in the case r_o constant must be attributed to the increase of pore-network structure disorder resulting from the increase of polydispersity degree, while in the case t_o constant, a combination of the effect of pore-network structure disorder and that of membrane-size fluctuations must be considered.

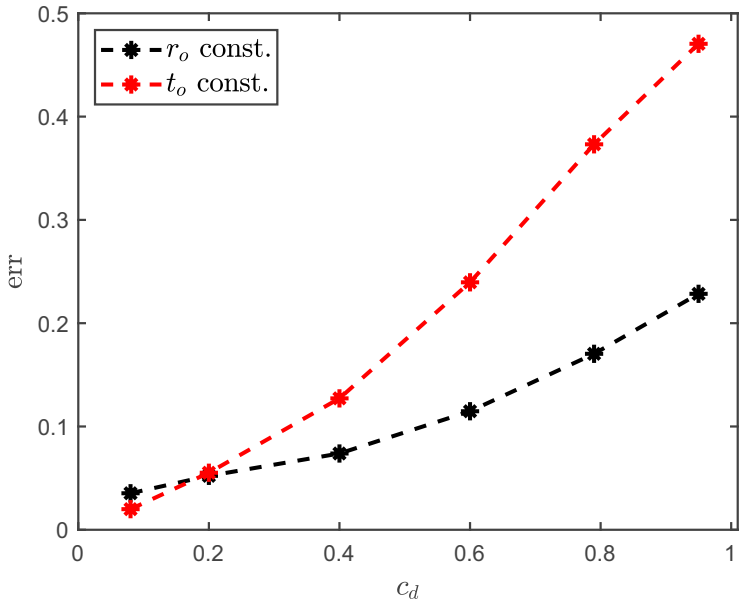

Figure IV.13: Relative error of mean pressure field approximation.

Now, we take interest in the permeability prediction with the mean field hypothesis. From the mean field hypothesis ($\Delta P_i = \Delta z_i \lambda$) and Eq. IV.14, we find:

$$K = \frac{1}{3A} \sum_{i=1}^{N_{WA}} r_{o,i}^3 \Delta z_i = \frac{N_{WA}}{3A} \langle r_{o,i}^3 \Delta z_i \rangle_{WA}, \tag{IV.17}$$

where $\langle \cdot \rangle_{WA}$ denotes the average on the membranes covering a cross-section of area A. Note that the average on all the membranes over the volume would give different results. As the probability of a large pore to be intercepted by a cross-section is higher than the one of a small pore, large pores are over-represented in surface average, leading to a lower influence of small pores.

In the case of a constant aperture size r_o for all membranes, permeability is given by:

$$K = \left\{ \frac{N_{WA}}{3A} \langle \Delta z_i \rangle_{WA} \right\} r_o^3 = \alpha_c r_o^3, \tag{IV.18}$$

where $\alpha_c = \frac{N_{WA}}{3A} \langle \Delta z_i \rangle_{WA}$ is a coefficient depending on the geometry.

In the case of a constant aperture ratio t_o, the permeability is given by:

$$K = \frac{N_{WA}}{3A} \langle r_{w,i}^3 \Delta z_i \rangle_{WA} t_o^3, \tag{IV.19}$$

where $r_{w,i} = \sqrt{Fa_i/\pi}$ is the size of the window i.

In the case of constant aperture ratio, the random variables, $r_{w,i}^3$ and Δz_i, are not fully independent (non zero covariance) as $\langle r_{w,i}^3 \Delta Z_i \rangle_{WA}$ is not equal to $\langle r_{w,i}^3 \rangle_{WA} \langle \Delta z_i \rangle_{WA}$ (as shown in Fig. IV.14). However, the increase of K when the polydispersity degree increases shown in Fig IV.11 is due to the effect of aperture sizes $\langle r_{w,i}^3 \rangle_{WA}$. Note that, for the case where the aperture ratio $t_{o,i}$ is randomly distributed and independently on the membrane size Fa_i, the permeability can be approximated by using Eq. IV.19 with $t_o = \langle t_{o,i} \rangle$.

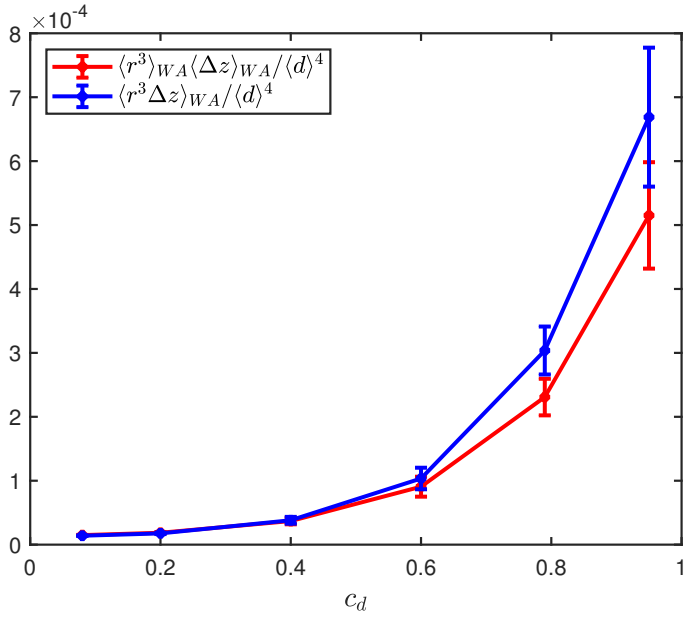

Figure IV.14: $\langle r^3 \rangle_{WA} \langle \Delta z \rangle_{WA}$ and $\langle r_i^3 \Delta Z \rangle_{WA}$ as a function of c_d with identical aperture ratio t_o. Symbols represent mean values, error bars show standard deviation values.

A comparison of permeabilities predicted by Eqs. IV.18 and IV.19 and the pore-network results is shown in Fig. IV.11. Its appears that these equations based on the pressure mean-field approximation can well predict the permeability of polydisperse open-cell foams with an acceptable error (increasing with the polydispersity degree). However, as for the pressure prediction error err, the permeability prediction is better for the case of constant aperture size than for the case of constant aperture ratio. From the calculation of the error estimator err, the mean-field approximation can be corrected to better predict the pore-network permeabilities as shown in Fig. IV.11:

$$K_{\text{Corr}} = K_{\text{MF}} \left(1 - 0.27\text{err}\right), \tag{IV.20}$$

where K_{MF} is the permeability predicted by mean-field approximation (Eq. IV.22), and the coefficient 0.27 is an adjusted coefficient.

From a practical point of view, Eq. IV.19 gives all the geometric parameters allowing an estimation of the permeability from the foam microstructure characterized by imaging methods (2D and 3D). Indeed, if the foamy material is isotropic, from analysis on two orthogonal sectional views of the foam (2D image), the parameters N_{WA}/A, $\langle r^3 \rangle_{\text{WA}}$ and $\langle \Delta z \rangle_{\text{WA}}$ can be measured. Then, Fig. IV.14 is useful for the estimation of $\langle r^3 \Delta z \rangle_{\text{WA}}$.

Before moving to the next section dedicated to the effect of small pores on permeability and to the definition of an effective pore size (two issues linked to the pore size distribution), we want to discuss about similar questions - the effect of large pores and the definition of an effective aperture size - from the point of view used in this section based on the fundamental equations of the pore-network modeling (Eq.IV.14, Sampson law, Kirchhoff nodal rule).

For both cases, r_o constant and t_o constant, we notice that the mean-field approximation predicts greater permeability values than those found with the pore-network simulations. This observation highlights the effect of large pores on the pressures of (smaller) neighboring pores in pore-network simulations while the mean-field approximation neglects this effect. Indeed, the pressure of a pore i can be described from the pressures of the neighboring pores via the conservation of mass (or Kirchhoff nodal rule):

$$P_i = \frac{\sum_{j=1}^{Nv_i} G_{ij} P_j}{\sum_{j=1}^{Nv_i} G_{ij}}. \tag{IV.21}$$

Consequently, the pressure of a pore (P_i) is a weighted average of the pressures of neighboring pores (P_j). Large pores having many neighboring pores will therefore influence many pores. This high influence of large pores leads to pull the pressure of small pores towards the pressure of large pores. Thus, the pressure difference $P_j - P_i$ between two connected pores including a large pore (and the resulting flow rate) is in average smaller than the ones predicted by the mean pressure field approximation. Indeed, this approximation does not consider any direct effect of pore-network structure.

The notion of effective membrane aperture size were introduced in effective medium approach for monodisperse foam [58]. In this approach, foam permeability is written as permeability of r_o constant foam with an appropriate choice of the aperture size r_o, corresponding to the effective aperture size r_{eff}:

$$K = \alpha_c r_{eff}^3. \tag{IV.22}$$

Within the framework of the pressure field approximation, the effective local aperture size r_{eff} for polydisperse foam is determined from Eq.IV.17:

$$r_{eff}^3 = \frac{\langle r^3 \Delta z \rangle_{WA}}{\langle \Delta z \rangle_{WA}}. \tag{IV.23}$$

For monodisperse foam, other models based on Kirkpatrick model [50] give others expressions for r_{eff} [58, 59]. In these models, the effects of aperture size fluctuation and closed membrane (percolation) on permeability are considered.

IV.5.3 Effect of small pores and effective pore size

One of the hypotheses proposed to progress in the development of a permeability model for a polydisperse foam is as follows. It is assumed that there is a network of interconnected pores of medium and large sizes that carry most of the viscous flow, so that the small pores do not contribute to the effective properties of the medium. In what follows, our aim is to identify the proportion of these small pores. To check the effect of small pores on the global permeability of open-cell foam, we consider random foams with a constant aperture ratio, the small pores having a size lower than a threshold are considered as fully closed (by closing their membranes). In order to do that, the pores must be sorted from the smallest to the largest following their sizes, and are plotted with a normalization of the cumulative pore volume $V_{\text{cum}}/V_{\text{total}}$ or of cumulative pore number $N^p_{cum}/N^p_{\text{total}}$. Then the smallest pores will be closed for the calculation of permeability K, after which we shall continue to close the larger ones.

Fig. IV.15 shows that in the polydisperse foams, the small pores are numerous but this does not represent a large volume and it makes a low contribution on the global permeability of foam. For example, in the foam having $c_d = 1.0$, 85% small pore number represent only about 10% total volume and if these 85% are closed, the foam lose only 15% of global permeability. The effect of small pore decreases with the decreasing of c_d because less polydisperse degree, more the pores having same size. It was also seen that the permeability tends to zero before all the pores are closed. This is brought about by the vanishing of percolation which occurs when the closed pores number is enough to stop the flow of fluid (the site percolation).

In order to determine whether the static permeability K of polydisperse foams can be modeled by monodisperse ones with an effective pore size, we introduce d_ϵ being the pore size related to $V_{\text{cum}}/V_{\text{total}} = \epsilon$. The determination of d_ϵ is depicted in Fig. IV.15. Moreover, we can define $D_{1-\epsilon}$ as the size of an average pore of volume equal to the mean volume of the pores having $d_i > d_\epsilon$:

$$D_{1-\epsilon} = \left(\frac{\sum_{d_i > d_\epsilon} d_i^3}{N^p_{d_i > d_\epsilon}} \right)^{1/3}. \tag{IV.24}$$

The size $D_{1-\epsilon}$ depends on both the threshold ϵ and polydisperse degree c_d except for monodisperse foams in which all pores have almost the same size where $D_{1-\epsilon}$ is a constant, i.e., the size of pores $D\left(c_d = 0\right) = \langle d \rangle = d$ (see Fig. IV.16). Thus, the permeability is expectedly predicted under the form:

$$K\left(c_d\right) = K\left(0\right) \left[\frac{D_{1-\epsilon}\left(c_d\right)}{D\left(0\right)} \right]^2. \tag{IV.25}$$

As shown in Fig.IV.17, the permeability prediction by Eq. IV.25 with the threshold $\epsilon = 0.1 - 0.15$ gives a good agreement with the computed one by pore-network simulation. This support that the permeability of a polydisperse foam can be estimated using an effective monodisperse foam with the pore size $d = D_{85-90\%}$. For the sake of a practical estimation of permeability, we consider $d = D_{90\%}$ as the effective pore size of random foam. From a practical point of view, the permeability of a monodisperse foam having a constant aperture size can be calculated easily and fast through the Kelvin-cell structure by FEM or pore-network [37, 97, 58]. Knowing the distribution of pore size, based on Eq. IV.25, the permeability of a polydisperse foam can be estimated without calculation even without generating the corresponding structure. Indeed, in

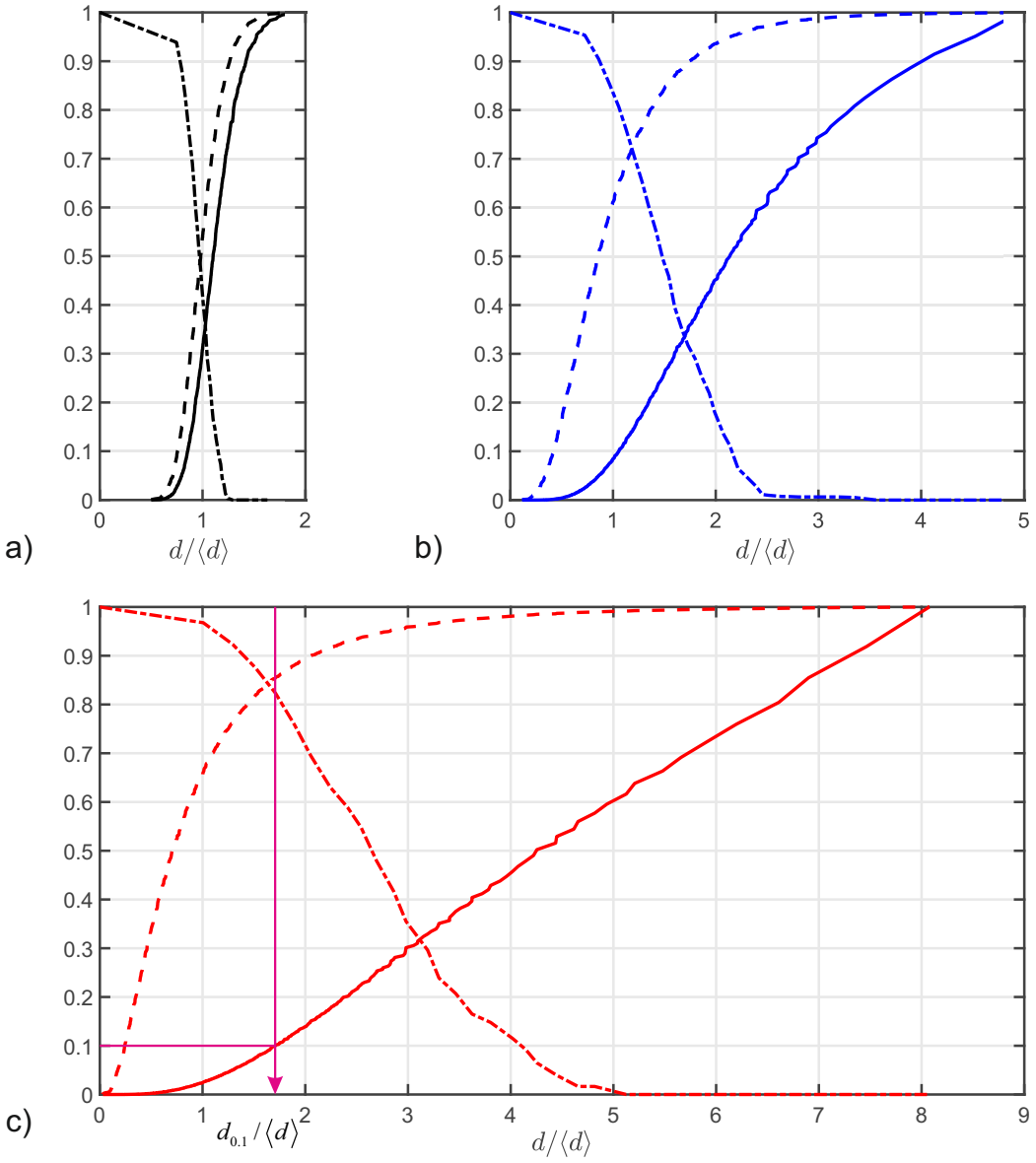

Figure IV.15: Dependence on normalized pore size $d/\langle d\rangle$ of normalized cumulative pore volume $V_{\text{cum}}/V_{\text{total}}$ (solid lines), of normalized cumulative pore number $N^p_{\text{cum}}/N^p_{\text{total}}$ (dashed lines) and of normalized permeability K/K_0 (dash-dot lines) for various coefficients of pore size: a) $c_d = 0.2$ (black color), b) $c_d = 0.6$ (blue color), c) $c_d = 1.0$ (red color). Note that K_0 is the permeability having all open membranes, K is calculated for the case of all membranes of the pore having $d_i < d$ are closed.

[59], an analytical formula was proposed to estimate the permeability of some configurations of Kelvin structure ($c_d = 0$):

$$K = \frac{\eta}{D_b}\left[n_{sq}G^{\text{sq}}_{fl} + 0.5 n_{hex}G^{\text{hex}}_{fl}\right], \tag{IV.26}$$

where D_b is the size of the unit cell which is related to the pore size d: $D_b = (\pi/3)^{(1/3)}d$. For a Kelvin structure with identical aperture ratio t_o and totally open $x_o = 1$: $n_{sq} = 2$, $n_{hex} = 4$ and

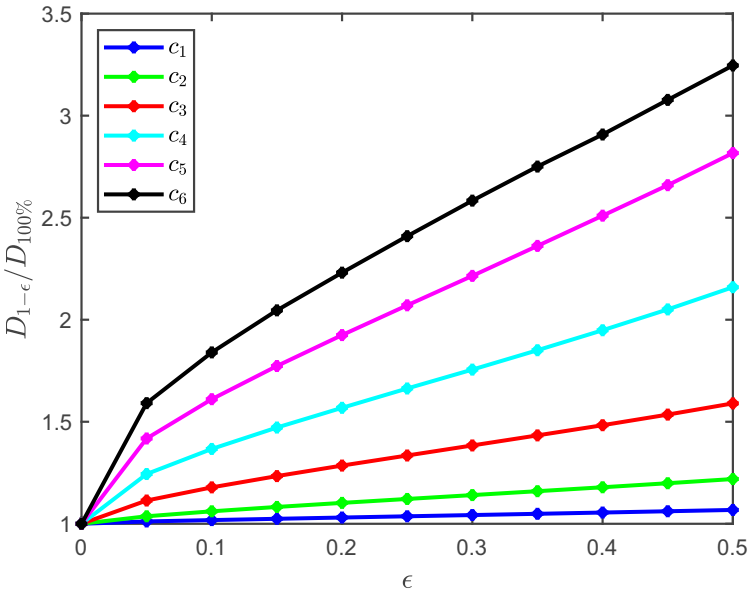

Figure IV.16: Normalized of $D_{1-\epsilon}$ as function of ϵ.

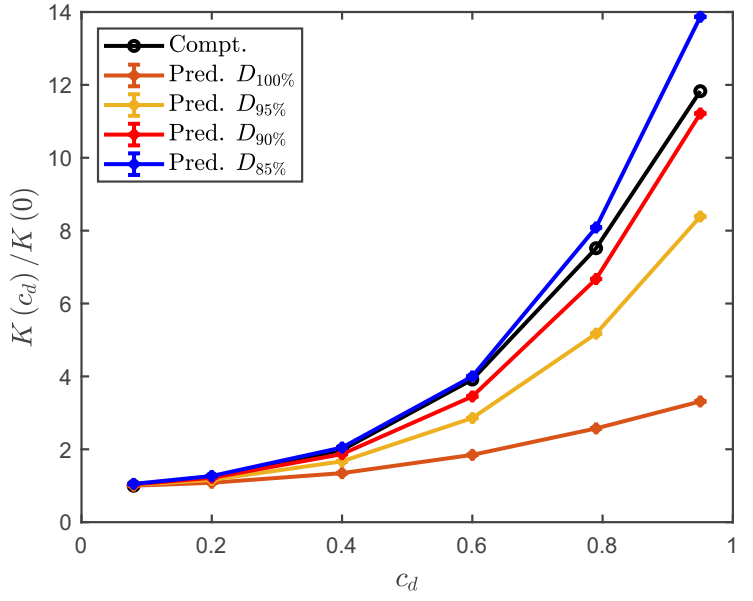

Figure IV.17: Prediction of permeability (Pred.) by Eq. IV.25 based on $D_{1-\epsilon}$ together with the computation by pore-network simulation (Compt.).

$G_{fl}^{\text{sq}} = r_{\text{sq}}^3/3\eta$, $G_{fl}^{\text{hex}} = r_{\text{hex}}^3/3\eta$ with $r_{\text{sq}} = t_o D_b/2\sqrt{2\pi}$, $r_{\text{hex}} = t_o D_b 3^{0.75}/4\sqrt{\pi}$, we have:

$$\frac{K(0)}{d^2} \approx 0.0283 t_o^3. \tag{IV.27}$$

Thus, the permeability of a polydisperse foam having identical aperture ratio t_o can be approximated by:

$$K(c_d) \approx 0.0283 D_{90\%}^2(c_d)\, t_o^3. \tag{IV.28}$$

IV.6 Effect of closed membranes

The study of the effect of closed membranes requires a large sample to represent a RVE, however, the procedure to determine the RVE size presented in section IV.4 needs the generation of several structures which requires high computing time. In this section, the calculation of permeability will be performed on foam structures having at least 1000 pores. To check if these structures are enough to represent a RVE, larger periodic foams were made from smaller ones by using a duplication process. A double period structure is a periodical duplication of the initial structure following three perpendicular directions. An example in 2D is shown in Fig. IV.18a.

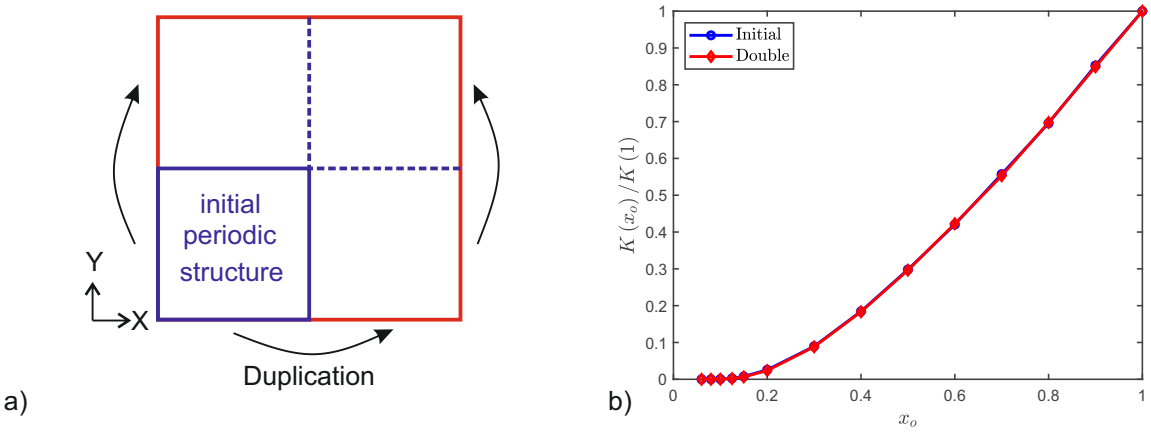

Figure IV.18: a) A simple example of a double periodic structure is made from an initial structure in 2D. b) Comparison of permeability calculated on two structures (initial and double) with $c_d = 1.0$ and identical aperture ratio for various open membrane proportion x_o.

As shown in Fig. IV.18b, for the most polydisperse foam under our study $c_d = 1.0$ which requires generally a most size of RVE, there is no significant difference between the simple period structure and the double structure. Therefore, the initial periodic structure (about 1000 pores) is enough to be a REV for the study of permeability with the change of open/closed membrane proportion.

Fig. IV.19 shows the permeabilities simulated with pore-network performed on the samples having random position of closed membranes and various open membranes proportions x_o for r_o constant and t_o constant.

In the case of r_o constant, the permeability exhibits a linear dependence on the open membranes proportion x_o except for x_o close to the bond percolation threshold x_p. While for t_o constant, the permeability depends not only on x_o but also on the polydisperse c_d. However the percolation threshold x_p seems independent from the aperture size (r_o or t_o) and the distribution of pore size c_d. Indeed, the bond percolation threshold depends on the lattice used including the neighbor pore number N_v [36]. For ordered lattices, the bond percolation threshold is close to $1.5/N_v$ [50]. This means that the average number of open membranes per pore must be greater than 1.5 to ensure the percolation. In reference to the foams, with the neighbor pore number N_v in the range $[12 - 14]$, the percolation threshold value could be found in narrow range $[0.1 - 0.125]$. It was confirmed by our numerical results.

For r_o constant, where the local conductances are identical, the curves of the dimensionless permeability $K(x_o)/K(1)$ can be superposed meaning that $K(x_o)/K(1)$ is not dependent on c_d. While for t_o constant, where the local conductances are related to the corresponding membrane areas, the values of $K(x_o)/K(1)$ are smaller than in the case of the r_o constant as observed in the

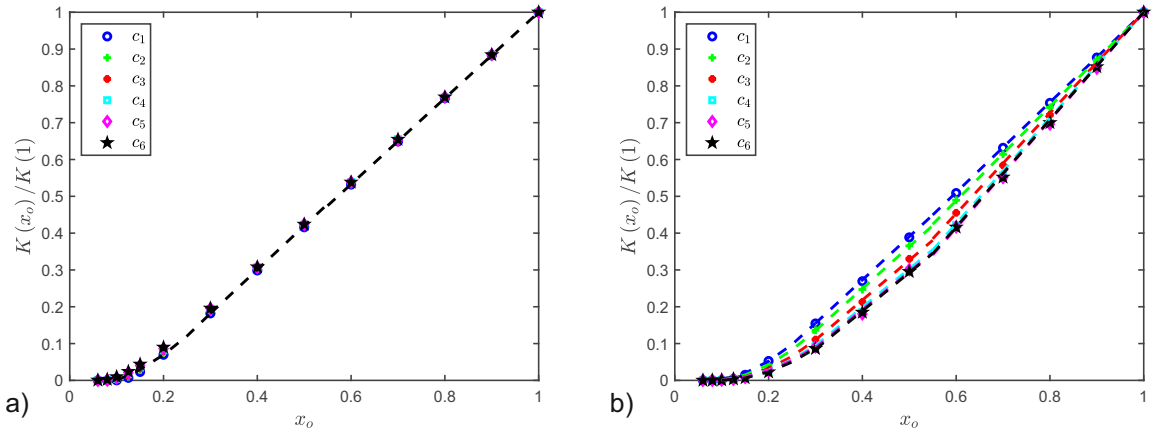

Figure IV.19: Dimensionless permeability $K(x_o)/K(1)$ as a function of open membrane proportion x_o for various polydisperse foams c_d. a) Case r_o constant b) Case t_o constant. The dashed lines correspond to adjusted curves of the form of Eq. IV.29-IV.31.

case of monodispersed foam. Evidently, the relationship between $K(x_o)/K(1)$ and x_o depends on the local conductances or the local sizes of aperture. The permeability for an open membrane proportion close to the percolation threshold can be explained by the open density R_{op} (= volume of pores within open pore space/ total volume of pores) [58].

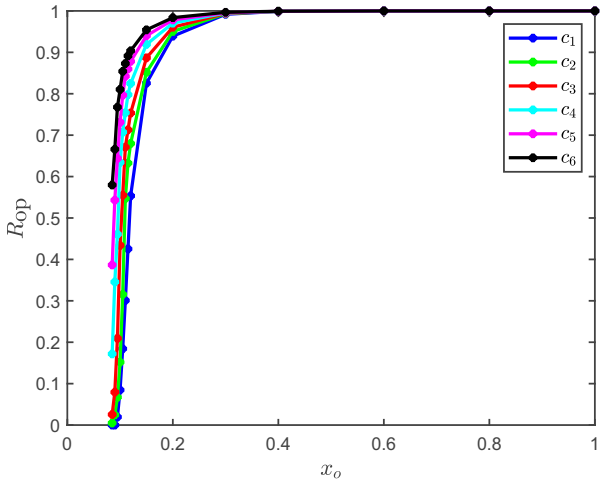

Figure IV.20: Open density R_{op} as a function open membrane proportion x_o.

As shown in Fig. IV.20 for $x_o \geq 0.3$, effect of R_{op} can be ignored. As measuring R_{op} in a real foamy material is hard and the behavior near threshold can be characterized by a power law [50], in order to provide a mathematical model for the prediction of dimensionless permeability, we assume that $K(x_o)/K(1)$ is approximated by a second-order polynomial function of x_o in the range $0.1 \leq x_o \leq 0.3$:

$$\frac{K(x_o)}{K(1)} = A_2\left(x_o^2 - 0.1^2\right) + A_1\left(x_o - 0.1\right), \tag{IV.29}$$

with assuming that at $x_o \leq 0.1$, the permeability vanishes. On the other hand, when the open membrane proportion is large, i.e. $x_o \geq 0.5$, Fig. IV.19 shows that the dimensionless permeability

increases linearly up to 1. Therefore, it is possible to estimate $K(x_o)/K(1)$ under the following form:

$$\frac{K(x_o)}{K(1)} = C_1\,(x_o - 1) + 1. \tag{IV.30}$$

For the transition range $0.3 < x_o < 0.5$, it is reasonable to define another linear approximation for dimensionless permeability:

$$\frac{K(x_o)}{K(1)} = B_1 x_o + B_0. \tag{IV.31}$$

The dependence of slopes A_2, A_1,B_1,B_0 and C_1 on the local conductances may be expressed through a dependency on variation coefficient of membranes size c_{Fa}.

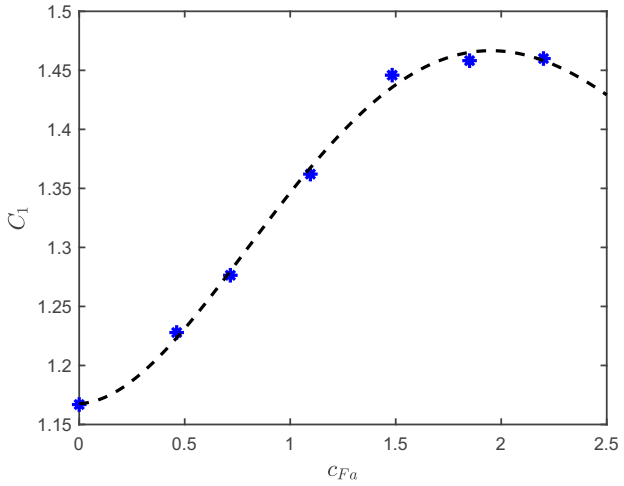

Figure IV.21: Slope C_1 as a function of c_{Fa}. Dashed line corresponds to adjusted curve of the form of Eq. IV.32.

As an example, Fig. IV.21 plotted slope C_1 as a function of c_{Fa}. Note that the case r_o constant corresponds to $c_{Fa} = 0$. Based on our numerical data, the mathematical expression of these slopes can be approximated by:

$$A_2(A_1, B_1, B_0, \text{or } C_1) \approx p_4 c_{Fa}^4 - p_3 c_{Fa}^3 + p_2 c_{Fa}^2 + p_1 c_{Fa} + p_0. \tag{IV.32}$$

The parameters p_i with $i = 1, 2, 3, 4$ for these slopes are listed in Tab. IV.2.

	p_4	p_3	p_2	p_1	p_0
A_2	0.1094	0.1567	−1.6138	1.5960	2.1317
A_1	−0.1214	0.3255	0.1242	−0.7588	0.0564
B_1	−0.0333	0.2040	−0.3643	0.1015	1.1887
B_0	−0.0057	0.0163	0.0059	−0.0553	−0.1748
C_1	0.0242	−0.1731	0.3205	−0.0071	1.1677

Table IV.2: Parameters of the polynomials of different slopes.

As shown in Fig. IV.19, the approximated formulas IV.29-IV.31 reproduce correctly the relationship between the permeability and the open membrane proportion x_o in the full range $[0.1, 1]$.

From a practical point of view, these approximated formulas allow us to predict the permeability of a polydisperse foam having a proportion of open membranes x_o if its full open-membranes' permeability is known. Note that as presented in section IV.5, the permeability of an open foam can be estimated by the mean pressure field approximation through geometrical features or by effective pore size through a monodisperse foam.

As an application on real foam, in the following, we apply the approximation above for permeability estimation of the real graphite polyurethane foam which was fabricated following a nucleation perturbation technique. The microstructures were characterized by imaging techniques: the treatment of 3D images obtained from micro-tomography X-ray given the distribution of pore size and the effective pore size $D_{90\%}$ was deduced. The membrane contents are measured through 2D SEM images including average of open membrane proportion $\langle x_o \rangle$, its average aperture ratio $\langle t_o \rangle$ and the variation coefficient of membrane area c_{Fa}. The detail of this characterization procedure was presented in chapter III.

$D_{90\%}[\mu m]$	$\langle x_o \rangle$	$\langle t_o \rangle$	c_{Fa}	$K_{\text{meas.}}[\times 10^{-10} m^2]$	$K_{\text{compt.}}[\times 10^{-10} m^2]$	$K_{\text{est.}}[\times 10^{-10} m^2]$
882	0.28	0.51	1.08	2.73 ± 0.34	2.83 ± 0.03	2.67

Table IV.3: Comparison of measured permeability, one computed by pore-network and one estimated by proposed approximation of graphite PU foam.

Since $\langle x_o \rangle < 0.3$, the permeability is estimated by combining Eqs. IV.28 and IV.29:

$$K_{\text{est.}} \approx 0.0283 \left(A_2(\langle x_o \rangle^2 - 0.1^2) + A_1(\langle x_o \rangle - 0.1) \right) D_{90\%}^2 \langle t_o \rangle^3. \tag{IV.33}$$

As shown in Tab. IV.3, the permeability calculated by pore-network simulation and the one estimated by the proposed approximation are close to the measurement value.

IV.7 Conclusion

Random polydisperse foams were generated with the increasing of pore size polydispersity to study the effect of pore size variation on the permeability. The pore-network simulation in monodisperse foams based on Sampson's law of local permeability was extended to the polydisperse foams for the calculation of permeability. The numerical results showed that the RVE size of foam media increases with the polydispersity of pore size or with the heterogeneity of microstructure and the average aperture ratio of membranes can be used as effective aperture ratio in the modeling of fully open-cell foam permeability. Based on the assumption of pressure mean field, the permeability can be estimated through the information of its microstructure [Eq. IV.22]. The small pores with small membrane were shown to contribute no significance on the permeability of polydisperse foam due to its small volume despite its large numbers in pore system. The effective pore size $D_{90\%}$ of a polydisperse foam is the average size after exclusion of small pores which contribute 10% of the total volume. Thus, it was shown that for this effective size, modeling polydisperse open-cell foam with identical aperture ratio by monodisperse one, where all pores are of the same effective size, yields mostly to statistically identical results [Eq. IV.25]. Then, effect of closed membrane proportion was investigated. By assuming the threshold percolation (critical concentration of open membrane proportion) always remains unchanged ($x_p = 0.1$) for all random foam structures and the slopes of dimensionless permeability function $K(x_o)/K(1)$ of open membrane proportion x_o depends on the variation of membrane areas, mathematical expressions were proposed to approximate this behavior in a large range of x_o ($x_o \geq 0.1$, beyond the percolation threshold) [Eqs. IV.29-IV.31]. The goal of this chapter is to provide an estimation

of the permeability of a random foam when distribution of pore size, distribution of membranes including area, proportion of open/closed and the average aperture ratio of open membranes are measured by imaging techniques presented in the previous chapter.

Chapter V

On the viscous characteristic length of thin membranes of foam samples

Contents

V.1 Introduction

As shown in chapter II, at the microscopic scale, the permeability of fluid saturated porous media can be described by the scaled dynamic Stokes problem with no-slip boundaries (Eq. II.23). In a high-frequency regime, when viscous boundary layer becomes negligible, inertial effects dominate and the fluid tends to behave as an inviscid flow having no viscous effect (except in the thin boundary layer). Therefore, at high frequency, viscous fluid flow has an analogy with the electrical conduction through a conductive fluid saturating the pore space (of a porous material having a non-conductive skeleton) which is described by the following problem:

$$\begin{aligned} \mathbf{E} &= \mathbf{e} - \nabla_y \varphi \quad \text{in} \quad \Omega_f, \\ \nabla_y \cdot \mathbf{E} &= 0 \quad \text{in} \quad \Omega_f, \\ \mathbf{E} \cdot \mathbf{n} &= 0 \quad \text{on} \quad \partial\Omega, \\ \mathbf{E} \quad \text{and} \quad \varphi \quad &\text{are} \quad \Omega\text{-periodic}. \end{aligned} \tag{V.1}$$

The high-frequency viscous tortuosity α_∞ and the viscous characteristic length Λ can be defined from local electrical field $\mathbf{E}$:

$$\Lambda = \frac{2\int_{\Omega_f} \mathbf{E}^2 dV}{\int_{\partial\Omega} \mathbf{E}^2 dS} = \frac{2I_V}{I_S}, \qquad \alpha_\infty = \frac{\langle \mathbf{E}^2 \rangle_f}{\langle \mathbf{E} \rangle_f^2}. \tag{V.2}$$

where $I_V = \int_{\Omega_f} \mathbf{E}^2 dV$ and $I_S = \int_{\partial\Omega} \mathbf{E}^2 dS$. The local electric potential φ is obtained by the Laplace problem:

$$\nabla^2 \varphi = 0 \quad \text{in} \quad \Omega_f, \tag{V.3}$$

$$\nabla\varphi \cdot \mathbf{n} = \mathbf{e} \cdot \mathbf{n} \quad \text{on} \quad \partial\Omega, \tag{V.4}$$

in which $\mathbf{e}$ is a given macroscopic electric field. By considering $\mathbf{e}$ is the unit electric field, i.e., $\|\mathbf{e}\| = 1$, as shown in [25], the tortuosity α_∞ can be rewritten as:

$$\alpha_\infty = \frac{1}{\langle \mathbf{E}^2 \rangle_f} = \frac{\Omega_f}{I_V}. \tag{V.5}$$

The electric field $\mathbf{E}$ is a function of the potential gradient $\nabla\varphi$. When the interface $\partial\Omega$ between fluid and solid phases is smooth the numerical approximation of I_S can be obtained routinely. However, when $\partial\Omega$ presents sharp edges (or corrugated geometries), φ is not smooth and the computation of $\mathbf{E}$ and Λ may be there very singular in the vicinity of singularity of $\partial\Omega$ [35]. Several studies have specifically investigated the high-frequencies' behavior of two-dimensional porous media whose internal surface has wedge-sharp geometries [1, 35, 25]. These works showed that, for the computation of I_S as well as the viscous characteristic length Λ, a particular care (such as a very dense finite element mesh around the sharp edges) is required. Recently, Zielinski et al. [110] used small smooth fillets to replace the sharp edges in order to ensure a numerical convergence of Λ. However, adding smooth fillets generates a large number of elements in the mesh and increases the computation costs. Therefore this method is suitable for simple PUC structures such as cylindrical pore (2D axisymmetric), Kelvin cell or PUCs based on packed rigid spherical beads, but not for media having a large number of pores.

Membranes in real high-porous foams have thin thickness: 1-2 μm [97, 37] even less than 0.3 μm for the graphite PU foam studied in this thesis (see chapter III). For the acoustical modeling of polydisperse and disordered foams, the use of structures having membranes with no thickness can strongly reduce the time of microstructure reconstruction and the cost of computations. However, these structures are sharp edged around the apertures connecting the pores. In this chapter, the effect of thin membrane on the local electric field will be investigated and an alternate technique for the calculation of viscous characteristic length Λ will be proposed.

V.2 Analytical solution of Laplace's equation for spheroidal pores

V.2.1 Problem description

We first consider a particular axisymmetric 3D geometry of pores for which there is a simple analytical solution of the Laplace equation allowing us to understand the effect of the presence of membranes on the volume and surface integrals, i.e., I_V and I_S. The pore geometry considered is based on the spheroidal oblate coordinates (η, ξ), defined from the rotation of confocal ellipses and hyperbolas around the axis of symmetry (Fig. V.1). These spheroidal oblate coordinates can be related to the cylindrical coordinates (r, z) as follows:

$$r = a\sqrt{1+\xi^2}\sqrt{1-\eta^2}, \tag{V.6}$$

$$z = a\xi\eta. \tag{V.7}$$

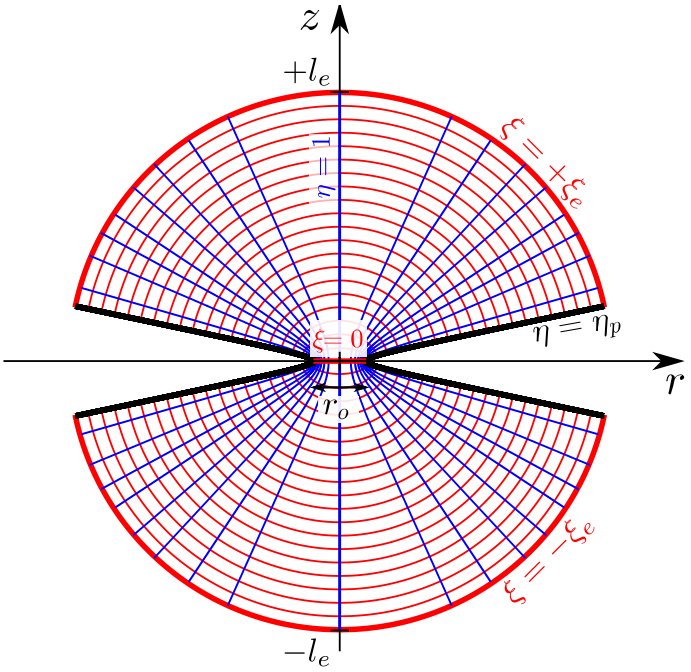

Figure V.1: Spheroidal pores.

The two foci of the ellipses are located at the coordinates $r = \pm a$ and $z = 0$. The surfaces at $\eta =$ const are associated to the hyperboloids of revolution, while the surfaces $\xi =$ const are associated to the oblate spheroids.

We will consider the following problem (Fig. V.1): a potential difference $2V_0$ is applied between two electrodes located at $\xi = \pm\xi_e = \pm l_e/a$, and the membrane corresponds to the surface $\eta = \eta_p$. The size a is chosen so that the radius of the constriction is equal to r_o: $a = r_o/\sqrt{1-\eta_p^2}$. The case of a membrane without thickness corresponds to $\eta_p = 0$. In this coordinate system, the Laplace equation is written:

$$\nabla^2 V = 0 \Leftrightarrow \frac{\partial}{\partial\xi}\left[\left(1+\xi^2\right)\frac{\partial V}{\partial\xi}\right] + \frac{\partial}{\partial\eta}\left[\left(1-\eta^2\right)\frac{\partial V}{\partial\eta}\right] = 0 \quad \text{in} \quad \Omega_f. \tag{V.8}$$

The boundary condition on the membrane surface ($\eta = \eta_p$) follows:

$$\frac{\partial V}{\partial\eta} = 0. \tag{V.9}$$

V.2.2 Analytic solution

Taking into account the boundary conditions, the solution of the Laplace equation is [85]:

$$V(\xi) = V_0 \frac{\tan^{-1}(\xi)}{\tan^{-1}(\xi_e)}. \tag{V.10}$$

Note that the scale factors of the spheroidal oblate coordinates are given by

$$h_\xi = a\sqrt{\frac{\xi^2+\eta^2}{\xi^2+1}} \quad \text{and} \quad h_\eta = a\sqrt{\frac{\xi^2+\eta^2}{\eta^2-1}}$$

. The electric field resulting from this potential is given by:

$$\mathbf{E} = -\nabla V = -\frac{1}{h_\xi}\frac{\partial V}{\partial \xi}\mathbf{u}_\xi = -\frac{V_0}{a\tan^{-1}(\xi_e)\sqrt{\left(1+\xi^2\right)\left(\xi^2+\eta^2\right)}}\mathbf{u}_\xi, \tag{V.11}$$

where $\mathbf{u}_\xi$ represents the unit vector associated with the coordinate ξ (and tangent to the hyperboloid of revolution), and, $0 \leq \xi \leq \xi_e$ and $\eta_p \leq \eta \leq 1$.

The maximum value of the electric field, $\max\|\mathbf{E}\|$, is obtained in the narrowest part of the constriction ($\xi = 0$, $\eta = \eta_p$): $\max\|\mathbf{E}\| \propto 1/\eta_p$. In the case of a membrane without thickness $\eta_p = 0$, the field has a singularity.

The volume integral, $I_V = \int_{\Omega_f} \mathbf{E}^2 dV$ with $dV = 2\pi a^3\left(\xi^2+\eta^2\right)d\xi d\eta$, is given as:

$$I_V = \int_{\Omega_f} \mathbf{E}^2 dV = 4V_0^2 \frac{\pi a\left(1-\eta_p\right)}{\tan^{-1}(\xi_e)}. \tag{V.12}$$

The electric flux I_e passing through the constriction is given by the integral of $-\mathbf{E}\cdot\mathbf{u}_\xi$ on the surface $\xi = 0$:

$$I_e = \int_{\xi=0} -\mathbf{E}\cdot\mathbf{u}_\xi dS = \frac{2\pi a V_0\left(1-\eta_p\right)}{\tan^{-1}(\xi_e)}. \tag{V.13}$$

We deduce an expression for the electrical conductance G_e due to the constriction:

$$G_e = \frac{\pi a\left(1-\eta_p\right)}{\tan^{-1}(\xi_e)}. \tag{V.14}$$

Note that Eqs. V.12 and V.14 are almost identical. This is due to the fact that the tortuosity α_∞ (and I_v, cf. Eq.V.2) depends on the electrical conductivity [14].

The integral over the pore surface $I_S = \int_{\partial\Omega} \mathbf{E}^2 dS$ with $dS = 2\pi a^2\sqrt{\left(1-\eta_p^2\right)\left(\xi^2+\eta_p^2\right)}d\xi$ is written:

$$I_S = \int_{\partial\Omega} \mathbf{E}^2 dS = \frac{2\pi V_0^2}{\left(\tan^{-1}(\xi_e)\right)^2}\tanh^{-1}\left(\frac{2\xi_e\sqrt{\left(1-\eta_p^2\right)\left(\eta_p^2+\xi_e^2\right)}}{\eta_p^2+\left(2-\eta_p^2\right)\xi_e^2}\right). \tag{V.15}$$

V.2.3 Limit for thin membrane

When the membrane thickness becomes small ($\eta_p \ll 1$), the volume integral is defined and is approximated as

$$I_V \approx \frac{4\pi V_0^2}{\tan^{-1}(\xi_e)}. \tag{V.16}$$

Note that even if the electric field **E** has a singularity as for zero-thickness membrane, I_V is always defined.

Moreover, for constrictions with a small aperture radius ($a \ll 1$ or $r_o \ll 1$) and thin membrane ($\eta_p \ll 1$), the volume integral is: $I_V \approx 8V_0^2 r_o$ and the electrical conductance is equal to: $G_e \approx 2r_o$. This expression explains the linear dependence between the inverse of the tortuosity and the size of the constriction shown in [59]: $\alpha_\infty^{-1} \propto r_o/l_e$ when $r_o/l_e \ll 1$ (here $2l_e$ represents the size of the pore). This expression for G_e could be useful for the forthcoming construction of a pore-network model for high-frequency tortuosity of the polydisperse foams (see the perspective part).

For thin membrane ($\eta_p \ll 1$) the surface integral I_S can be approximated by:

$$I_S \approx \frac{2\pi V_0^2}{\left(\tan^{-1}(\xi_e)\right)^2}\left[\ln\left(\frac{1}{\frac{1}{\xi_e^2}+1}\right) - \ln\left(\frac{\eta_p^2}{4}\right)\right]. \tag{V.17}$$

When the thickness of the membrane is zero ($\eta_p = 0$), the surface integral I_S is not defined:

$$I_S \approx \frac{2\pi V_0^2}{\left(\tan^{-1}(\xi_e)\right)^2}\lim_{\epsilon\to 0}\left[\ln\left(\frac{1}{\frac{1}{\xi_e^2}+1}\right) - \ln\left(\frac{1}{\frac{1}{\epsilon^2}+1}\right)\right] \to +\infty. \tag{V.18}$$

Note that the pore geometry considered in this section has no constant thickness membrane. However, the dimensionless parameter η_p can be related to the average thickness e_m of the membrane, and to the radius of curvature ρ_m existing at the level of the throat (narrowest zone of the constriction) as follows:

$$\rho_m = \left(\frac{d^2\rho_p}{dz^2}(0)\right)^{-1} = a\frac{\eta_p^2}{1-\eta_p^2} \approx \eta_p^2 a, \tag{V.19}$$

$$e_m = \frac{1}{\partial\Omega/2}\int_{1/2\partial\Omega} 2z dS \approx \frac{4}{3}\frac{l_e\eta_p}{\sqrt{1+\frac{1}{\xi_e^2}}}. \tag{V.20}$$

We feel that the radius of curvature is the physical parameter governing the singularity of the electrical field.

Equation V.17 expressed as a function of the radius of curvature ρ_m or of the average thickness e_m of the membrane becomes:

$$\frac{I_S}{D_p^2} \approx \frac{\pi}{2\left(\tan^{-1}(\xi_e)\right)^2}\left[\ln\left(\frac{4}{\frac{1}{\xi_e^2}+1}\right) - \ln\left(\frac{\rho_m}{a}\right)\right], \tag{V.21}$$

$$\frac{I_S}{D_p^2} \approx \frac{\pi}{\left(\tan^{-1}(\xi_e)\right)^2}\left[\ln\left(\frac{8}{3\left(\frac{1}{\xi_e^2}+1\right)}\right) - \ln\left(\frac{e_m}{l_e}\right)\right], \tag{V.22}$$

with $D_p = 2l_e$ represents the pore size. We recall that the aperture radius $r_o = a\sqrt{1-\eta_p^2}$ and $\xi_e = l_e/a$. It can be seen that $\frac{I_S}{D_p^2}$ depends linearly on the logarithm of the radius of curvature ρ_m or of the average thickness e_m of the membrane.

To conclude, through the analytic solution of Laplace's problem for spheroidal pores, we showed that the surface integral of the square of electric field I_S diverges when the membrane thickness tends to zero ($\eta_p \to 0$). For thin membrane $\eta_p \ll 1$, I_S expresses a logarithmic relation with the radius of curvature or the average thickness of membrane while the volume integral I_V is always defined. Therefore, as found in literature, the high frequency tortuosity α_∞ is always defined whatever the membrane thickness, while the viscous characteristic length is undefined for zero-thickness membrane. In the following, we will show that these conclusions are still valid for other foam structures.

V.3 Geometrical singularities in foam structures without membrane thickness

The case of no-thickness membrane was firstly considered in several works with 2D corrugated channels [25, 35] in which apex angle $\gamma = 0$, see Fig.V.2. As previously pointed, the surface integral I_S diverges in this case and consequently, the viscous characteristic length tends to zero. Therefore, the calculation of the viscous characteristic length by means of numerical methods should encounter convergence problems.

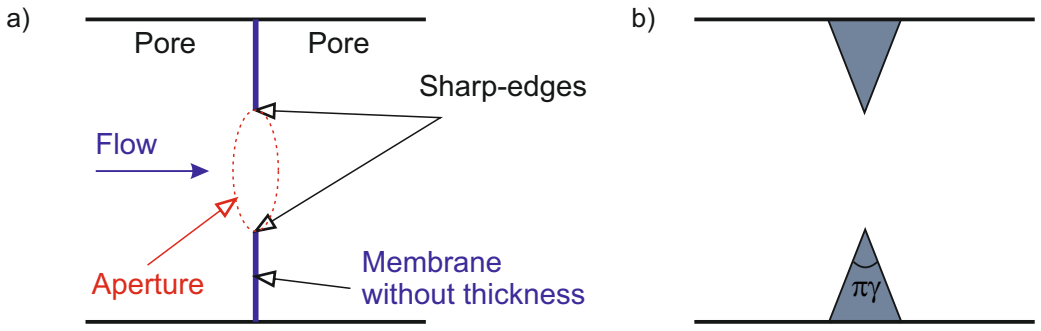

Figure V.2: a) Illustration of sharp-edges in a structure without membrane thickness. b) 2D corrugated pore channels.

To illustrate this point, we consider a 3D foam microstructure, an open-membrane configuration, called $K0$, of Kelvin cell which is widely used for the modeling of monodisperse foams. In this configuration the membranes have no thickness and are opened by a circular hole of identical radius r_0. It is true that the type of microstructure as well as the one reconstructed by the procedure described in chapter III shows sharp-edges all around the apertures connecting the pores. The Laplace equation for obtaining the tortuosity α_∞ and the viscous length Λ is resolved by FEM with the elements which are around the apertures by imposing a constant size h_e (see Fig.V.3).

As a result, Fig. V.4 shows that while α_∞ converges with the refinement of the mesh (reducing h_e), Λ tends towards zero with h_e. The convergence of I_V and divergence of I_S implies that the divergence of Λ lies in the evaluation of the surface integral I_S. These results are in good agreement with the ones performed on 2D sharp-edged porous media found in [35, 24].

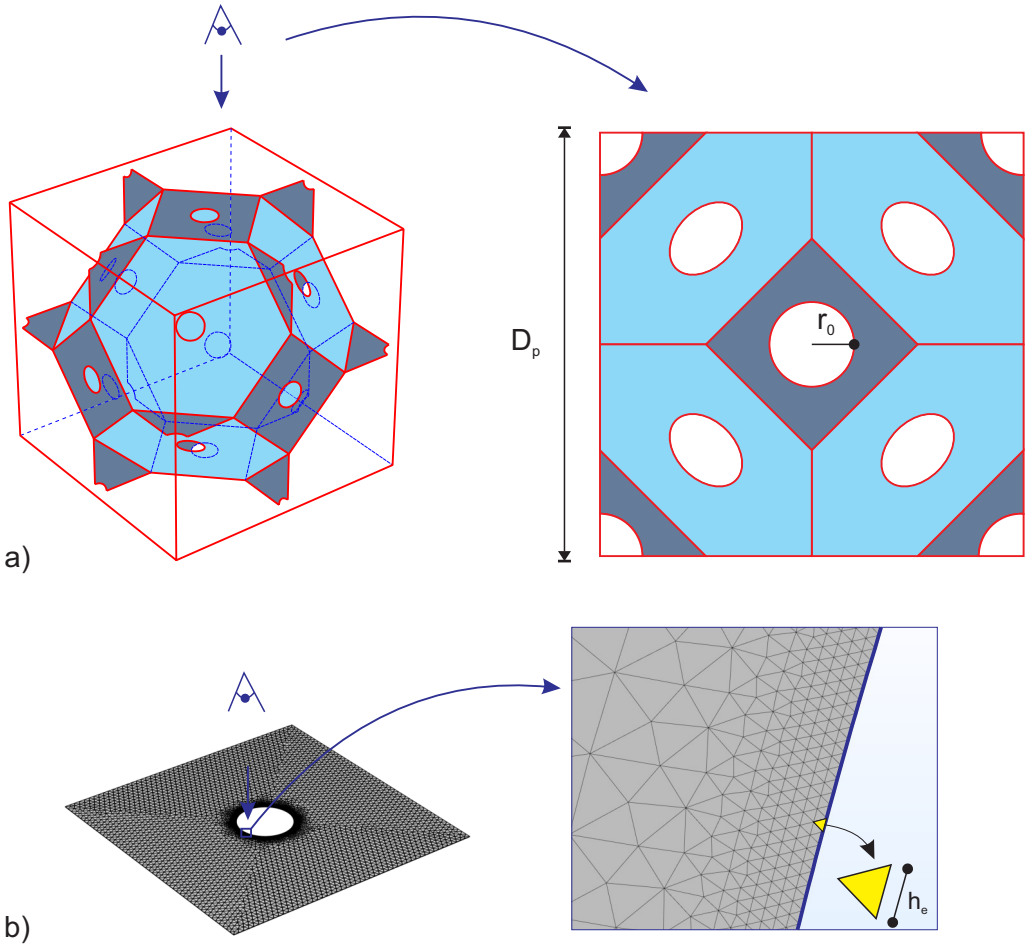

Figure V.3: a) Configuration K0 of Kelvin-cell structure. b) Finite element mesh around the aperture.

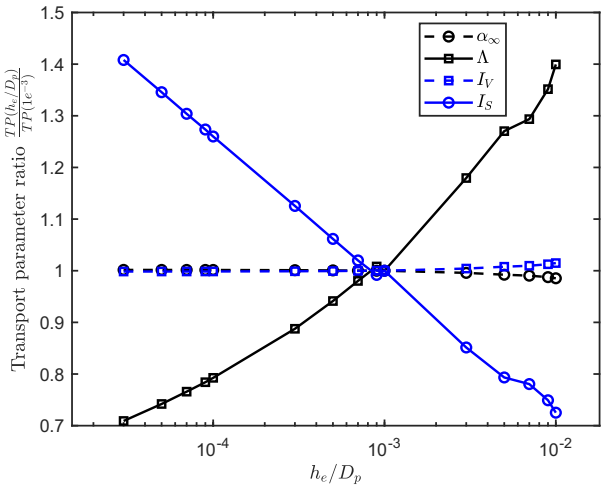

Figure V.4: Relative changes of transport parameters (TP) with respect to the ratio of h_e/D_p. $r_0/D_p = 0.1$, $D_p = 1$ mm.

V.4 Effect of membrane thickness and virtual thickness of membranes

To study the effect of membrane thickness on the surface integral I_S, three symmetrical configurations of Kelvin cell are considered as shown in Fig. V.5: $K0$, all membranes are opened; $K1$, only squared membranes are opened; $K2$, only hexagonal membranes are opened. Note that four-squared membranes which are parallel to fluid flow are ignored. Membranes have a non-zero thickness e_m. In order to avoid sharp-edged singularity geometries, a fillet of radius $e_m/2$ is added around the apertures as illustrated in Fig. V.6. That ensures a numerical convergence for viscous characteristic length Λ [110]. To ensure an accurate calculation, the element size applied along the aperture should be less than 0.1 times the thickness of membrane.

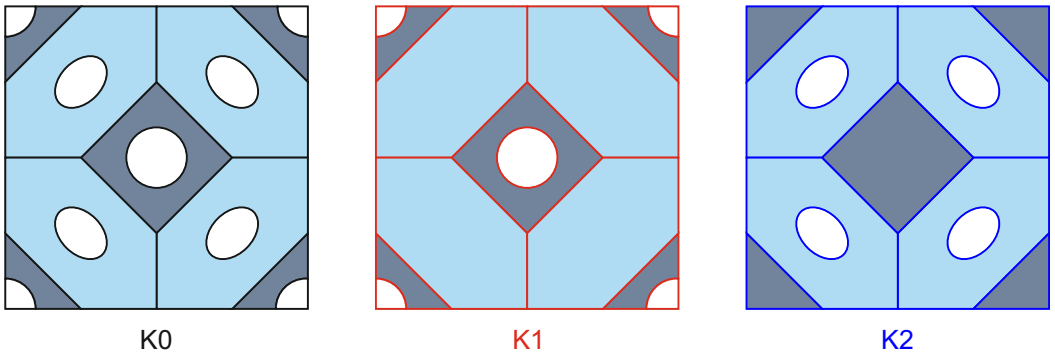

Figure V.5: Top view from the median plane of the Kelvin configurations showing the positions of closed/open membranes. Note that the horizontal median plane is a plane symmetry.

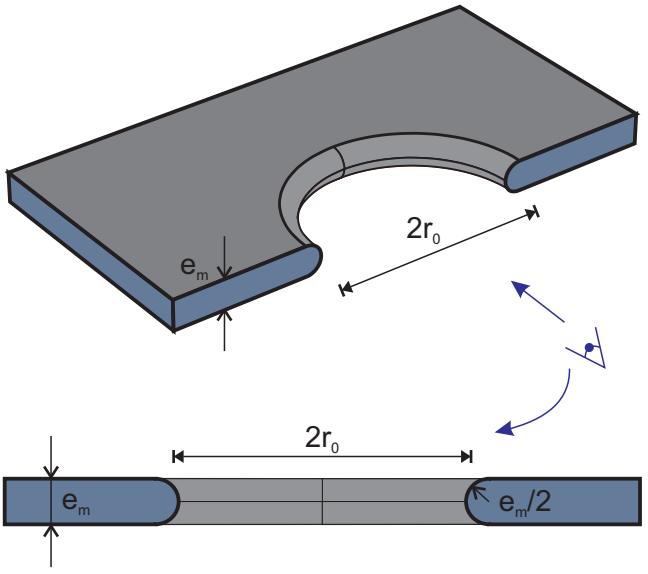

Figure V.6: Half of an open membrane with non-zero thickness e_m.

Fig. V.7 shows the surface integral I_S normalized by D_p^2 as a function of e_m/D_p. It can be seen that for thin membrane ($e_m/D_p \leq 10^{-3}$), I_S/D_p^2 depends linearly on the logarithm of the membrane thickness e_m/D_p. More specifically, there is a relation of the form $I_S/D_p^2 = A\ln\left(e_m/D_p\right) + B$ where A and B are two constants depending on the geometry. This relation is quite analogous to the analytical relation established for the spheroidal pores. By taking various

ratios of r_0/D_p (not shown here), we also obtained the same result. Note that a similar relationship between the surface integral and the mesh size was found in the FEM convergence problem shown in the previous section (V.3). Therefore, it seems possible to replace, in FEM calculations, membranes of non-zero thickness by zero-thickness membranes and by an appropriate size of the mesh elements around the membrane opening. To check this idea, we compare in Fig V.7 the FEM calculations of the surface integral performed on the two kinds of microstructure (with and without thickness).

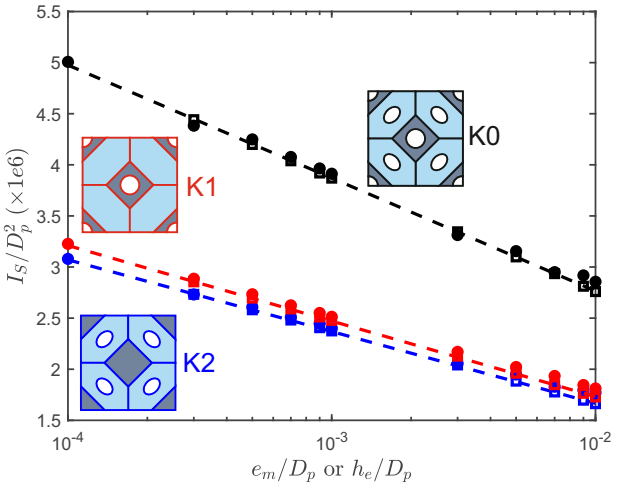

Figure V.7: Normalized surface integral I_S/D_p^2 as a function of e_m/D_p (non-zero thickness, square marker) or h_e/D_p (no thickness, circle marker) for different Kelvin-cell configurations. $r_0/D_p = 0.1$, $D_p = 1mm$. The dashed lines correspond to adjusted curves of the form $A\ln(x) + B$ with x is e_m/D_p or h_e/D_p.

The concordance between the results of these two types of microstructures is clearly observed. This supports the idea that it is possible to simulate a structure with thin membranes of non-zero thickness e_m by imposing the element size $h_e = e_m$ along the apertures of a structure with membranes having no thickness, when calculating the viscous characteristic length Λ. Alternatively, the relation $I_S/D_p^2 = A\ln\left(h_e/D_p\right) + B$ may also be used to model the thin membranes. More precisely, by considering two coarser meshes in order to determine the constants A and B of the studied microstructure, we can deduce its viscous characteristic length Λ instead of imposing a fine mesh ($h_e = e_m$).

V.5 Conclusion

We presented in this chapter, the effect of thin membranes on the evaluation of surface integral of the electrical field which causes the divergence of viscous characteristic length when numerical foam geometries have sharp edges. By working on the analytical solution of Laplace's equation for spheroidal pores and FEM simulation performed on Kelvin cell configurations, it was shown that for structures having smooth thin membranes, there is a logarithmic relationship between the surface integral $I_S = \int_{\partial\Omega} \mathbf{E}^2 dS$ and the thickness e_m of membranes. This relation combined with the equivalence between element size being applied around the apertures (in zero thickness membranes structure) and the desired membrane thickness when the calculating of I_S, gives a simple way to consider the membrane thickness effects, without modeling them in FEM simulations. As this technique significantly reduces the computational cost, it will be applied to calculate the

viscous characteristic length of polydisperse foam for which the microstructure contains a large number of membrane apertures.

Chapter VI

Acoustical properties of a real polydisperse foam

Contents

VI.1 Introduction

When a long-wavelength acoustic wave propagates in a porous medium such as foam, the energy dissipation occurs because of visco-inertial, thermal and structural effects. The sound propagation problem can be solved using an asymptotic homogenization method performed on virtual periodic structures, so-called Periodic Unit Cell (PUC), mimicking the microstructure of a real foam [76, 94, 46, 95, 97]. This approach uses semi-analytical models which require a set of transport parameters as inputs, for example, the Johnson-Champoux-Allard-Lafarge (JCAL) model [49, 20, 56] requires six transport parameters: porosity, static viscous and thermal permeability, high-frequency tortuosity, viscous and thermal characteristic lengths. The transport parameters can be computed from the steady Stokes flow and Laplace's equation related to viscous and inertial effects, respectively, and from the Poisson's equation related to heat transfer. Biot's theory [7, 8] can be used to take into account the effect of the deformations of the solid skeleton. Furthermore, the Biot-JCAL model was established from an alternative Biot's formulation for dissipative porous media with skeleton deformation, as introduced by Becot and Jaouen [6] by considering the elastic properties of the solid frame to be independent from the properties of the fluid. This model requires the six above mentioned transport parameters together with the Young's modulus, the Poisson's coefficient and the loss factor of the foam as input parameters.

A PUC can capture the essential behaviors of a foam if its microstructural features are properly identified. The Kelvin cell, e.g., a tetrakaidecahedron cell with six square faces and eight hexagonal faces that can fully fill the space and nearly minimizes the surface energy [96, 102], is widely used to study monodisperse foams including membranes effects. Based on a Kelvin structure, the fraction of fully open/fully closed membrane effects was investigated in Doutres et al. [29, 30]; the effect of membrane aperture was studied by Hoang et al.[94, 46] on both the acoustic properties and the elastic properties of foams. Recently, Gao et al. [37] and Trinh et al. [97] studied the acoustic properties of foams having both open and closed membranes. These works showed that the presence of membranes is a key parameter to control the acoustic absorption of foams and that Kelvin structure is appropriate for modeling monodisperse foams. However, the polydisperse foams which have a wide pore size distribution cannot be described by such a simple ordered structure. On the contrary, Voronoi tessellations [23] and Laguerre tessellations [60] are widely used as models for disordered foams. These tessellations are generated from a set of seeds which are often determined from a dense (overlapping or non-overlapping) packing of spheres [82, 12, 104] whose sphere size distribution is assumed as the pore size distribution of foam. Later, in the works of Redenbach et al. [82, 64, 98] the tessellation models were fitted to real foams by a minimization of the distance between morphological characteristics of the pores of the real foam and the model. This method was used to study elastic properties of closed foams with strongly varying pore sizes [81] or of open-cells foams [64]. The effects of polydisperse pore size on the permeability of open-cell foams were investigated in [104]. At the present time, however, no complete study has been carried out on acoustic properties of disordered foams by taking into account both membrane effects and wide pore size distribution effects.

The addition of graphite particles in PU foam has been shown to modify the flame retardancy, and the thermal and mechanical properties of PU foams [70, 68, 63, 21, 65]; however, their acoustic properties have not been fully studied in literature. In chapter III, the micostructures of a graphite PU foam having a wide distribution of pore size was characterized by X-ray CT microtomography and the SEM images. Its microsctructure was also reconstructed by taking into account the membrane content. Now, the acoustic properties of this foam will be investigated by applying the asymptotic homogenization method on reconstructed microstructures to derive the transport parameters and the sound absorption coefficient at normal incidence.

VI.2 Material and acoustic measurements

The graphite PU foam revealing a high porosity presents a high membrane content and a wide distribution of pore size characterized by a pore size variation coefficient equal to $c_d = 0.79$. The distributions of pore size and pore sphericity can be aproximated by two log-normal probability laws (see chapter III). The morphological properties of graphite PU foam given in Tab. VI.1 was characterized by imaging techniques. Its macroscopic properties determined from physical measurements are also summarized in Tab. VI.2.

$d\,(\mu m)$	$1-s\,(-)$	$\langle x_o \rangle\,(-)$	$\langle t_o \rangle\,(-)$
360 ± 290	0.23 ± 0.068	0.28 ± 0.05	0.51 ± 0.17

Table VI.1: Geometry properties of PU foam.

$\phi\,(-)$	$\sigma\,(Ns/m^4)$	$\rho_1\,(kg/m^3)$	$E\,(kPa)$	$\nu_e\,(-)$	$\eta_e\,(-)$
0.92 ± 0.01	67500 ± 9900	13.37 ± 0.19	172 ± 19	0.46 ± 0.02	0.157 ± 0.005

Table VI.2: Physical properties of PU foam.

The characterization of the acoustic behavior of a porous material can be obtained with a three-microphone impedance tube, as described in the Fig. VI.1. Based on this experimental setup the sound absorption coefficient at normal incidence is directly measured through the pressure created by the outgoing and the ingoing waves at the surface of the sample: $(\mathrm{SAC_{NI}}) = 1 - |p_{ref}/p_{inc}|^2$ in which, p_{ref} and p_{inc} are respectively the reflective and incident pressures at the surface of the samples. The supplementary frequency-dependent response functions of the porous material modeled as an equivalent fluid are determined from the pressure transfer functions between the microphones [87], i.e., effective density ρ_{ef} and effective bulk modulus $\mathcal{B}_{ef}$.

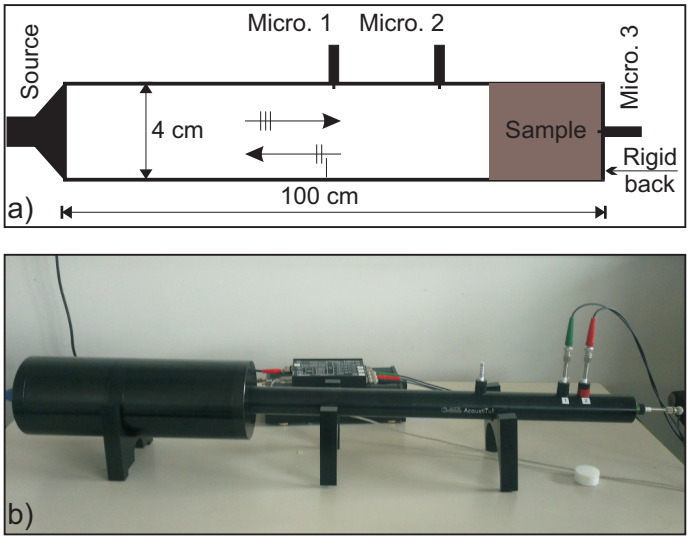

Figure VI.1: Three-microphone impedance tube. a) Schematic illustration, b) Its real picture.

Note that for the same series of six cylindrical foam samples were used to characterize the elastic, transport, and sound absorbing properties of the porous material under study, with a thickness of 21 mm (see Fig. VI.2) as described in chapter III. A thin layer of Teflon was put around

the samples in order to avoid air leakage between the tube walls and the samples; this implies that there was a slight pre-compression of the samples in radical direction. The influence of this factor will be used to justify an adjustment of the characterized elastic parameters in the model.

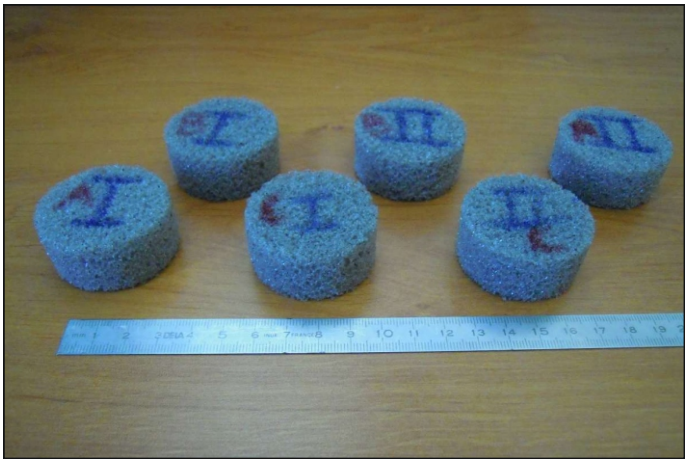

Figure VI.2: Samples used for the measurement of acoustic properties.

VI.3 Methodologies

Based on the characterized distributions of pore size and pore sphericity, the periodic microstructures of graphite PU foam were reconstructed by Neper software and validated in chapter III from a morphological point of view. These reconstructed structures will be used for the calculations of the acoustic properties which were described in chapter II.

To begin with, the foam is considered rigid, the JCAL semi-phenomenological model is used to predict the effective properties of equivalent fluid i.e., effective density ρ_{ef} and effective bulk modulus $\mathcal{B}_{ef}$:

$$\rho_{ef}(\omega) = \frac{\alpha_\infty \rho_0}{\phi}\left[1 + \frac{\phi\sigma}{i\omega\alpha_\infty\rho_0}\sqrt{1 + i\frac{4\alpha_\infty^2\eta\rho_0\omega}{\sigma^2\Lambda^2\phi^2}}\right], \tag{VI.1}$$

$$\mathcal{B}_{ef}(\omega) = \frac{\gamma P_0}{\phi}\left\{\gamma - (\gamma-1)\left[1 - i\frac{\phi\kappa}{k_0' C_p\rho_0\omega\sqrt{1 + i\frac{4k_0'^2 C_p\rho_0\omega}{\kappa\Lambda'^2\phi^2}}}\right]^{-1}\right\}^{-1}. \tag{VI.2}$$

In these equations, ρ_0, η, κ are the density, dynamic viscosity and thermal conductivity of air, respectively, P_0 ambient mean pressure, C_p the isobaric specific heat, γ the ratio of heat capacities at constant pressure and volume, i the imaginary unit, $\omega = 2\pi f$ the angular frequency. The JCAL model requires a set of six input transport parameters $\left(\phi, \Lambda', k_0, \Lambda, \alpha_\infty, k_0'\right)$. The determination of the open porosity ϕ requires an accurate experimental measurement (Chapter III), while the thermal characteristic length Λ' is directly deduced from the reconstructed geometry: $\Lambda' = 2\int_{\Omega_f} dV / \int_{\partial\Omega} dS$, here, Ω_f denotes the fluid volume and $\partial\Omega$ is the fluid-solid interface. The static airflow resistivity is directly related with the static viscous permeability, $\sigma = \eta/k_0$. The low computational cost of the pore-network simulation method, which is based on an analytical estimate of the permeability for a perforated plate [58], enables an efficient calculation of the

static permeability k_0 for the reconstructed microstructures (Chapter IV). The remaining transport parameters are computed by the finite element method using a commercial software (COMSOL Multiphysics). The high-frequency viscous tortuosity α_∞ and the viscous characteristic length Λ are given as:

$$\alpha_\infty = \frac{\langle \mathbf{E}\cdot\mathbf{E}\rangle_f}{\langle \mathbf{E}\rangle_f \cdot \langle \mathbf{E}\rangle_f}, \tag{VI.3}$$

$$\Lambda = 2\frac{\int_{\Omega_f} \mathbf{E}\cdot\mathbf{E}dV}{\int_{\partial\Omega} \mathbf{E}\cdot\mathbf{E}dS}, \tag{VI.4}$$

where $\mathbf{E}$ is the local electric field, solution of the electric conduction problem:

$$\begin{aligned} \mathbf{E} &= \mathbf{e} - \nabla_y\varphi \quad \text{in} \quad \Omega_f, \\ \nabla_y\cdot\mathbf{E} &= 0 \quad \text{in} \quad \Omega_f, \\ \mathbf{E}\cdot\mathbf{n} &= 0 \quad \text{on} \quad \partial\Omega, \\ \mathbf{E} \quad \text{and} \quad \varphi \quad &\text{are} \quad \Omega\text{-periodic}, \end{aligned} \tag{VI.5}$$

here, $\mathbf{e}$ is a given macroscopic electric field while φ is a local electric potential. Finally, the static thermal permeability k_0' is calculated as:

$$k_0' = \phi\left\langle \tilde{k}_0' \right\rangle_f, \tag{VI.6}$$

where $\tilde{k}_0'$ is the solution of the Poisson's equation:

$$\begin{aligned} -\nabla_y^2\tilde{k}_0' &= 1 \quad \text{in} \quad \Omega_f, \\ \tilde{k}_0' &= 0 \quad \text{on} \quad \partial\Omega, \\ \tilde{k}_0' \quad &\text{is} \quad \Omega\text{-periodic}. \end{aligned} \tag{VI.7}$$

For rigidly backed porous material of thickness H, the sound absorption coefficient ($\mathrm{SAC_{NI}}$) at normal incidence follows:

$$\mathrm{SAC_{NI}} = 1 - \left|\frac{Z_s - Z_0}{Z_s + Z_0}\right|^2, \quad Z_s = -iZ_{ef}/\phi\cot\left(\delta_{ef}H\right), \tag{VI.8}$$

where c_0 is the sound speed in air, $Z_0 = \rho_0 c_0$ is the the impedance of the air and Z_s is the normal incidence surface impedance. The wave number $\delta_{ef}(\omega)$ and the characteristic impedance $Z_{ef}(\omega)$ are then given by:

$$\delta_{ef}(\omega) = \omega\sqrt{\rho_{ef}(\omega)/\mathcal{B}_{ef}(\omega)}, \qquad Z_{ef}(\omega) = \sqrt{\rho_{ef}(\omega)\,\mathcal{B}_{ef}(\omega)}. \tag{VI.9}$$

Secondly, the elasto-acoustic coupling effect due to the solid phase deformation (skeleton and membranes) on the absorption coefficient is taken into account using the Biot-JCAL model [26, 6] which relies on the use of Biot's theories together with a JCAL model. The surface impedance at normal incidence in that case is predicted by [47]:

$$Z_s^{\mathrm{Biot}} = -i\frac{\left(Z_1^s Z_2^f\mu_2 - Z_2^s Z_1^f\mu_1\right)}{D_Z}, \tag{VI.10}$$

where D_Z is equal to

$$D_Z = (1-\phi+\phi\mu_2)\left[Z_1^s-(1-\phi)\,Z_1^f\mu_1\right]\tan(\delta_2 H) + (1-\phi+\phi\mu_1)\left[(1-\phi)\,Z_2^f\mu_2-Z_2^s\right]\tan(\delta_1 H), \tag{VI.11}$$

Z_k^s, Z_k^f with $k=1,2$ are the characteristic impedances in the solid (superscript s) and fluid phase (superscript f) of first (index 1) and second (index 2) Biot compressional waves:

$$Z_k^s = (P_B+Q_B\mu_k)\frac{\delta_k}{\omega} \quad \text{with} \quad k=1,2, \tag{VI.12}$$

$$Z_k^f = \left(R_B+\frac{Q_B}{\mu_k}\right)\frac{\delta_k}{\phi\omega} \quad \text{with} \quad k=1,2, \tag{VI.13}$$

δ_1, δ_2 are the complex wave numbers of the two compressional waves, and are given from:

$$\delta_k^2 = \frac{\omega^2}{2\left(P_BR_B-Q_B^2\right)}\left[P_B\tilde{\rho}_{22}+R_B\tilde{\rho}_{11}-2Q_B\tilde{\rho}_{12}\pm\sqrt{\Delta}\right] \quad \text{with} \quad k=1,2, \tag{VI.14}$$

where

$$\Delta = \left[P_B\tilde{\rho}_{22}+R_B\tilde{\rho}_{11}-2Q_B\tilde{\rho}_{12}\right]^2-4\left(P_BR_B-Q_B^2\right)\left(\tilde{\rho}_{11}\tilde{\rho}_{22}-\tilde{\rho}_{12}^2\right), \tag{VI.15}$$

μ_1, μ_2 are the ratio of the velocity of the air over the velocity of the solid phase for the two compressional waves:

$$\mu_k = \frac{P_B\delta_k^2-\omega^2\tilde{\rho}_{11}}{\omega^2\tilde{\rho}_{12}-Q_B\delta_k^2} \quad \text{with} \quad k=1,2. \tag{VI.16}$$

In these equations, P_B , Q_B and R_B are the elasticity coefficients,

$$P_B = \tfrac{4}{3}N+B_b+\tfrac{(1-\phi)^2}{\phi}B_f, \tag{VI.17}$$

$$Q_B = B_f(1-\phi), \tag{VI.18}$$

$$R_B = \phi B_f, \tag{VI.19}$$

where $B_f=\phi\mathcal{B}_{ef}$ is the bulk modulus of the fluid in the pore space, the bulk modulus of the solid frame B_b can be evaluated by the following equation:

$$B_b = \frac{2N(\nu_e+1)}{3(1-2\nu_e)}. \tag{VI.20}$$

The shear modulus of the material N is estimated by

$$N = \frac{E(1+i\eta_e)}{2(1+2\nu_e)}. \tag{VI.21}$$

Biot's modified mass densities are expressed as [26, 6]:

$$\tilde{\rho}_{22} = \phi^2\rho_{ef}, \tag{VI.22}$$

$$\tilde{\rho}_{12} = \phi\rho_0-\tilde{\rho}_{22}, \tag{VI.23}$$

$$\tilde{\rho}_{11} = \rho_1-\tilde{\rho}_{12}. \tag{VI.24}$$

The representative periodic geometries without membrane thickness reconstructed by the procedure described in chapter III have sharp edges all around the windows connecting the pores.

These sharp edges lead to a value of the viscous length Λ which converges very slowly to zero [35]. As shown in chapter V, the thickness e_m of thin membranes can be simulated by the associated size h_e of elements applied along the apertures; and there exists a logarithmic relationship between the surface integral I_S of the square of the electric field and the size of the element h_e on the apertures: $I_S = A \ln h_e + B$. By using two coarser meshes with $h_e^{(1)}$ and $h_e^{(2)}$, the geometry-dependent coefficients, A and B, are calculated from:

$$I_S^{(1)} = A \ln h_e^{(1)} + B, \tag{VI.25}$$

$$I_S^{(2)} = A \ln h_e^{(2)} + B. \tag{VI.26}$$

The viscous characteristic is then deduced as

$$\Lambda = \frac{2I_V}{I_S}, \tag{VI.27}$$

where I_V is the integral of the electric field over fluid domain $I_V = \int_{\Omega_f} \mathbf{E}^2 dV$ and $I_S = A \ln e_m + B$. In this work, the thickness of membranes e_m is assumed equal to 0.001 times the averaged pore size $\langle d \rangle$, as observed through SEM images.

Due to local heterogeneity, for each size of the reconstructed domain, the calculation is performed on fifteen different configurations (five generated structures, together with three configurations of randomly selected open membranes) along the x, y, and z axis perpendicular to the cubic unit cell boundaries. Fig. VI.3 shows a configuration of periodic geometry, with 453 pores; and the corresponding mesh.

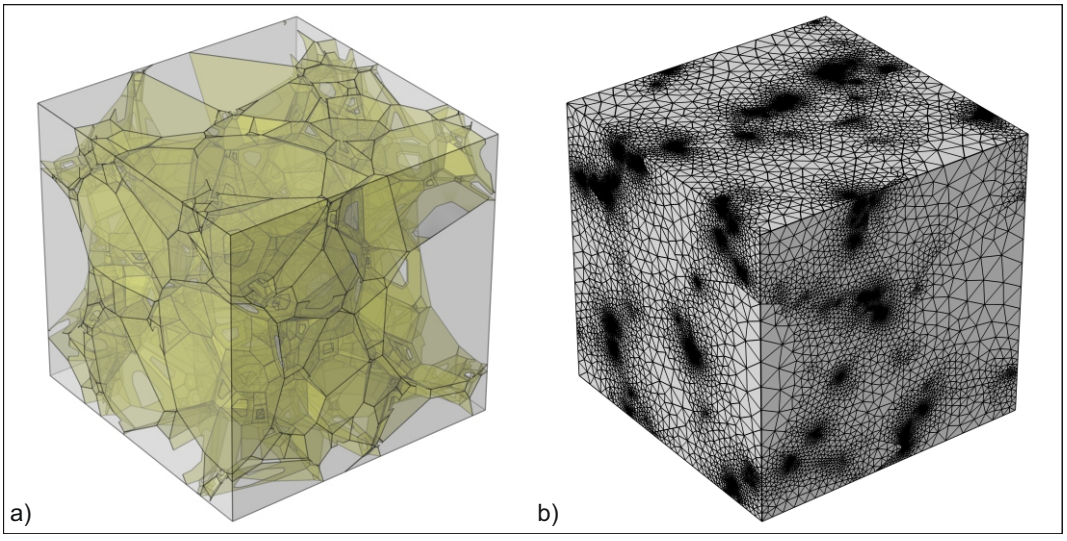

Figure VI.3: A configuration of periodic geometry of 453 pores a) and corresponding mesh b).

VI.4 Results and discussions

VI.4.1 Macroscopic transport parameters

In this section, we show how the transport properties depend on the size of the structure or more specifically, on the pore number $\left(N_p\right)$ in the structure. The transport parameters are computed separately on the generated structures by using the method described in section VI.3. The minimum number of pores must be greater than 50 in order to ensure representativity of the pore size

distribution. As expected, Fig VI.4 shows that the transport parameters tend to converge with N_p. However, all the parameters do not converge with the same rate when increasing the number of pores: the rate of convergence of Λ, Λ' and k_0' with N_p is higher than the rate of convergence of (k_0) and (α_∞) with N_p. At $N_p = 453$ which corresponds to $L/\langle d\rangle = 10$, the RVE size is considered to be reached for all of transport parameters.

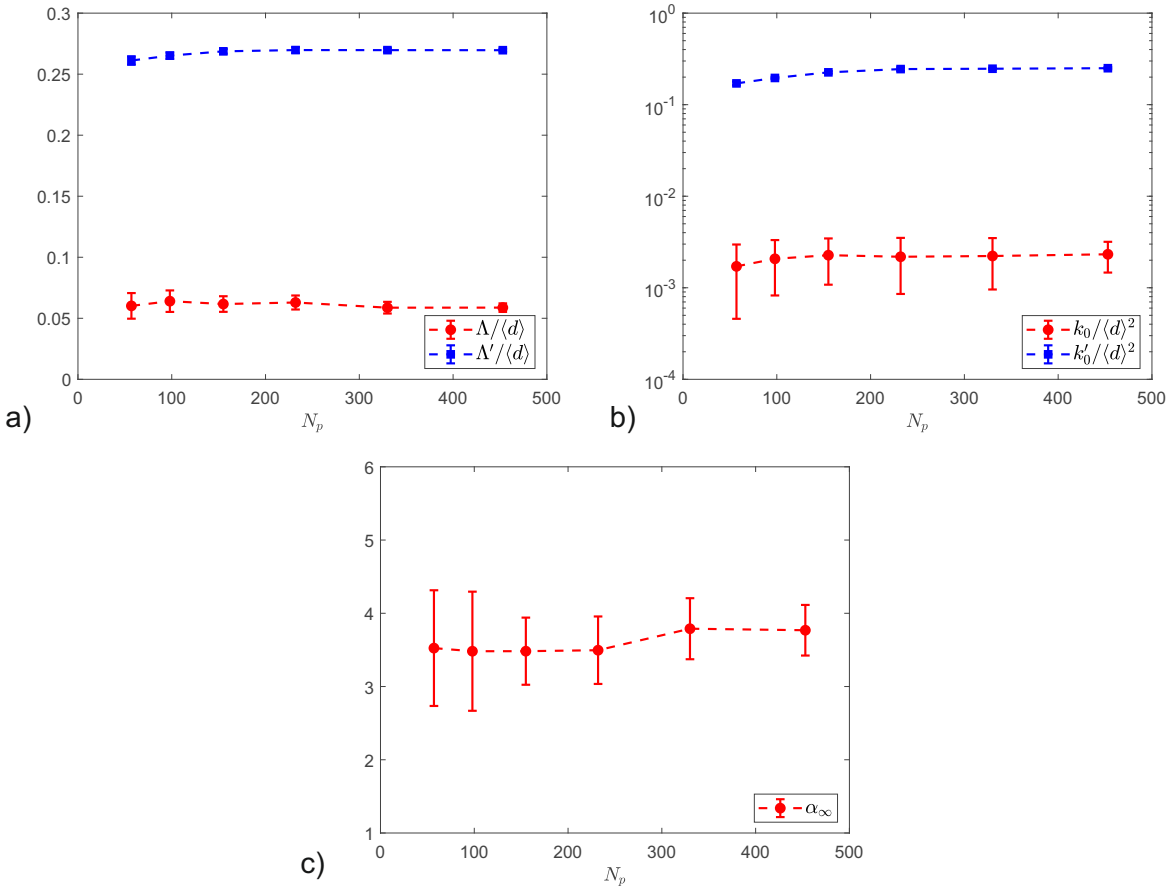

Figure VI.4: Dimensionless transport properties versus pore number N_p. The error bars represent the standard deviations.

In Table VI.3, the computed and measured macroscopic parameters are presented. The large associated standard deviations correspond to a strong anisotropy of the transport properties mainly for k_0 and α_∞, which is induced by the pore size and shape inhomogeneity. On average, for the several simulated microstructures, the computed values are in close agreement with the measured value of viscous permeability k_0. For this PU foam having a significant fraction of closed windows, the strong effect of membranes presence is expressed by high tortuosity and high value of characteristic lengths ratio $\Lambda'/\Lambda = 4.56$ [29].

	$\phi\,(-)$	$k_0\,(10^{-10}m^2)$	$\alpha_\infty\,(-)$	$\Lambda\,(\mu m)$	$\Lambda'\,(\mu m)$	$k_0'\,(10^{-10}m^2)$
Measurements	0.92 ± 0.01	2.73 ± 0.34				
Computations		2.83 ± 0.03	3.77 ± 0.35	59 ± 3	270 ± 1	324 ± 8

Table VI.3: Macroscopic transport parameters: measurements and computational results

VI.4.2 Sound absorption coefficient prediction

Concerning the SAC prediction, Fig. VI.5 shows the comparison of measured absorption coefficients and that simulated with the parameters computed above. The measured data are represented by the dispersion envelope obtained on all the used samples. The simulations of the SAC at normal incidence are displayed for the mean values of the calculated transport parameters using the Johnson Champoux-Allard-Lafarge (JCAL) model. In order to take into account the skeleton deformation effect, two simulations were also carried out with the Biot-JCAL model: the first with the average value of the characterized elastic parameters and the second by adjusting the Young's modulus.

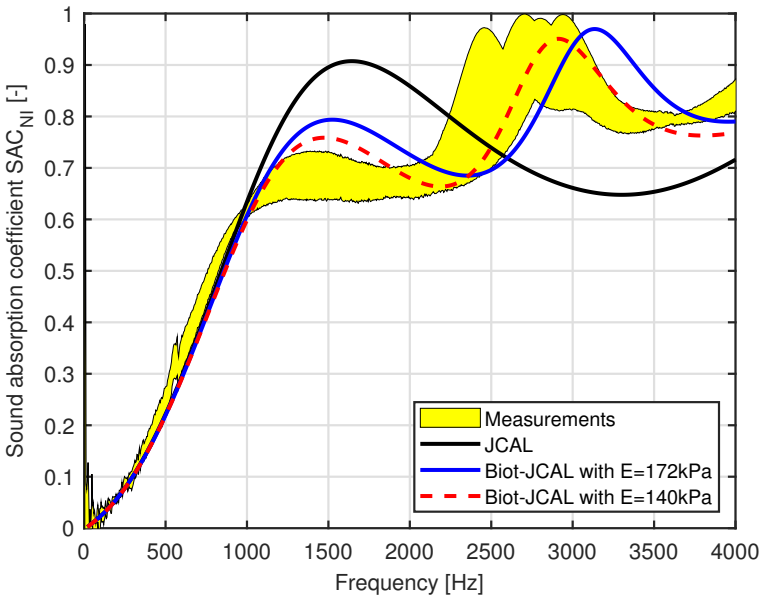

Figure VI.5: Sound absorption coefficient. Sample thickness: 21 mm.

Fig. VI.5 demonstrates that there is a strong poro-elastic coupling between 800 Hz and 4 kHz. Indeed, to quantify the elasto-acoustic coupling, Pilon et al. [77] developed the Frame Acoustical Excitability (FAE) criterion which takes into account the specific stiffness of the frame, the visco-inertial coupling between the two phases and the size, or shape factor, of the sample. Our foam exhibits a high FAE criterion, FAE $\approx$ 57 MW/Kg, which supports the idea of a strong elasto-acoustic coupling. This value has to be compared with the proposed critical criterion, stating that when FAE $>$ 2 MW/Kg, the elastic foam may become notably sensitive to the edge constraint. The JCAL model obviously cannot describe this phenomenon. Therefore, the Biot-JCAL is more suitable but we can note a difference between the measurements (yellow filled zone) and the simulation carried out with the average values of the elastic parameters (blue line). This deviation can be justified by the fact that the quasi-static compression method has a strong dependence on compression while the measurements with impedance tube lead to a small pre-compression. Fig. VI.6 shows the intrinsic Young's modulus measured as function of the compression rate. It can be seen that decreasing the used compression rate leads to the obtention of a lower Young's modulus. We note that at a compression rate around 0.5 %, the value of the characterized Young's modulus is consistent with the one used to simulate an acoustical behavior of the foam (Fig. VI.5) in good agreement with experimental data (E = 140 kPa). Note that, 0.5 is the compression rate in the quasi-static compression experiments in which the samples tend to expand in the radial direction; but it is not exactly the same value in the impedance tube measurements, because the samples are

limited radially by the tube.

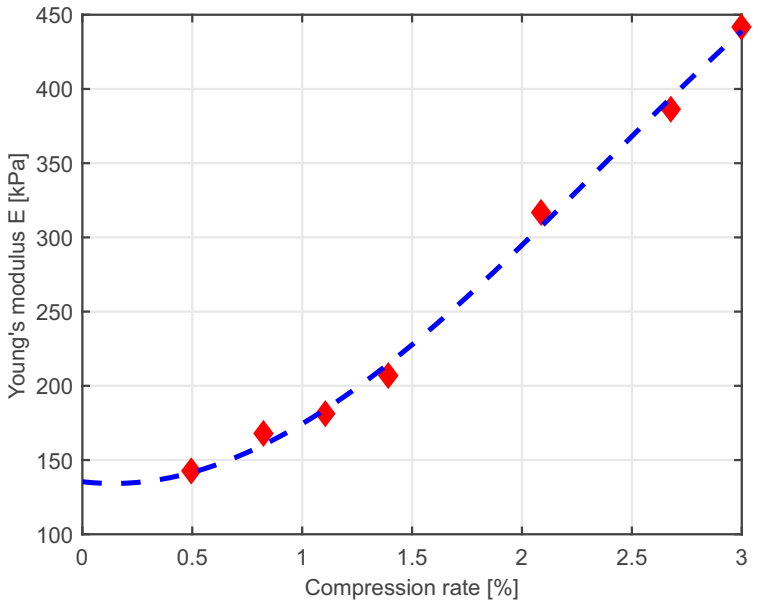

Figure VI.6: Intrinsic Young's modulus as a function of the compression rate for a sample 40 mm in diameter.

Moreover, Fig. VI.7 shows the sound absorption coefficient curves for different values of the Young's modulus. It can be observed that reducing the Young's modulus makes it possible to better describe the elastic coupling effect. However, one can see that the model does not work perfectly whatever the value of Young's modulus. It can be explained by the fact that our model considers a perfect bond between the sample and the impervious rigid wall, which is not the case. Our measurements show a high sensitivity to the mounting conditions of the sample in the tube (see appendix A). Moreover, in terms of elastic parameter characterization of porous materials, F. Chevillotte et al. [22] showed that the obtained results depend on the initial load (stress or deformation) suggesting that the elastic parameters should be characterized following the final application of materials.

In order to evaluate the contribution of viscous and thermal dissipation on the SAC curve, based on Biot-JCAL model with adjusted Young's modulus ($E = 140$ kPa), it is possible to define the Biot-J model which does not take into account the thermal effects by modifying the effective bulk modulus in Eq. VI.2:

$$\mathcal{B}_{ef}(\omega) = \frac{\gamma P_0}{\phi}. \tag{VI.28}$$

In the same way, the Biot-CAL model is defined with discarding the viscous effects while keeping the effective bulk modulus in Eq. VI.2 but modifying the effective density in Eq. VI.1

$$\rho_{ef}(\omega) = \frac{\alpha_\infty \rho_0}{\phi}. \tag{VI.29}$$

Fig. VI.8 compares the computed sound absorption coefficient curves with Biot-JCAL, Biot-J and Biot-CAL together with the measured one. It can be shown that the Biot-CAL which does not take into account the viscous effect is not convincing. In addition, small deviations between Biot-JCAL and Biot-J show the importance of viscous and elastic effect. We therefore conclude that for foams

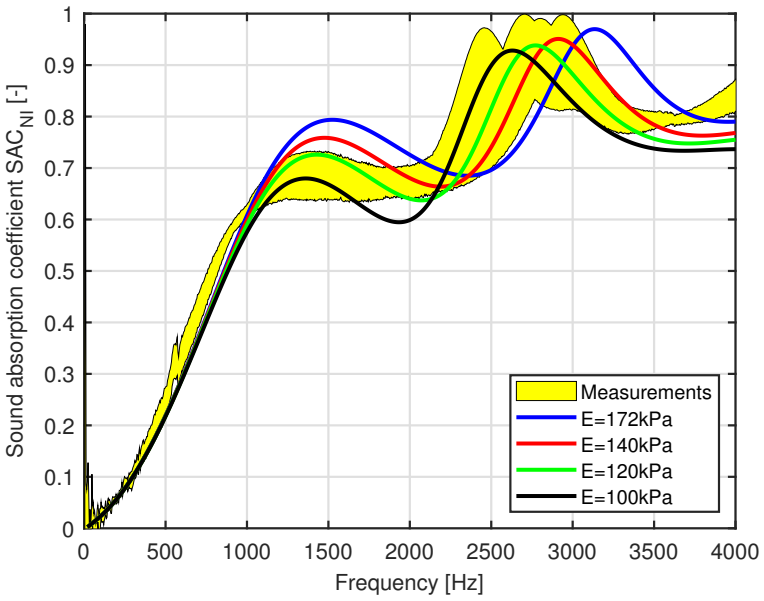

Figure VI.7: Sound absorption coefficient for various Young's modulus (Biot-JCAL model). Sample thickness: 21 mm.

having a large amount of membranes, the absorption is mainly controlled by the viscous flow and the elastic skeleton effects; whereas the thermal losses do not play a significant role on the sound absorption for this kind of foams.

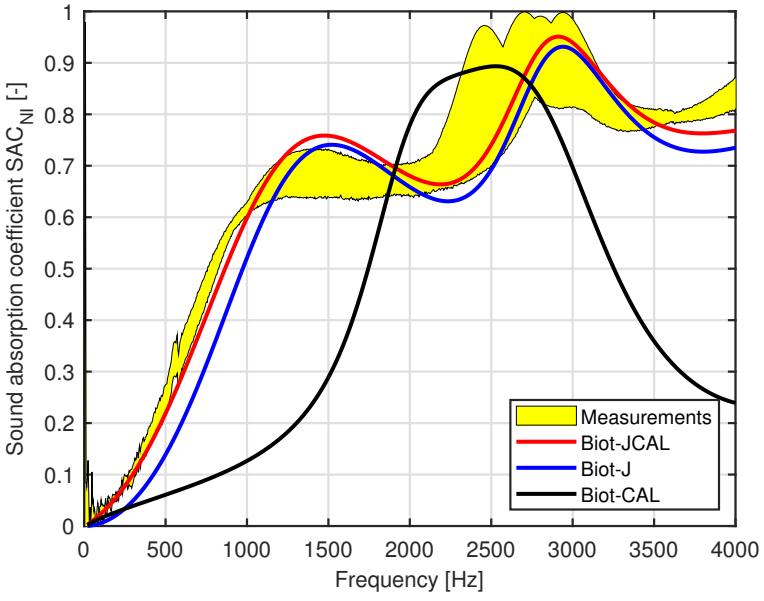

Figure VI.8: Characterized and computed sound acoustical coefficient ($E = 140$ kPa). Sample thickness: 21 mm.

VI.4.3 Effect of membrane content

The membranes can influence the elastic properties [46, 38] through the thickness and opening size. However, this effect decreases when reducing the membrane thickness, and it could be negligible for foams having membranes thickness such that $e_m/\langle d\rangle \approx 0.001$. In Fig. VI.9, we plot the variation of the asymptotic parameters as a function of the membranes aperture rate $\tau_o = x_o t_o$. The associated sound absorption coefficients are given in Fig. VI.10. It shows evidently that increasing τ_o reduces membrane content, which leads to an increase of the static viscous permeability k_0 and reduction of the tortuosity α_∞. Also worth to be mentioned, the pore-volume-to-surface ratio increases with τ_o, thus Λ and Λ' increase with τ_o. The static thermal permeability k_0' slowly increases with τ_o because k_0' is not directly related to connectivity of the pore space [90]. This tendency is in agreement with the one found in the works on monodisperse foams [94, 97]. Roughly speaking, increasing t_o and x_o gives a similar trend for the studied transport parameters and corresponds to an increase of the sound absorbing coefficient (in the studied range of variation). However, it appears necessary to take into account the exact values of both the proportion of open windows x_o and the membrane aperture ratio t_o to get an accurate estimation of macroscopic parameters and sound absorption coefficients.

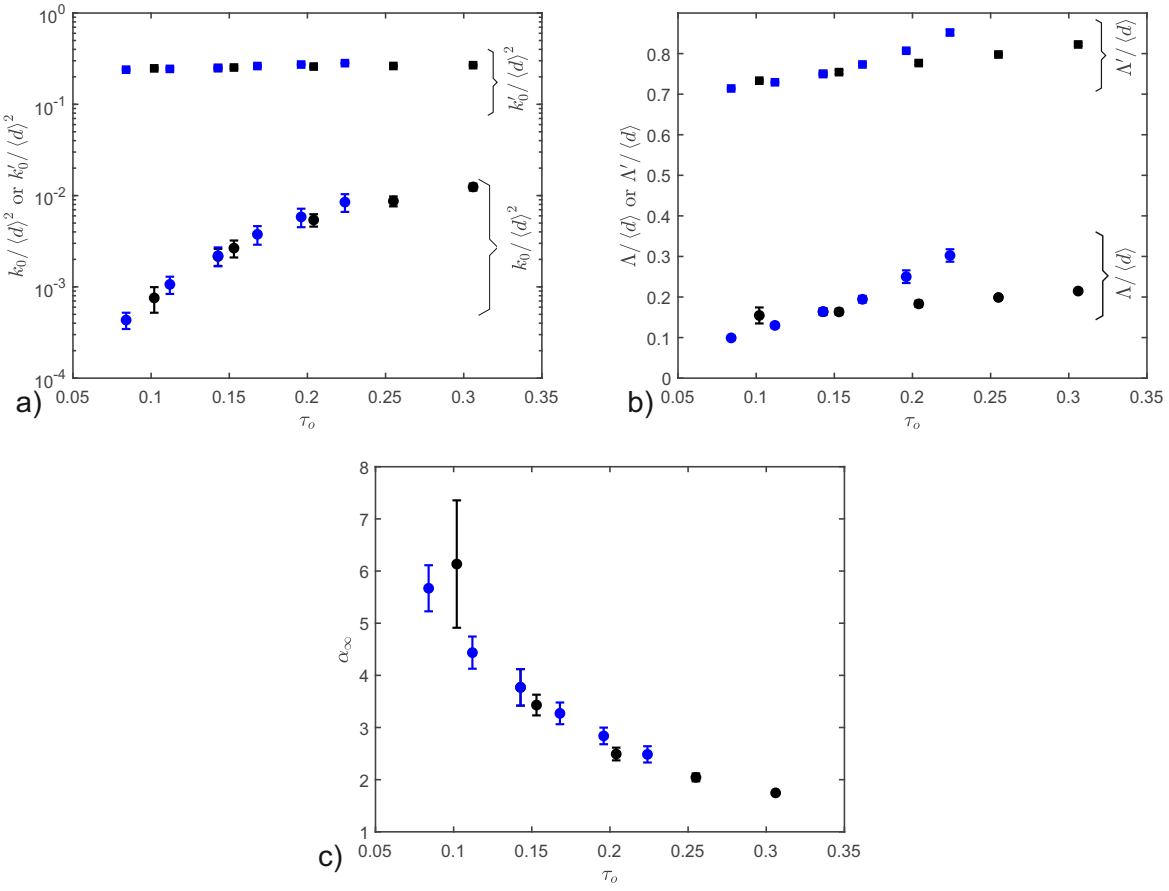

Figure VI.9: The membrane aperture rate τ_o dependence of the transport parameters. The black symbols correspond to the case of $t_o = 0.51$, the blue symbols correspond to the case of $x_o = 0.28$. The error bars correspond to standard deviations.

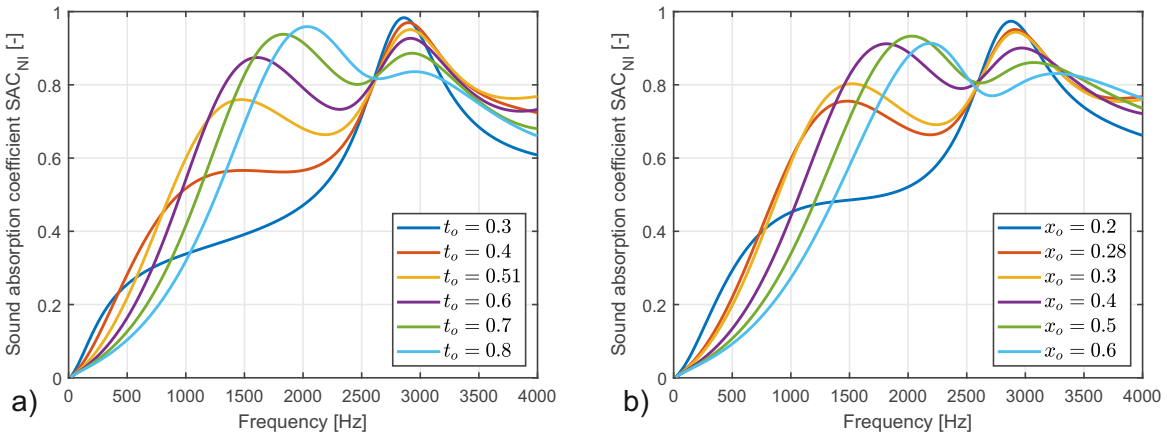

Figure VI.10: Sound absorption coefficients of the foams with different membrane aperture ratios (a), with different opened membrane fraction (b). Sample thickness: 21 mm.

VI.5 Conclusion

This chapter studied the acoustic properties of a graphite PU foam. The foam presented a wide distribution of pore size and a high fraction of fully-closed membranes. Its microstructure was studied by advanced image analysis techniques and reconstructed using an advanced Laguerre tessellation technique by the Neper software. The heterogeneity and anisotropy of foam pores were both taken into account by means of the fitted distributions of pore sizes and pore sphericity used as input parameters. The fraction of open membranes, as well as the average aperture ratio of open membranes, were also included in the three dimensional stochastic model.

A numerical homogenization approach was applied to the modeled microstructures in order to determine the corresponding transport parameters. Based on the evolution of transport parameters with simulated pore numbers, an estimate of the size of the RVE was provided, from which the sound absorption coefficient at normal incidence was derived using the semi-phenomenological JCAL or Biot-JCAL model in order to take into account the effect of solid skeleton deformation. This model was assessed by comparing experimental measurements and simulations. The results showed that the classical JCAL model cannot be used to predict accurately the sound absorbing coefficient because of a strong poro-elastic coupling. The sound absorption coefficient predicted by Biot-JCAL was found to agree to the experimental one showing the feasibility of the proposed methodology for studied foam. By playing with input parameters of Biot-JCAL, the sound absorption was shown to be dominated by the viscous losses and the elastic effects, while the thermal dissipations play a minor role on the overall sound absorption of this type of foams.

Based on this validated micro-macro model (from statistical morphology to macroscopic properties), a parametric study might be pursued to investigate the combined effect of pore size dispersion and membranes on transport and acoustic properties. A morphological optimization should make it possible to determine target microstructures in order to maximize sound absorption and/or transmission loss for a given frequency range.

Chapter VII

Conclusion and perspectives

Contents

VII.1 General conclusion

This thesis work focuses on the modeling of acoustic foams with wide distribution of pore sizes and their interconnections by homogenization approach. The general objective of this project was to develop a numerical chaining allowing to simulate locally heterogeneous systems of a low density cellular foam. The developed numerical chaining was applied on a graphite PU foam which is notably characterized by a strong local heterogeneity in its pore size. A long term objective will be to propose a modification of the stochastic and locally heterogeneous microstructural parameters in order to enhance multi-functional properties.

The locally heterogeneous microstructures of foam samples were characterized by advanced imaging techniques: X-ray computed tomography and scanning electron microscopy. It was shown that these two techniques are complementary to characterize the foam microstructures. The images obtained from X-ray computed tomography were processed for pore characterization including size, sphericity and neighbor number; while the analyses of SEM images provided information on membrane properties comprising surface, proportion of closed/open membranes, aperture ratio, thickness, number of edges per face (membrane). These morphological features of local microstructure are important input information for the modeling works.

A stochastic model of the microstructure was then reconstructed by using an optimized Laguerre tessellation algorithm (Neper software). This periodic partition was shown to represent the morphological properties of real cellular foam, in terms of pore size and pore sphericity distributions. These experimental statistical properties were used as input parameters of the morphological model. Information on membrane content such as proportion of open membranes and their aperture ratio was also taken into account. Because of high porosity (low density) and very thin membranes, the ligaments and membrane thickness were not modeled. That significantly reduced the number of elements for the FEM simulations.

Concerning the static viscous permeability, an important parameter of transport properties in porous materials, the pore-network simulation initially developed for mono-size foams was extended to polydisperse ones. This is a low computational cost method allowing permeability prediction of a large size domain which can hardly be performed by FEM. A pore-network model including the use of an average aperture ratio was shown to be sufficient to capture the associated transport parameters. The mean pressure field approximation was proposed to quickly estimate permeability of open-cell random foams from the standpoint of the geometrical features only. Small pores in polydisperse foams was shown to have a weak contribution on permeability due to their low volume. Furthermore, by excluding these small pores (10% of total volume), the effective pore size was found in order to simulate polydisperse foams through a mono-sized one. Effect of closed/open membrane proportion on foam permeability was also investigated. This behavior was shown to be dependent on the variation coefficient of membranes surface. Then, an expression was proposed to provide an approximation of the permeability of random foams from measurable parameters of the geometry: distribution of pore size, distribution of membrane surface, proportion of open membranes and their average aperture ratio.

The modeling of foam microstructure with membrane having no thickness helps to reduce computational cost but it cannot describe the effect of real thin membranes on the viscous characteristic length (because the viscous characteristic length tends to zero for a membrane having no thickness - due to the divergence of the surface integral of the electric field). The effect of membrane thickness was studied on this surface integral. A logarithmic relation was found between the surface integral and membrane thickness. Moreover, there is an equivalence between membrane thickness to be reproduced and an appropriate finite element mesh. As a result, a simulation technique of of membrane thickness using a zero-thickness membrane was developed in order to calculate the surface integral of the electric field. Noteworthy, the proposed technique can be used

to simulate the acoustic properties of complex random foams by reducing the computational cost.

An acoustic simulation was performed with the reconstructed microstructure corresponding to the real PU foam studied in this thesis, whose morphological features are locally heterogeneous and display a wide distribution of pore size (as a consequence of the graphite particles introduction). The pore size distribution can be approximated by a lognormal probability law. By image processing, this foamy material also showed high content of thin membrane. A homogenization hybrid multi-scale method was used, in which the transport parameters governing the phenomena of acoustic dissipation serve as input data for the semi-phenomenological models: JCAL model following a rigid skeleton assumption, and the Biot-JCAL formulation when taking into account the elasto-acoustic coupling. The static viscous permeability was calculated by pore-network simulations, the remaining parameters were computed by resolving two classic boundary problems (potential flow, controlled diffusion). The visco-elastic parameters were characterized by experimental measurements. Because of a strong elasto-acoustic coupling observed for the graphite PU foam, only the Biot-JCAL model enables a good agreement between modeling and impedance tube measurements, which validates the developed multi-scale approach.

To conclude, our work provides a complete procedure for the numerical simulation of acoustic foams whose important features are 1) a high porosity and 2) thin membranes (the ration between membrane thickness and pore size is in the order of 0.001): from the acquisition and reconstruction of the locally heterogeneous microstructure to the calculation of the macroscopic properties and determination of the size of the RVE. An important feature of this work is the assessment of poly-sized pores and random nature of a real foam which opens a new morphological path for the optimization of foams with enhanced acoustical performances.

VII.2 Perspectives

In our view, several intriguing topics for future research shall be further investigated following this thesis.

1. It would be of interest to extend the pore-network method to other transport parameters, particularly for the tortuosity α_∞. Actually, the pore-network model for α_∞ was developed for monodisperse foams [59]. It could probably be extended to foams with polydisperse pore size. As with permeability, low computational methods would be useful for a faster estimation of transport parameters and would possibly allow the development of results for complex materials related to percolating effects.

2. A numerical model for Biot's parameters (elastic ones) would complete our numerical procedure. Several approaches could be pursued. If the thickness of membranes is of the kind encountered in graphite PU foam (very thin), one could consider that the solid phase mainly concentrates in the skeleton (this would allow neglecting this membranes). Following this assumption, the elastic properties of random polydisperse foams could realistically be simulated by FEM [46, 38, 81]. Alternatively, a stochastic homogenization method based on empirical marginal distribution functions and correlation functions of apparent properties could be selected [64, 40]. Another fruitful path to consider is related to the concept of permeo-elastic media, including a perfectly rigid skeleton onto which highly flexible thin membranes are fixed [99, 11]. Moreover, the numerical model derived from idealized periodic unit cells from which structure-properties relationships were derived [41] could be extended to the polydisperse foams.

3. A research work for the determination of optimal and manufacturable foam microstructures based on the developed numerical models could be considered in a more systematic

approach combining a series of laboratory and numerical experiments. The proposed multi-scale method developed in this thesis could be used to reduce the number of experimental tests. Although additive manufacturing techniques may be used to produce and design optimal micro-geometries [9, 109, 83], their production remain expensive when compared to large scale manufacturing techniques based on a foaming process. Moreover, advanced additive manufacturing technologies are still limited to production volumes at the scale of a laboratory experiment and cannot reproduce at the same time thin membranes (resolution in the order of 0.1 µm, and large sample size). Therefore, a design of experiment would make it possible to mark out the field of achievable morphologies, in and around this space one could determine more accurately promising optimal configurations.

Appendix A

Effect of contact stiffness on the acoustic measurements

In this appendix, we show experimentally contact stiffness effect between foam samples and backed rigid wall on the acoustic measurement in an impedance tube of 3 microphones.

First of all, the samples used have a diameter slightly larger than the tube (or a thin layer of Teflon was put around the samples) in order to avoid air leakage between the tube walls and the samples, so that it is necessary to apply a slight stress to push it into the tube. The impedance tube consists of two parts, one on which the microphones 1 and 2 are fixed; and the other part (thereafter called the sample holder) containing the sample and the microphone 3 (see Fig. A.1).

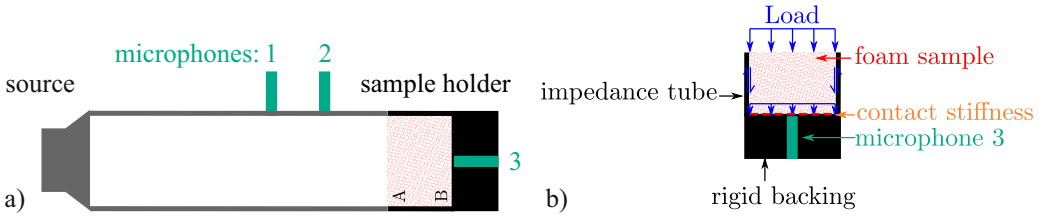

Figure A.1: a) Three-microphone impedance tube. b) Illustration of contact stiffness.

We introduced the sample in the sample holder of the tube arranged vertically and placed a load on top of it in order to press it against the rigid bottom (the lowest mass exceeds the friction force on the side walls). Different loads were used in order to test the effect of the stress. We also carried out a measurement by leaving a small air gap between the rigid bottom and the sample of approximately 0.5 mm (this case is designed by "0 Pa" thereafter). And we made the same measurements after reversing the directions of the sample in the tube (directions A and B). The results are averaged over four measurements.

A.1 Effect of sample placement direction

Fig. A.2 shows the effect of sample placement direction for two extreme stress values tested: "0 Pa" and "190 Pa".

The measurements, for direction A and direction B, are perfectly identical in the "0 Pa" case. Moreover, it is not shown here but the 4 measurements taken on each side are also perfectly repeatable. In the case of foam samples placed with a constraint, the measurements are not perfectly identical in the two directions of placement of the sample (they are on the other hand relatively

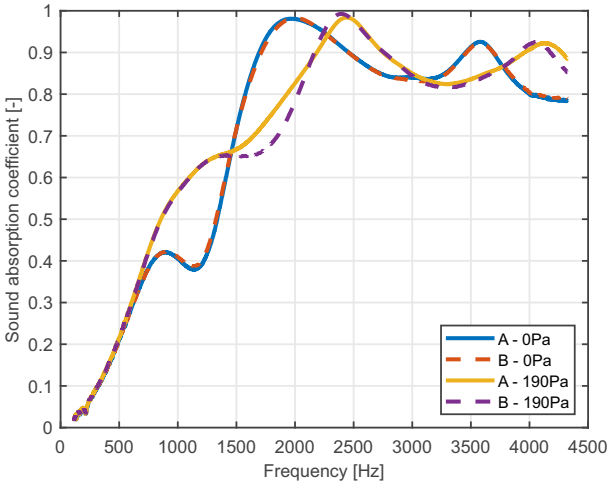

Figure A.2: Effect of sample placement direction on sound absorption coefficient for "0 Pa" and "190 Pa".

repeatable at 190 Pa). The no-load "0 Pa" measurements were repeated several times after stressing the sample. The repeatability of the measurements shows that the load has not irreversibly deformed the sample.

A.2 Effect of constraint variation

The coefficients of sound absorption measured with various loads are plotted in Fig. A.3. The results are averaged over two direction of sample placement.

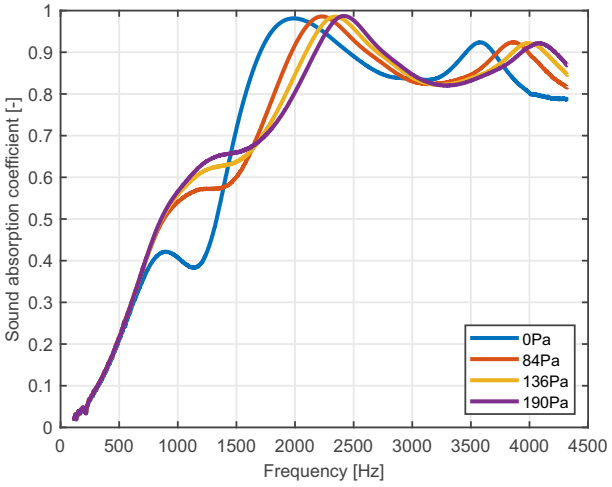

Figure A.3: Effect of sample placement direction on sound absorption coefficient for "0 Pa" and "190 Pa".

It can be seen that apart from the low frequencies behavior, the constraint used for placement of the sample in the tube has a significant impact on the absorption coefficient. According to the measurements, the peaks associated with the vibrations of the foam skeleton depend on this constraint. In the without constraint "0 Pa" case, a small air gap is placed between the sample

and the tube rigid bottom, the resonance peak must be associated with a half wavelength. If the displacements of foam skeleton are null at the contact with the tube rigid bottom, one must have a quarter-wave mode. In Fig. A.3, we see that the measurements at low constraint gradually tend towards measurements with a small air gap (half-wave mode).

This behavior can be explained by considering an effect of contact stiffness between the foam sample and the tube rigid bottom. The constraint applied to the foam sample allows it to be placed more or less in contact with the rigid bottom. Rigorous modeling of acoustic behavior of foam sample in the impedance tube would require taking into account an effect of contact stiffness at the interface foam sample/tube rigid bottom (the contact stiffness depends on the number of contacts, which themselves depend on the constraint or load used to place the foam sample into the tube). The absence of behavior symmetry of the sample under a constraint (difference in the two directions A and B) (see Fig. A.2 for "190 Pa" case) would come from a difference in surface state between two sides of the foam sample which can lead to a difference of contact stiffness.

In a classic model for acoustic absorption at normal incidence backed by an impervious rigid wall, the displacement of the skeleton at the interface with rigid wall is considered null, this implies that the porous material is perfectly in contact with the tube rigid bottom. With perfectly flat and parallel surfaces, this is theoretically realistic. But as soon as one considers defects of flatness or parallelism of the two surfaces in contact, this is no longer possible except by applying a constraint which can correct these two defects. In our manipulations, it is both the (pre)stress applied to the sample and the friction force on the side wall which make it possible to maintain contact at the foam sample/ rigid wall bottom interface. Therefore, in our numerical simulation (chapter VI), we can reduce the elastic modulus of the skeleton by considering that the contact stiffness decreases the apparent stiffness of the foam sample:

$$\frac{1}{K_{\text{apparent}}} = \frac{1}{E'S/L} + \frac{1}{K_{\text{contact}}}$$

Appendix B

Validation about the use of structures without thickness modeling

Here, we show the transport parameters computed by FEM of two Kelvin structures: (A) with and (B) without modeling the thickness of ligaments and membranes. The size of unit cell is $D_p = 1$ mm, the membranes have aperture of identical size d_0. Note that for the structure (A), the ligaments have a regular section where the thickness r is chosen based on the porosity ϕ (see appendix A in [97]):

$$\frac{r}{D_b} \approx \left(\frac{1-\phi}{\frac{3\sqrt{3}}{\sqrt{2}} - \left(10 - 3\sqrt{6}\right)\sqrt{\frac{(1-\phi)\sqrt{2}}{3\sqrt{3}}}} \right)^{1/2} . \tag{B.1}$$

The element size around of the aperture in structure (B) h_e is equal to thickness of membranes e_m in structure (A) (See Tab. B.1) The FEM simulations are performed on an eighth part of Kelvin

	ϕ	d_0/D_p	e_m/D_p	h_e/D_p
With thickness (A)	0.98	0.1	0.001	–
Without thickness (B)	1.00	0.1	–	0.001

Table B.1: Geometrical parameters of two Kelvin cell type.

cell (see Fig. B) taking advantage of existing symmetries [110] in order to reduce computational cost.

The results shown in Tab. B.2 with small deviations, which may come from the difference of porosity, validated the use of structure without thickness modeling (for ligaments and membranes).

	Λ'/D_p	$k_0/D_p^2/\phi$	α_∞	Λ/D_p	$k_0'/D_p^2/\phi$
With thickness (A)	0.3186	0.0034	1.1415	0.3005	0.0300
Without thickness (B)	0.3088	0.0033	1.1375	0.2994	0.0298

Table B.2: Comparison of computed transport parameters.

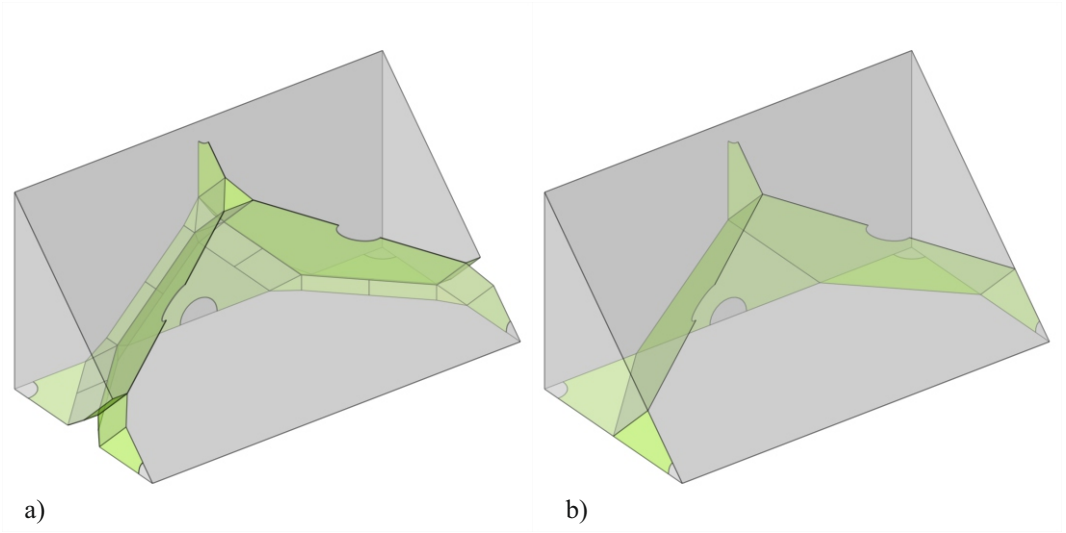

Figure B.1: An eighth part of Kelvin cell. a) with and b) without modeling the thickness of ligaments and membranes.

Bibliography

[1] Y Achdou and Marco Avellaneda. Influence of pore roughness and pore-size dispersion in estimating the permeability of a porous medium from electrical measurements. *Physics of Fluids A: Fluid Dynamics*, 4(12):2651–2673, 1992.

[2] Pablo Acuña, Zhi Li, Mercedes Santiago-Calvo, Fernando Villafañe, Miguel Ángel Rodríguez-Perez, and De-Yi Wang. Influence of the characteristics of expandable graphite on the morphology, thermal properties, fire behaviour and compression performance of a rigid polyurethane foam. *Polymers*, 11(1):168, 2019.

[3] Jean-François Allard and Yvan Champoux. New empirical equations for sound propagation in rigid frame fibrous materials. *The Journal of the Acoustical Society of America*, 91(6):3346–3353, 1992.

[4] Franz Aurenhammer. Power diagrams: properties, algorithms and applications. *SIAM Journal on Computing*, 16(1):78–96, 1987.

[5] Jean-Louis Auriault, Lionel Borne, and René Chambon. Dynamics of porous saturated media, checking of the generalized law of Darcy. *The Journal of the Acoustical Society of America*, 77(5):1641–1650, 1985.

[6] Francois-Xavier Bécot and Luc Jaouen. An alternative Biot's formulation for dissipative porous media with skeleton deformation. *The Journal of the Acoustical Society of America*, 134(6):4801–4807, 2013.

[7] MA Biot. Theory of elastic waves in a fluid-saturated porous solid. 1. low frequency range. *J. Acoust. Soc. Am.*, 28:168–178, 1956.

[8] Maurice A Biot. Theory of propagation of elastic waves in a fluid-saturated porous solid. ii. higher frequency range. *The Journal of the acoustical Society of america*, 28(2):179–191, 1956.

[9] Jean Boulvert, Théo Cavalieri, Josué Costa-Baptista, Logan Schwan, Vicente Romero-García, Gwénaël Gabard, Edith Roland Fotsing, Annie Ross, Jacky Mardjono, and Jean-Philippe Groby. Optimally graded porous material for broadband perfect absorption of sound. *Journal of Applied Physics*, 126(17):175101, 2019.

[10] Claude Boutin, Pascale Royer, and Jean-Louis Auriault. Acoustic absorption of porous surfacing with dual porosity. *International Journal of Solids and Structures*, 35(34-35):4709–4737, 1998.

[11] Claude Boutin and Rodolfo Venegas. Pore-scale bending and membrane effects in permeoelastic media. *Mechanics of Materials*, 145:103362, 2020.

[12] Mauro Bracconi, Matteo Ambrosetti, Matteo Maestri, Gianpiero Groppi, and Enrico Tronconi. A systematic procedure for the virtual reconstruction of open-cell foams. *Chemical Engineering Journal*, 315:608 – 620, 2017.

[13] Kenneth A Brakke. The surface evolver. *Experimental mathematics*, 1(2):141–165, 1992.

[14] Robert JS Brown. Connection between formation factor for electrical resistivity and fluid-solid coupling factor in Biot's equations for acoustic waves in fluid-filled porous media. *Geophysics*, 45(8):1269–1275, 1980.

[15] Bart Buffel, Frederik Desplentere, Kris Bracke, and Ignace Verpoest. Modelling open cell-foams based on the Weaire–Phelan unit cell with a minimal surface energy approach. *International Journal of Solids and Structures*, 51(19-20):3461–3470, 2014.

[16] Larysa Burtseva, Benjamin Valdes Salas, Rainier Romero, and Frank Werner. *Multi-sized sphere packings: models and recent approaches*. Univ., Fak. für Mathematik, 2015.

[17] Philip Crosbie Carman. Determination of the specific surface of powders i. transactions. *J. Soc. Chemical Industries.*, 57:225–234, 1938.

[18] Philip Crosbie Carman. Flow of gases through porous media. 1956.

[19] W David Carrier III. Goodbye, Hazen; hello, Kozeny-Carman. *Journal of Geotechnical and Geoenvironmental Engineering*, 129(11):1054–1056, 2003.

[20] Yvan Champoux and Jean-François Allard. Dynamic tortuosity and bulk modulus in air-saturated porous media. *Journal of Applied Physics*, 70(4):1975–1979, 1991.

[21] Jia-Ji Cheng, Bo-Bo Shi, Fu-Bao Zhou, and Xiao-Yu Chen. Effects of inorganic fillers on the flame-retardant and mechanical properties of rigid polyurethane foams. *Journal of Applied Polymer Science*, 131(10), 2014.

[22] Fabien Chevillotte, Francesca Ronzio, Claudio Bertolini, Minh Tan Hoang, Ludovic Dejaeger, Arnaud Duval, Philippe Mordillat, et al. Inter-Laboratory Characterization of Biot Parameters of Poro-Elastic Materials for Automotive Applications. Technical report, SAE Technical Paper, 2020.

[23] Sung Nok Chiu, Dietrich Stoyan, Wilfrid S Kendall, and Joseph Mecke. *Stochastic geometry and its applications*. John Wiley & Sons, 2013.

[24] A Cortis and DMJ Smeulders. On the viscous length scale of wedge-shaped porous media. *International Journal of Engineering Science*, 39(8):951–962, 2001.

[25] Andrea Cortis, David MJ Smeulders, Jean Luc Guermond, and Denis Lafarge. Influence of pore roughness on high-frequency permeability. *Physics of fluids*, 15(6):1766–1775, 2003.

[26] O Dazel, F-X Bécot, and L Jaouen. Biot effects for sound absorbing double porosity materials. *Acta Acustica united with Acustica*, 98(4):567–576, 2012.

[27] ME Delany and EN Bazley. Acoustical characteristics of fibrous absorbent material. *The Journal of the Acoustical Society of America*, 48(2A):434–434, 1970.

[28] Jean-François Despois and Andreas Mortensen. Permeability of open-pore microcellular materials. *Acta materialia*, 53(5):1381–1388, 2005.

[29] Olivier Doutres, Noureddine Atalla, and Kevin Dong. Effect of the microstructure closed pore content on the acoustic behavior of polyurethane foams. *Journal of Applied Physics*, 110(6):064901, 2011.

[30] Olivier Doutres, Noureddine Atalla, and Kevin Dong. A semi-phenomenological model to predict the acoustic behavior of fully and partially reticulated polyurethane foams. *Journal of Applied Physics*, 113(5):054901, 2013.

[31] X Du and M Ostoja-Starzewski. On the size of representative volume element for Darcy law in random media. *Proceedings of the Royal Society A: Mathematical, Physical and Engineering Sciences*, 462(2074):2949–2963, 2006.

[32] David Edouard, Maxime Lacroix, Cuong Pham Huu, and Francis Luck. Pressure drop modeling on solid foam: State-of-the art correlation. *Chemical Engineering Journal*, 144(2):299–311, 2008.

[33] JJ Espadas-Escalante, F Avilés, PI Gonzalez-Chi, and AI Oliva. Thermal conductivity and flammability of multiwall carbon nanotube/polyurethane foam composites. *Journal of Cellular Plastics*, 53(2):215–230, 2017.

[34] Irving Fatt. *The Network Model in the Study of Porous Media*. PhD thesis, University of Southern California, 1955.

[35] M Firdaouss, J-L Guermond, and D Lafarge. Some remarks on the acoustic parameters of sharp-edged porous media. *International Journal of Engineering Science*, 36(9):1035–1046, 1998.

[36] Serge Galam and Alain Mauger. Universal formulas for percolation thresholds. *Physical Review E*, 53(3):2177, 1996.

[37] K Gao, JAW van Dommelen, and MGD Geers. Microstructure characterization and homogenization of acoustic polyurethane foams: Measurements and simulations. *International Journal of Solids and Structures*, 100:536–546, 2016.

[38] K Gao, JAW Van Dommelen, and MGD Geers. Investigation of the effects of the microstructure on the sound absorption performance of polymer foams using a computational homogenization approach. *European Journal of Mechanics-A/Solids*, 61:330–344, 2017.

[39] Thomas MJ Gebhart, Dieter Jehnichen, Roman Koschichow, Michael Mueller, Michael Goebel, Vinzenz Geske, Michael Stegelmann, and Maik Gude. Multi-scale modelling approach to homogenise the mechanical properties of polymeric closed-cell bead foams. *International Journal of Engineering Science*, 145:103168, 2019.

[40] M Geißendörfer, A Liebscher, C Proppe, C Redenbach, and D Schwarzer. Stochastic multiscale modeling of metal foams. *Probabilistic Engineering Mechanics*, 37:132–137, 2014.

[41] Mohammad S Gholami, Olivier Doutres, and Noureddine Atalla. Effect of microstructure closed-pore content on the mechanical properties of flexible polyurethane foam. *International Journal of Solids and Structures*, 112:97–105, 2017.

[42] L Gong and St Kyriakides. Compressive response of open cell foams part ii: Initiation and evolution of crushing. *International Journal of Solids and Structures*, 42(5-6):1381–1399, 2005.

[43] Lixin Gong, S Kyriakides, and W-Y Jang. Compressive response of open-cell foams. part i: Morphology and elastic properties. *International Journal of Solids and Structures*, 42(5-6):1355–1379, 2005.

[44] Allen Hazen. Some physical properties of sand and gravel with special reference to their use in filtration. *24th Ann, Rep., Mass. State Board of Health, Boston, 1983*, 1983.

[45] Minh Tan Hoang. *Modélisation et simulation multi-échelle et multi-physique du comportement acoustique de milieux poroélastiques: Application aux mousses de faible densité*. PhD thesis, Université Paris-Est, 2012.

[46] Minh Tan Hoang, Guy Bonnet, Hoang Tuan Luu, and Camille Perrot. Linear elastic properties derivation from microstructures representative of transport parameters. *The Journal of the Acoustical Society of America*, 135(6):3172–3185, 2014.

[47] Noureddine Atalla Jean Allard. *Propagation of Sound in Porous Media: Modelling Sound Absorbing Materials 2e*. Wiley, 2nd edition, 2009.

[48] Christian Geindreau Jean-Louis Auriault, Claude Boutin. *Homogenization of Coupled Phenomena in Heterogenous Media*. Wiley-ISTE, 2009.

[49] David Linton Johnson, Joel Koplik, and Roger Dashen. Theory of dynamic permeability and tortuosity in fluid-saturated porous media. *Journal of Fluid Mechanics*, 176:379–402, 1987.

[50] Scott Kirkpatrick. Percolation and conduction. *Reviews of modern physics*, 45(4):574, 1973.

[51] Josef Kozeny. Ueber kapillare Leitung des Wassers im Boden. *Royal Academy of Science, Vienna, Proc. Class I*, 136:271–306, 1927.

[52] Andrew M Kraynik. Foam structure: from soap froth to solid foams. *MRS bulletin*, 28(4):275–278, 2003.

[53] Andrew M Kraynik, Douglas A Reinelt, and Frank van Swol. Structure of random monodisperse foam. *Physical Review E*, 67(3):031403, 2003.

[54] Andrew M Kraynik, Douglas A Reinelt, and Frank van Swol. Structure of random foam. *Physical Review Letters*, 93(20):208301, 2004.

[55] Prashant Kumar and Frédéric Topin. Predicting pressure drop in open-cell foams by adopting Forchheimer number. *International Journal of Multiphase Flow*, 94:123–136, 2017.

[56] Denis Lafarge, Pavel Lemarinier, Jean-François Allard, and Viggo Tarnow. Dynamic compressibility of air in porous structures at audible frequencies. *The Journal of the Acoustical Society of America*, 102(4):1995–2006, 1997.

[57] Christian Langlois, Raymond Panneton, and Noureddine Atalla. Polynomial relations for quasi-static mechanical characterization of isotropic poroelastic materials. *The Journal of the Acoustical Society of America*, 110(6):3032–3040, 2001.

[58] V Langlois, VH Trinh, C Lusso, Camille Perrot, X Chateau, Y Khidas, and O Pitois. Permeability of solid foam: Effect of pore connections. *Physical Review E*, 97(5):053111, 2018.

[59] V Langlois, VH Trinh, and C Perrot. Electrical conductivity and tortuosity of solid foam: Effect of pore connections. *Physical Review E*, 100(1):013115, 2019.

[60] Claudia Lautensack and Sergei Zuyev. Random Laguerre tessellations. *Advances in Applied Probability*, 40(3):630–650, 2008.

[61] David Legland, Ignacio Arganda-Carreras, and Philippe Andrey. MorphoLibJ: integrated library and plugins for mathematical morphology with ImageJ. *Bioinformatics*, 32(22):3532–3534, 07 2016.

[62] Th Levy and E Sanchez-Palencia. Equations and interface conditions for acoustic phenomena in porous media. *Journal of Mathematical Analysis and Applications*, 61(3):813–834, 1977.

[63] Yi Li, Jing Zou, Shengtai Zhou, Yang Chen, Huawei Zou, Mei Liang, and Wenzhou Luo. Effect of expandable graphite particle size on the flame retardant, mechanical, and thermal properties of water-blown semi-rigid polyurethane foam. *Journal of Applied Polymer Science*, 131(3), 2014.

[64] A Liebscher, C Proppe, C Redenbach, and D Schwarzer. Stochastic multiscale modeling of metal foams. *Procedia IUTAM*, (6):87–96, 2013.

[65] Wei Luo, Yi Li, Huawei Zou, and Mei Liang. Study of different-sized sulfur-free expandable graphite on morphology and properties of water-blown semi-rigid polyurethane foams. *RSC advances*, 4(70):37302–37310, 2014.

[66] M Marvi-Mashhadi, CS Lopes, and J LLorca. Effect of anisotropy on the mechanical properties of polyurethane foams: An experimental and numerical study. *Mechanics of Materials*, 124:143–154, 2018.

[67] M Marvi-Mashhadi, CS Lopes, and J Llorca. High fidelity simulation of the mechanical behavior of closed-cell polyurethane foams. *Journal of the Mechanics and Physics of Solids*, 135:103814, 2020.

[68] Xian-Yan Meng, Ling Ye, Xiao-Guang Zhang, Pei-Mei Tang, Jian-Hua Tang, Xu Ji, and Zhong-Ming Li. Effects of expandable graphite and ammonium polyphosphate on the flame-retardant and mechanical properties of rigid polyurethane foams. *Journal of Applied Polymer Science*, 114(2):853–863, 2009.

[69] Yasushi Miki. Acoustical properties of porous materials-modifications of Delany-Bazley models. *Journal of the Acoustical Society of Japan (E)*, 11(1):19–24, 1990.

[70] M Modesti, A Lorenzetti, F Simioni, and G Camino. Expandable graphite as an intumescent flame retardant in polyisocyanurate–polyurethane foams. *Polymer Degradation and Stability*, 77(2):195–202, 2002.

[71] Matthew D Montminy, Allen R Tannenbaum, and Christopher W Macosko. The 3D structure of real polymer foams. *Journal of Colloid and Interface Science*, 280:202–211, 2004.

[72] Thanh Tung Nguyen. *Modeling of complex microcracking in cement based materials by combining numerical simulations based on a phase-field method and experimental 3D imaging*. PhD thesis, 2015. Thèse de doctorat dirigée par Yvonnet, Julien Structures et Matériaux Paris Est 2015.

[73] Andra Nistor, Miloš Toulec, Alexandr Zubov, and Juraj Kosek. Tomographic reconstruction and morphological analysis of rigid polyurethane foams. In *Macromolecular Symposia*, volume 360, pages 87–95. Wiley Online Library, 2016.

[74] Nobuyuki Otsu. A threshold selection method from gray-level histograms. *IEEE transactions on systems, man, and cybernetics*, 9(1):62–66, 1979.

[75] Ju Hyuk Park, Sei Hyun Yang, Hyeong Rae Lee, Cheng Bin Yu, Seong Yeol Pak, Chi Sung Oh, Yeon June Kang, and Jae Ryoun Youn. Optimization of low frequency sound absorption by cell size control and multiscale poroacoustics modeling. *Journal of Sound and Vibration*, 397:17–30, 2017.

[76] Camille Perrot, Fabien Chevillotte, Minh Tan Hoang, Guy Bonnet, François-Xavier Bécot, Laurent Gautron, and Arnaud Duval. Microstructure, transport, and acoustic properties of open-cell foam samples: Experiments and three-dimensional numerical simulations. *Journal of Applied Physics*, 111(1):014911, 2012.

[77] Dominic Pilon, Raymond Panneton, and Franck Sgard. Behavioral criterion quantifying the edge-constrained effects on foams in the standing wave tube. *The Journal of the Acoustical Society of America*, 114(4):1980–1987, 2003.

[78] Olivier Pitois, Asmaa Kaddami, and Vincent Langlois. Permeability of monodisperse solid foams. *Transport in Porous Media*, 134(3):635–649, 2020.

[79] Steven R Pride, Frank Dale Morgan, and Anthony F Gangi. Drag forces of porous-medium acoustics. *Physical review B*, 47(9):4964, 1993.

[80] Romain Quey and Loïc Renversade. Optimal polyhedral description of 3D polycrystals: method and application to statistical and synchrotron x-ray diffraction data. *Computer Methods in Applied Mechanics and Engineering*, 330:308–333, 2018.

[81] C Redenbach, I Shklyar, and H Andrä. Laguerre tessellations for elastic stiffness simulations of closed foams with strongly varying cell sizes. *International Journal of Engineering Science*, 50(1):70–78, 2012.

[82] Claudia Redenbach. Microstructure models for cellular materials. *Computational Materials Science*, 44(4):1397–1407, 2009.

[83] HJ Rice, John Kennedy, Peter Göransson, L Dowling, and D Trimble. Design of a Kelvin cell acoustic meta-material. *Journal of Sound and Vibration*, 472:115167, 2020.

[84] DJ Rowenhorst, AC Lewis, and G Spanos. Three-dimensional analysis of grain topology and interface curvature in a β-titanium alloy. *Acta Materialia*, 58(16):5511–5519, 2010.

[85] Subin Sahu and Michael Zwolak. Maxwell-hall access resistance in graphene nanopores. *Physical Chemistry Chemical Physics*, 20(7):4646–4651, 2018.

[86] Y Salissou and R Panneton. Pressure/mass method to measure open porosity of porous solids. *Journal of Applied Physics*, 101(12):124913, 2007.

[87] Yacoubou Salissou and Raymond Panneton. Wideband characterization of the complex wave number and characteristic impedance of sound absorbers. *The Journal of the Acoustical Society of America*, 128(5):2868–2876, 2010.

[88] Ralph Allen Sampson. Xii. on Stokes's current function. *Philosophical Transactions of the Royal Society of London.(A.)*, (182):449–518, 1891.

[89] Johannes Schindelin, Ignacio Arganda-Carreras, Erwin Frise, Verena Kaynig, Mark Longair, Tobias Pietzsch, Stephan Preibisch, Curtis Rueden, Stephan Saalfeld, Benjamin Schmid, et al. Fiji: an open-source platform for biological-image analysis. *Nature methods*, 9(7):676, 2012.

[90] LM Schwartz, N Martys, DP Bentz, EJ Garboczi, and S Torquato. Cross-property relations and permeability estimation in model porous media. *Physical Review E*, 48(6):4584, 1993.

[91] Jakub Skibinski, Karol Cwieka, Tadeusz Kowalkowski, Bartlomiej Wysocki, Tomasz Wejrzanowski, and Krzysztof Jan Kurzydlowski. The influence of pore size variation on the pressure drop in open-cell foams. *Materials & Design*, 87:650–655, 2015.

[92] Aaron Spettl, Thomas Werz, Carl E Krill, and Volker Schmidt. Parametric representation of 3D grain ensembles in polycrystalline microstructures. *Journal of Statistical Physics*, 154(4):913–928, 2014.

[93] Michael R Stinson and Gilles A Daigle. Electronic system for the measurement of flow resistance. *The Journal of the Acoustical Society of America*, 83(6):2422–2428, 1988.

[94] Minh Tan Hoang and Camille Perrot. Solid films and transports in cellular foams. *Journal of Applied Physics*, 112(5):054911, 2012.

[95] Minh Tan Hoang and Camille Perrot. Identifying local characteristic lengths governing sound wave properties in solid foams. *Journal of Applied Physics*, 113(8):084905, 2013.

[96] William Thomson. Lxiii. on the division of space with minimum partitional area. *The London, Edinburgh, and Dublin Philosophical Magazine and Journal of Science*, 24(151):503–514, 1887.

[97] Van Hai Trinh, Vincent Langlois, Johann Guilleminot, Camille Perrot, Yacine Khidas, and Olivier Pitois. Tuning membrane content of sound absorbing cellular foams: Fabrication, experimental evidence and multiscale numerical simulations. *Materials & Design*, 162:345–361, 2019.

[98] Irene Vecchio, Claudia Redenbach, Katja Schladitz, and Andrew M Kraynik. Improved models of solid foams based on soap froth. *Computational Materials Science*, 120:60–69, 2016.

[99] Rodolfo Venegas and Claude Boutin. Acoustics of permeo-elastic materials. *Journal of Fluid Mechanics*, 828:135–174, 2017.

[100] István L Vér and Leo L Beranek. *Noise and vibration control engineering: principles and applications*. John Wiley & Sons, 2005.

[101] Shijun Wang, Lijun Qian, and Fei Xin. The synergistic flame-retardant behaviors of pentaerythritol phosphate and expandable graphite in rigid polyurethane foams. *Polymer Composites*, 39(2):329–336, 2018.

[102] Denis Weaire. *The Kelvin Problem*. CRC Press, 1997.

[103] Gregor D. Wehinger, Thomas Eppinger, and Matthias Kraume. Detailed numerical simulations of catalytic fixed-bed reactors: Heterogeneous dry reforming of methane. *Chemical Engineering Science*, 122:197 – 209, 2015.

[104] Daniel Westhoff, Jakub Skibinski, Ondřej Šedivỳ, Bartlomiej Wysocki, Tomasz Wejrzanowski, and Volker Schmidt. Investigation of the relationship between morphology and permeability for open-cell foams using virtual materials testing. *Materials & Design*, 147:1–10, 2018.

[105] Wang Xi, Lijun Qian, Zhigang Huang, Yanfang Cao, and Linjie Li. Continuous flame-retardant actions of two phosphate esters with expandable graphite in rigid polyurethane foams. *Polymer Degradation and Stability*, 130:97–102, 2016.

[106] Tianliang Zhai, Dongxu Li, Guoxia Fei, and Hesheng Xia. Piezoresistive and compression resistance relaxation behavior of water blown carbon nanotube/polyurethane composite foam. *Composites Part A: Applied Science and Manufacturing*, 72:108–114, 2015.

[107] HP Zhang and HA Makse. Jamming transition in emulsions and granular materials. *Physical Review E*, 72(1):011301, 2005.

[108] Liqiang Zhang, Meng Zhang, Yonghong Zhou, and Lihong Hu. The study of mechanical behavior and flame retardancy of castor oil phosphate-based rigid polyurethane foam composites containing expanded graphite and triethyl phosphate. *Polymer Degradation and Stability*, 98(12):2784–2794, 2013.

[109] Tomasz G Zieliński, Kamil C Opiela, Piotr Pawłowski, Nicolas Dauchez, Thomas Boutin, John Kennedy, Daniel Trimble, Henry Rice, Bart Van Damme, Gwenael Hannema, et al. Reproducibility of sound-absorbing periodic porous materials using additive manufacturing technologies: Round robin study. *Additive Manufacturing*, 36:101564, 2020.

[110] Tomasz G Zieliński, Rodolfo Venegas, Camille Perrot, Milan Červenka, Fabien Chevillotte, and Keith Attenborough. Benchmarks for microstructure-based modelling of sound absorbing rigid-frame porous media. *Journal of Sound and Vibration*, page 115441, 2020.

[111] Cornelis Zwikker and Cornelis Willem Kosten. *Sound absorbing materials*. Elsevier, 1949.